# Experimental and numerical study on the impact of tsunami waves on composite breakwaters

MSc Thesis

Edoardo Antonio Forte

Delft University of Technology

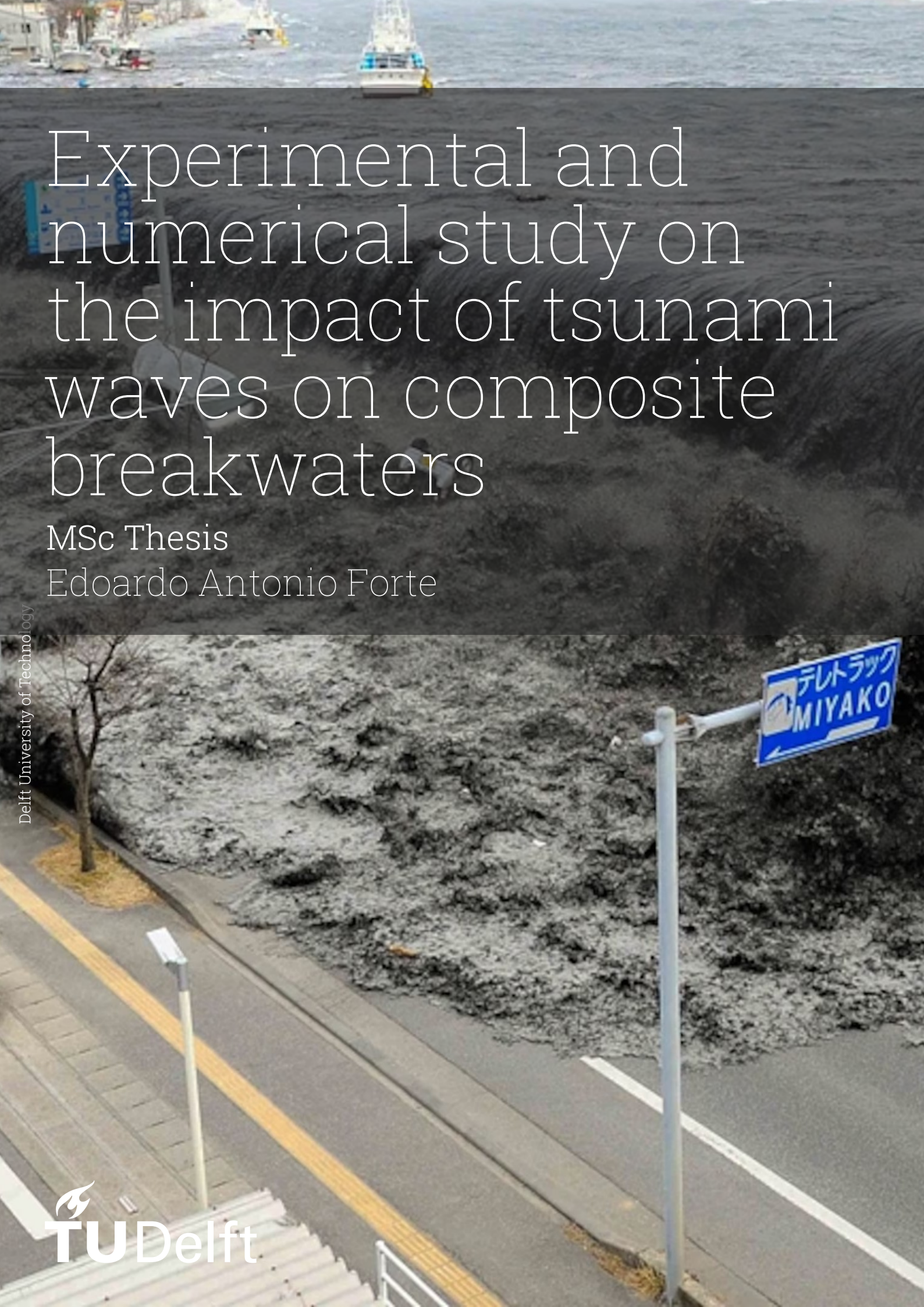


TU Delft

# Experimental and numerical study on the impact of tsunami waves on composite breakwaters

by
Edoardo Antonio Forte

in partial fulfilment of the requirements for the degree of
Master of Science
in Civil Engineering
at the Delft University of Technology

| | |
|---|---|
| Student Name: | Edoardo Antonio Forte |
| Student Number: | 5731364 |
| Assessment Committee: | Dr A. (Alessandro) Antonini, Chair |
| | Dr D. (Davide) Wüthrich, Supervisor |
| | Dr A. (Akshay) Patil, Supervisor |
| Faculty: | Faculty of Civil Engineering and Geosciensces, TU Delft |

| | |
|---|---|
| Cover: | Adapted from WAVE OF DESTRUCTION - Photograph from Mainichi Shimbun/ Reuters |
| Style: | TU Delft Report Style, with modifications by Daan Zwaneveld |

TU Delft

# Preface

This research represents the culmination of my master's degree in Civil Engineering at Delft University of Technology, specializing in Hydraulic Engineering.

The past two years at TU Delft have been extremely stimulating in every aspect. I had the opportunity to study subjects that genuinely interest me and to meet inspiring people, both students and professors, whom I am grateful to have encountered. Throughout this thesis, I deepened my knowledge in tsunami engineering and computational fluid dynamics, two fields that greatly captivate me.

I would like to express my sincere gratitude to the professors on my committee for their constant and essential support from the beginning to the end of this research project: Akshay Patil, Alessandro Antonini, and Davide Wüthrich. Their invaluable assistance throughout all phases of my research, along with their extensive knowledge in the fields of coastal engineering, hydraulic structures, and computational fluid dynamics, was crucial for the success of this thesis.

I would also like to extend my heartfelt thanks to my family. Without their support, I could never have embarked on my degree at TU Delft. Their encouragement was vital, especially when the challenging nature of this master's program felt overwhelming. Finally, I am deeply grateful to all my friends who shared this journey at TU Delft with me, as well as my friends in Italy, whose support and companionship were always felt, even from afar.

*Edoardo Antonio Forte*
*Delft, August 2024*

# Abstract

Many regions around the world are prone to tsunami risk, and their populations are expected to increase. Moreover, past events like the 2011 Great Eastern Japan Earthquake and Tsunami resulted in numerous fatalities and the failure of many coastal protection structures. These events underscore the urgent need for further research in tsunami engineering and the mitigation of tsunami risk. In fact, the capability of coastal protection structures, such as breakwaters, to withstand tsunami loads is not yet fully understood. Additionally, these structures are typically designed to resist wind waves loads rather than the longer waves produced by tsunamis.

This research provides further insight into the interaction between tsunamis and composite breakwaters by analyzing experimental results where a unique technique capable of accurately reproducing tsunamis as scaled N and E-waves was used. The experiments employed a 2-dimensional flume where waves were generated with a tsunami simulator and propagated until they impacted a composite breakwater model, inspired by the world-record breakwater in the Kamaishi bay in Japan. This research thoroughly analyzed the results of one of the experiments conducted at the HR Wallingford research center in the UK, with the objective of understanding the response of a composite breakwater when impacted by a tsunami, focusing particularly on the caisson on top of the structure and its stability. Another objective was the development of a numerical model based on the coupling of the two software OceanWave3D and OpenFOAM, aiming to reproduce physical experiments on tsunami-structure interaction and provide further insights beyond the capabilities of physical tests.

The results of this research indicate that the pressures and forces induced by a tsunami on the caisson of a composite breakwater have a dominant hydrostatic contribution. The absence of wave breaking as the tsunami approaches the breakwater and shoals on its rubble mound prevents the generation of impulsive forces on the structure. The analysis also shows that, for the considered tsunami at prototype scale, the caisson would be unstable and fail due to sliding, primarily because of the water level and pressure differences on the two sides of the structure.
The model developed in this research demonstrated a good accuracy in representing the physical experiment, as evidenced by elevation and pressure time series, with minor limitations on the lee side of the structure and on its rubble mound.
With further validation using additional experimental results, this model can serve as a starting point for future studies on tsunami-structure interaction. It overcomes some limitations of physical testing, potentially provides more accurate results for caisson stability analysis, and offers a cost-effective alternative to physical experiments.

# Contents

# Abbreviations and Symbols

## Abbreviations

| Abbreviation | Definition |
|---|---|
| SWL | Still Water Level |
| OCW3D | OceanWave3D |
| PLWG | Pneumatic Long Wave Generator |
| ADCP | Acoustic Doppler Current Profiler |
| FFT | Fast Fourier Transform |
| LWG | Long Wave Gauge |
| SWG | Short Wave Gauge |
| LPF | Low Pass Filter |
| MULES | Multi-dimensional Universal Limiter with Explicit Solution |
| RANS | Reynolds-averaged Navier Stokes |
| NLL | Nominal Lower Limit |
| NUL | Nominal Upper Limit |
| RMSE | Root Mean Square Error |
| NRMSE | Normalize Root Mean Square Error |
| SF | Stability Factor |
| SL | Stability Limit |
| CFD | Computational Fluid Dynamics |

## Symbols

| Symbol | Definition | Unit |
|---|---|---|
| $Fr$ | Froude number | - |
| $u$ | velocity | m/s |
| $g$ | gravitational acceleration | m/s$^2$ |
| $h$ | depth | m |
| $Re$ | Reynolds number | - |
| $\nu$ | kinematic viscosity | m$^2$/s |
| $We$ | Weber number | - |
| $\rho$ | water density | kg/m$^3$ |
| $l$ | characteristic length | m |
| $\sigma_s$ | surface tension | N/m |
| $L$ | length | m |
| $u_m$ | model velocity | m/s |
| $u_p$ | prototype velocity | m/s |
| $L_m$ | model length | m |
| $L_p$ | prototype length | m |
| $g_m$ | model gravitational acceleration | m/s$^2$ |
| $g_p$ | prototype gravitational acceleration | m/s$^2$ |
| $n_L$ | scale factor | - |
| $T$ | period | s |
| $c$ | celerity | m/s |
| $a^+$ | positive amplitude | m |
| $\eta$ | water surface elevation | m |

| Symbol | Definition | Unit |
|---|---|---|
| $X_1$ | horizontal position of the crest | m |
| $X_2$ | horizontal position of the zero-crossing | m |
| $x_0$ | location of the center of the wave | m |
| $H$ | wave height | m |
| $\Omega_1$, $\Omega_2$ | wave frequency | rad/s |
| $t$ | time | s |
| $A_1$, $A_2$ | wave amplitude | m |
| $p$ | pressure | Pa |
| $u_i$ | velocity in the $i$ direction | m/s |
| $S_{ij}$ | mean strain tensor | 1/s |
| $\rho^*$ | excess pressure | Pa |
| $\mu$ | dynamic molecular viscosity | Ns/m$^2$ |
| $\phi$ | velocity/indicator function in relaxation function | m/s or - |
| $\alpha_R$ | relaxation function | - |
| $\alpha$ | indicator parameter | - |
| $\nabla$ | nabla operator | - |
| $n$ | porosity | - |
| $u_r$ | relative velocity between fluids | m/s |
| $\nu_t$ | turbulent viscosity | m$^2$/s |
| $k$ | turbulent kinetic energy | m$^2$/s$^2$ |
| $\omega$ | turbulent kinetic energy dissipation rate | 1/s |
| $\lambda_1$, $\lambda_2$ | stress limiting coefficients | - |
| $u_p$ | pore velocity | m/s |
| $x_r$ | reference location | m |
| $C_m$ | added mass coefficient | - |
| $\gamma_p$ | closure coefficient | - |
| $F_p$ | flow resistance | kg/m$^2$s |
| $d_{n50}$ | nominal diameter | m |
| $d_{50}$ | median diameter | m |
| $a$, $b$ | resistance terms | - |
| $\alpha$, $\beta$ | resistance coefficients | - |
| $KC$ | Keulegan-Carpenter number | - |
| $n_v$ | bulk porosity | - |
| $e_0$ | void ratio | - |
| $n_{RRD}$ | uniformity index | - |
| $C_o$ | Courant number | - |
| $H_1$ | energy head | m |
| $F$ | force | N |
| $\mu$ | friction coefficient | - |
| $W$ | weight | kg |
| $U$ | total uplift force | N |
| $P$ | total horizontal force | N |
| $M_U$ | moment of uplift force | Nm |
| $M_P$ | moment of wave pressure | Nm |
| $\gamma$ | specific weight | N/m$^3$ |

# 1

# Introduction

## 1.1. Introduction to tsunami risk and mitigation measures

Tsunamis are long gravity waves mainly caused by seafloor displacement or volcanic eruptions. While they propagate from deep sea towards the coast, energy dissipation is generally low, allowing them to retain their destructive power over long distances and posing a significant threat to coastal areas, even those located far from the source location.
Tsunamis can cause extensive damage, including loss of life and the destruction of critical infrastructure such as homes, businesses, ports and harbors. With an expected increase in the population living in tsunami-prone areas, it is crucial to further advance studies in tsunami engineering (Neumann et al. 2015).

Events from the past, such as the 2011 Great Eastern Japan Earthquake and Tsunami and the devastating Indian Ocean Tsunami in 2004, caused 19,868 and 230,000 fatalities, respectively (Shibayama et al. 2013, Telford et al. 2006). The Great Eastern Japan Earthquake and Tsunami, in particular, resulted in the failure and damage of numerous coastal protection structures due to the unexpected wave heights. Gusiakov (2009) identified tsunamis as the fifth most dangerous natural hazard in terms of documented total damage and loss of human lives, reporting more than 700,000 fatalities from tsunamis throughout recorded history up to 2007. Moreover, tsunamis can have an extremely adverse impact on the socioeconomic infrastructure of society due to their ability to affect densely populated and typically well-developed coastal areas. This impact is intensified by their sudden onset, rapid progression, and potential for significant destruction and high fatality rates among the affected population. According to Jelinek and Krausmann (2009), future tsunamis are anticipated to have an even greater impact because the number of people, buildings, and infrastructure exposed to natural hazards is increasing as urban development pressures push into higher-risk areas. Neumann et al. (2015) estimated that the population in low-lying coastal areas, which was 625 million in 2015, will increase by 68–122 %, reaching approximately 1.052 to 1.388 billion people by 2060. This underscore the necessity of protecting vulnerable coastal areas from tsunami hazards and improving our understanding of current tsunami mitigation measures.

Although the most common coastal structures, such as breakwaters, seadikes and seawalls shown in Figure 1.1, are generally designed to protect the coasts against wind waves, there have been attempts to adapt their design for tsunami mitigation. Numerous studies analyzed the performance of these structures against tsunami-like waves (including Foster et al. 2017, McGovern et al. 2018, 2019, 2023, Aniel-Quiroga et al. 2018, 2019). However, the complex interaction between hard structures and tsunamis is not fully understood yet. One notable example is the Kamaishi breakwater, which was the world's deepest breakwater in 2011, designed to withstand possible tsunami waves. Despite these intentions, the structure could not withstand the impact of the Great Eastern Japan Tsunami in 2011 and was partially washed away. The unprecedented size and force of the 2011 tsunami overwhelmed the structure, highlighting the challenges in designing effective tsunami barriers (Tucker 2013). Oetjen et al. (2022) highlighted that while many coastal protection structures may be effective against some

tsunamis, they might not be able to mitigate the impact of more destructive ones. A more thorough understanding of how tsunamis interact with coastal structures like composite breakwaters is essential to assess their stability and effectiveness in mitigating tsunami risks.

**(a)** Seadikes in the Netherlands (Photo by Thijs Damsma)

**(b)** Breakwaters in Asutralia (Ocean Reef Marina project)

**(c)** Seawall on the Isle of Wight, England (Photo by Oikos-team)

**Figure 1.1:** Most common types of coastal protection structures

## 1.2. Research objectives and structure

The objective of this research is to delve deeper into the behavior of hard structures in tsunami protection by analyzing the hydrodynamic interaction between a simulated tsunami event and a composite breakwater. This study builds on data by Van Balen (2023) collected over a five-month research period at HR Wallingford, UK. During this period, a series of scaled laboratory tests were conducted to evaluate the effectiveness of breakwaters against tsunami-like waves. This research thoroughly analyses the shortest and most impulsive wave simulated in those experiments, incorporating a breakwater model inspired by the Kamaishi design. The data from these physical experiments form the basis for developing a numerical model to replicate these results and extend the findings.
Developing a numerical model to simulate the generation and propagation of scaled tsunami waves, and their interaction with coastal structures, represents a significant advancement in tsunami engineering. This approach extends the scope of research beyond physical laboratory experiments, offering a cost-effective alternative for studying tsunami dynamics and mitigation strategies.

The research aims at answering to the following research question:

- What are the key hydrodynamic interactions, pressure distributions and forces exerted when a tsunami wave interacts with a composite breakwater structure?

and the related sub-questions:

- How effectively does a numerical model simulate the generation, propagation, and impact of a tsunami wave interacting with a composite breakwater? What additional insights does it provide compared to experimental results, and what are its associated limitations?
- What are the critical aspects of caisson stability during a tsunami? How well does the numerical model perform in studying the stability of the caisson?

Following the description of tsunami phenomena and the most commonly used coastal protection structures, Chapter 2 offers a comprehensive literature review on the state of the art in tsunami engineering research. This section also describes the typical coastal protection structures used in Japan and the 2011 Great East Japan Tsunami, which led to the failure of the Kamaishi breakwater. Chapter 3 details the methodology employed in the physical experiments and a comprehensive description of the approach followed for the development of the numerical model. Chapter 4 presents an overview of the results from the experimental data analysis and numerical study, along with a discussion on these findings in Chapter 5. Finally, Chapter 6 concludes the thesis by addressing the previously defined research questions and highlighting the limitations encountered in the research.

# 2

# Literature Review

## 2.1. Tsunami definition and common mitigation measures

Tsunamis are very long progressive gravity waves, primarily caused by seafloor displacement and volcanic eruptions. During these events, a large volume of water is forcefully displaced, generating a high-speed wave with an average velocity of 200 m/s at deep see. Tsunamis are characterized by extremely long wavelengths, ranging from 1 to 100 km, and periods varying from 90 to 7000 seconds (McGovern et al. 2018). They are classified as shallow water waves, meaning the ratio between the wavelength and the water depth is less than $\frac{1}{20}$. While tsunami waves propagate from deep sea towards the coast, energy dissipation is generally low, allowing them to retain their destructive power over long distances and posing a significant threat to coastal areas, even those located far from the source location. As tsunamis enter shallow water near land and approach the shoreline, they slow down, wavelengths decrease and waves grow in height. At a depth of 10 m, their typical velocities reduce to an average of 10 m/s (Lampela 2020). Near the shoreline, the rising tsunami wave pulls seawater from the front, causing the water to recede. This results in the sea bottom being exposed, creating a phenomenon known as a drawback. The phenomenon is shown in the cross section depicted in Figure 2.1a

Tsunami events can be divided into two classes based on their return period and typical inundation depths. The inundation depth can be defined as shown in Figure 2.1b. Level 1 tsunamis are described as events with a return period spanning from 50 to 160 years and inundation depths below 10 meters, while Level 2 tsunamis have a return period of hundreds to thousands of years with inundation depths above 10 meters. Although Level 2 tsunamis are less frequent, they can cause extensive inundation damage (Shibayama et al. 2013).


**(a)** Tsunami associated drawback

**(b)** Inundation depth definition

**Figure 2.1:** Typical terms in tsunami engineering and cross shore evolution of tsunami

Tsunami protection measures are generally divided into hard countermeasures, such as dikes, seawalls, and breakwaters, and soft countermeasures, including nature-based solutions. The most com-

monly adopted hard structures include continuous or detached breakwaters, which can be submerged, emerged, or seawalls. Sea dikes are also used and are generally preferred for protecting low-lying areas against flooding. Breakwaters are coastal protection structures designed to mitigate wave impact on the shore through wave reflection and energy dissipation. Besides detached breakwaters, non-detached breakwaters are also used, particularly in harbors (Oetjen et al. 2022). Examples of coastal protection structures are shown in Figure 1.1

## 2.2. The Great East Japan Earthquake and the failure of the Kamaishi breakwater

In Japan's coastal regions, composite breakwaters are the predominant type of hard coastal protection measure. These structures are composed of a rubble mound base with a vertical wall superstructure. They offer several advantages, including enhanced stability, relatively rapid construction, and resistance to wave transmission. Among the drawbacks, it should be acknowledged that composite breakwaters experience higher wave forces due to the wave pressure acting on the vertical section in almost the same phase from top to bottom. Additionally, the vertical section of the breakwater can cause wave reflection, which may pose concerns for nearby harbors (Tucker 2013).

Some of the composite breakwaters in Japan are designed to account for possible tsunami loads, while others are solely intended to withstand wind waves with much shorter periods. Tanimoto et al. (1983) investigated the 1983 Japan Sea Tsunami studying the mitigation effect offered by classical breakwaters in case of tsunami events. He noticed instances of reduced tsunami run-up heights at various ports, attributed to the presence of breakwaters or upright revetments. Oda et al. (2005) demonstrated the effectiveness of breakwaters in reducing inundation depth and flow velocity for smaller tsunamis. However, the tsunamis examined in these studies were considerably smaller than the one witnessed in Japan on March 11, 2011.
This event followed one of the strongest recorded earthquakes in history, with a measured magnitude of 9.0 (Tucker 2013). The earthquake caused a massive tsunami in the Pacific Ocean travelling up to 200 m/s. This resulted in the failure of many sea defense structures specifically designed to provide adequate protection to coastal settlements and critical infrastructure (Alison et al. 2015).

The Kamaishi breakwater was a composite type breakwater located in Kamaishi, 593 km north of Tokyo, in the Iwate Prefecture. The structure comprised of a pair of breakwaters of lengths 990 m and 670 m linked with a submerged 300 m wide opening and it reached a depth of 63 m. Its design featured a trapezoidal cross-section above the rubble base, crafted to enhance resistance against hydrodynamic pressures generated by seismic activity. At the top of the trapezoidal section, the vertical face of the breakwater was designed accounting for wave dissipation effectiveness. Figure 2.2 shows the cross section of the breakwater located in the north side of the bay.

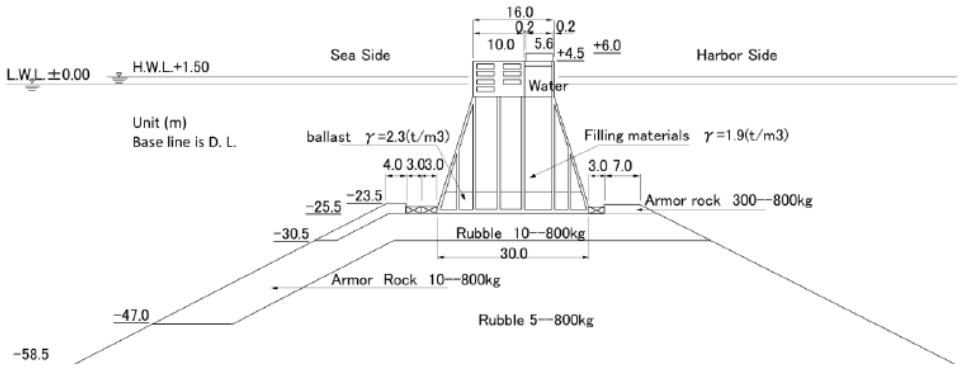


**Figure 2.2:**
Cross section of the Kamaishi breakwater (Arikawa et al. 2012)

Although designed to withstand tsunami loads besides wind waves, the Kamaishi breakwater failed against the Great East Japan Tsunami in 2011 (Arikawa et al. 2012). The breakwater's failure occurred when it was overtopped by the initial wave, measuring 4.3 meters in height (Tucker 2013). The tsunami event led to the displacement of some caisson blocks towards the landward direction. Even the caissons which did not undergo sliding were not correctly positioned anymore after the event (Patil 2019, Arikawa et al. 2012).

During the design of the breakwater, waves with such strong natural force like the ones caused by the 2011 tsunami were not considered. Hence, the breakwater aimed to endure a less destructive tsunami, but the unpredictable characteristics of seismic activity proved to be the primary factor leading to its failure. Nevertheless, extensive research into the design of the breakwater demonstrated that the structure was indeed capable of withstanding seismic action and tsunami forces, albeit not at the magnitude of one of the most powerful earthquakes ever documented (Tucker 2013). According to PARI (2011), despite the Kamaishi breakwater failed against the 2011 tsunami, it managed to reduce the tsunami height by 40%, the maximum run-up height by 50%, and delay the water level rise by 6 minutes. On a related note, Hanzawa and Matsumoto (2015) asserted that detached breakwaters, when exposed to solitary waves, can reduce run-up by 30% to 90%.

A key lesson from the Kamaishi breakwater failure is the connection between failures and scour on the lee side resulting from wave overtopping. In fact, Aniel-Quiroga et al. (2018) suggest that a leading failure mechanism in breakwaters in case of tsunamis, could be caused by scour processes occurring on the rear side due to the overflow. Subsequently, it was recommended to implement the lee side of breakwaters with a proper toe protection, as well as including crown shapes on top of the structure to redirect the flow towards the sea (NILIM 2013). Other phenomena that played a crucial role in the failure of the Kamaishi breakwater, according to Arikawa et al. (2012), are found in the difference in water levels and the decrease in back surface pressure during the overflow. In deep waters, studies by Esteban et al. 2008, 2015a, 2015b suggest that breakwaters are susceptible to being washed away upon impact with a tsunami, while they demonstrate better resilience in shallower waters. Conversely, Hanzawa and Matsumoto (2015) argue that breakwaters in shallower waters tend to incur more damage from solitary wave impacts compared to those in deeper waters. Findings from Esteban et al. 2015a, 2015b also highlighted that the most destabilizing process occurs during the overflow of the breakwater, and during the first impact of the tsunami wave.

## 2.3. State of the art on tsunami engineering

Numerous studies investigated the force exerted by tsunami waves on coastal structures, primarily through physical modelling of scaled tsunami waves in flumes and laboratories. However, these studies sometimes yielded conflicting findings.

A critical observation regarding the majority of existing studies on tsunami-structure interaction, encompassing both physical and numerical investigations, is the prevalent use of solitary waves to represent tsunami-like waves. However, Madsen et al. (2008) highlighted that this approach is flawed and fails to capture the complex behavior and geometry of real tsunami-like waves. Indeed, field observations have confirmed that approaching tsunamis behave as either leading elevation or leading depression waves, depending on the source of the seafloor rupture, rather than as solitary waves. To provide a more realistic representation of prototype tsunami waveforms, Madsen et al. (2008) introduced the concept of N-waves, focusing on the leading trough and its period. Subsequently, Larsen et al. (2019b) analyzed the shape of real tsunami-like waves, identifying elevated E-waves and trough-led N-waves as typical representations. They also proposed an analytical expression to describe these wave types (Equation 2.2).

Shibayama et al. (2013) suggested that while hard countermeasures may be effective for level 1 tsunamis, they may not provide significant protection against more extreme events, such as those

classified as level 2 tsunamis. Krautwald et al. (2022) discussed the set of crucial variables that need to be considered when developing a tsunami resistant structure. These include uplift force, including both hydrostatic buoyancy forces and hydrodynamic ones (drag and impulsive forces). Other factors such as soil stability and geotechnical characteristics like wave-induced erosion and scour also play a crucial role on the structure's stability.

Takagi and Bricker (2015) revealed a link between breakwater dimensions and damage severity. Their study indicates that taller and narrower structures are associated to more significant damage. Mcgovern et al. (2023) found that the force recorded at the wall of a structure is primarily dominated by the hydrostatic component, and the hydrodynamic impulse of the wave plays only a minor role for long waves like tsunamis.

Moreover, findings from Foster et al. (2017) and McGovern et al. 2018 and 2019 indicated that shoaling over a breakwater's rubble mound doesn't lead to wave breaking for large-scale tsunami waves and therefore does not play a role in structural damage. Foster et al. (2017) also observed that longer period waves exhibit no impulsive forces, and their pressure distributions are hydrostatic, regardless of the flow regime. Consequently, they argue that impulsive forces can be neglected, allowing the application of a theoretical framework for quasi-steady flow in unsteady situations like a tsunami hitting a structure. Furthermore, Mcgovern et al. (2023) also confirmed that waves with periods of at least 40 seconds don't produce significant impulsive forces, attributing it to limited shoaling preventing wave breaking. They concluded that the maximum resultant force at the wall is approximately 1.2 times the hydrostatic force. In a different study on the hydrodynamic impact of tsunami-like waves on buildings, Wüthrich et al. (2018) noted an initial impact characterized by high-splash, followed by quasi-steady hydrodynamic flow around the structure.

Mizutani (2015) identified three different pressure peaks in wave pressures acting on a structure configured as a sloped wall. According to their study, a first dynamic wave pressure appears when the incident wave reaches the slope and impacts it. A second sustained wave pressure is observed when wave run-up and water level remain high through a series of incident waves. A final wave pressure appears when reflected and incident waves collide. They also describe an overflowing wave pressure, which is maximum when the overflowing wave collides on the back of the structure. Aniel-Quiroga et al. (2019) conducted studies on the pressures generated by tsunami-like waves on crown-walls positioned on top of a rubble mound breakwater using both physical experiments and numerical simulations to further investigate their findings. They discovered that the maximum horizontal pressure on a the vertical wall of a crown-wall primarily stems from the initial impact of a tsunami. A secondary lower pressure peak follows from the water mass down- rushing the wall. They also studied the vertical uplift force prompted by the pressure of the transmitted wave generated by the overtopping jet falling into the lee side. Regarding the uplift forces, they observed the same two peaks followed by a third one prompted by the pressure of the transmitted wave generated by the overtopping jet falling into the lee side.

Before that, Aniel-Quiroga et al. (2018) had already performed laboratory experiments to study the stability of rubble mound breakwaters under tsunami waves and subsequent overflow. They concluded that there is no clear correlation between tsunami wave height, number of waves and damage on structures. The overflow jet generates high turbulence on the lee side, with the resulting scouring process potentially causing harm to the breakwater's integrity.

Among the notable studies that employed numerical models, Guler et al. (2018) integrated physical experiments and numerical modelling to simulate solitary waves to mimic tsunamis under different configurations and conducted a tsunami overflow test over a breakwater with a crown wall. They provided a detailed description of the pressure distribution exerted by solitary waves around the crown wall. Their study demonstrated that the maximum pressure is applied to the crown wall from the bottom edge (uplift pressure) during solitary wave action. Hsu et al. (2022) also encompassed both experimental and numerical modelling techniques to study the forces exerted by extreme waves on vertical breakwaters. A key conclusion of their study is that the Goda method, originally designed for wind waves, fails to accurately represent the real pressures on the faces of monolithic breakwaters in the case of extreme

waves. It tends to overestimate the maximum forces exerted by very steep waves and overtopping waves. They also emphasized the necessity of studying the lee side of monolithic breakwaters, as the pressures exerted on the rear side can be substantial due to the impact of overtopping wave jets and water level fluctuations induced by the overtopping flow.

Mata (2021) conducted an extensive study on the capabilities of numerical solvers, such as OpenFOAM, to accurately represent wave-structure interactions under various wind-wave conditions. They employed a coupled numerical tool by combining OceanWave3D and OpenFOAM, referred to as CoastalFOAM, to investigate wave loads exerted on the crest wall of a breakwater modeled after the Holyhead breakwater in the UK. The research concluded that the dual numerical tool can model with high accuracy the surface elevation timeseries and induced forces in case of both normal and more extreme wind-waves, with Pearson's coefficients around 0.60 to 0.90 if compared to physical experiments.

## 2.4. Recent progress in tsunami engineering studies

The most common structures for the protection of coasts, including breakwaters, are generally designed to resist the loads exerted by wind waves, while tsunami loads are rarely considered. At present, it is not perfectly clear what level of protection these structures provide against tsunamis. Only limited studies exist regarding the implementation of breakwaters design techniques to counteract the destructive effects of tsunamis. Most studies are based on physical model tests relying on flume experiments (for example Kato et al. 2007, Mizutani 2015, Arikawa et al. 2012, Aniel-Quiroga et al. 2019) . However, replicating long waves such as tsunamis in a physical flume faces limitations due to the challenges in physically reproducing tsunami waves. Conversely, only a limited number of studies explore numerical modeling of the interaction between tsunamis and breakwaters (such as studies by Aniel-Quiroga et al. 2019, Guler et al. 2018, Hsu et al. 2022). Existing numerical research on tsunami waves impacting coastal structures focuses on various types of infrastructure. However, there is a limited number of studies specifically investigating interactions with vertical walls or composite breakwaters.

Van Balen (2023) conducted a series of laboratory tests at HR Wallingford to investigate the effectiveness of breakwaters against tsunami-like waves, simulated as the N and E waves described by Madsen et al. (2008) and Larsen et al. (2019b). These tests employed a unique Pneumatic Long Wave Generator (PLWG), referred to as the tsunami simulator, which was developed through a collaborative project between the University College of London and HR Wallingford, U.K.Rossetto et al. (2011) applied this technology to a flume with a constant depth for the first time. The PLWG enabled the simulation of tsunami waves with unprecedented precision.
Theoretical trough-led N-waves are described by Madsen et al. (2008) with the following equation:

$$\eta(X,0) = \alpha \frac{H}{d}(X - X_2) sech^2(K_s(X - X_1)) \tag{2.1}$$

where $\alpha$ is a constant of scaling, $X_1$ is the position of the crest and $X_2$ the horizontal position of the zero-crossing. $K_s$ is defined as $K_s = \frac{1}{h}\sqrt{\frac{3H}{4h}}$. Another analytical representation of the N and E wave equation, capable of reproducing the physics of tsunami waves was given by Larsen and Fuhrman 2019:

$$\eta(x,t) = A_1 \operatorname{sech}\left[\Omega_1\left(t - t_1 - \frac{x - x_0}{\sqrt{gh}}\right)\right]^2 - A_2 \operatorname{sech}\left[\Omega_2\left(t - t_2 - \frac{x - x_0}{\sqrt{gh}}\right)\right]^2 \tag{2.2}$$

Where $A_1$ and $A_2$ are the amplitude of the two single waves, $\Omega_i = \frac{2\pi}{T_i}$, $x_0$ is the location of the center of the wave and $t_1$, $t_2$ are used for wave shifting of the two single waves. Figure 2.3 gives an illustration of typical shapes of these waves.

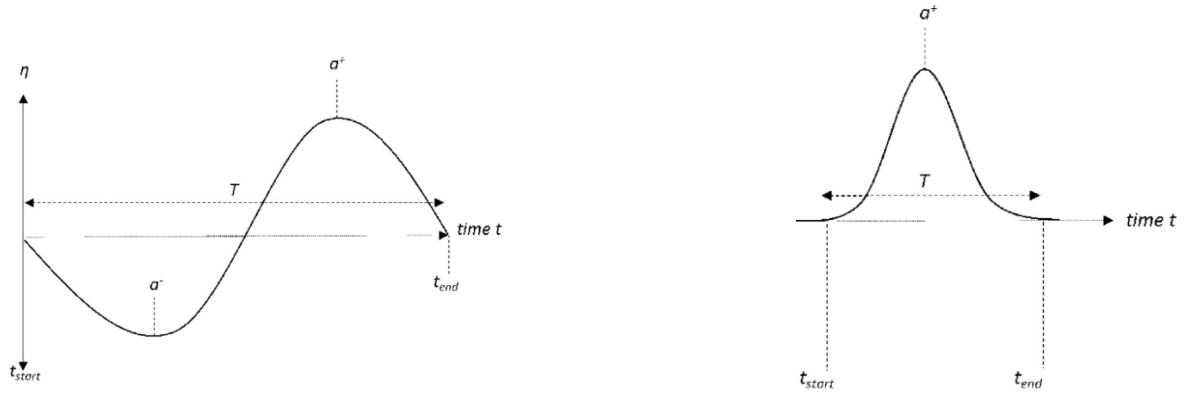


**(a)** Trough led N-wave

**(b)** Elevated E-Wave

**Figure 2.3:** N and E waves defined in McGovern et al. (2018)

Crest-led and trough-led wave forms, with modeled periods ranging between 20 and 236 seconds, were simulated and studied by Van Balen (2023). The laboratory tests conducted using the PLWG focused on evaluating the performance of various tsunami countermeasures, including both hard and soft measures, mainly focusing on the effects produced on tsunami-induced beach run-up. The study concluded that the breakwater proved to be highly effective in mitigating tsunami-induced run-up, significantly outperforming natural solutions. Additionally, it highlighted several advantages of using breakwaters to mitigate tsunami risk, including reduced coastal erosion and wave activity, improved beach quality, reef development, and increased biodiversity. Another significant finding of the research was that the pressures exerted by N and E waves on the breakwater were predominantly hydrostatic, with small contributions from hydrodynamic forces.

The limitations in many previous studies, as emphasized by Madsen et al. (2008), regarding the inadequate representation of tsunamis as solitary waves, and the introduction of new wave forms for more accurate tsunami representation, underscore the need for further research. Additionally, recent advancements in numerical modelling techniques enable further investigation of previous experimental findings to enhance understanding of tsunami-structure interactions.

# 3

# Methodology

In this section, a comprehensive overview of the methodology employed in both the physical experiments and the numerical model is provided. First, an introduction to the experiments performed by Van Balen (2023) is presented, describing the experimental set-up. Then, the focus shifted to the numerical model developed in this thesis. This last part includes both a description of the softwares that were used and in depth illustration of the set-up of the numerical model.

## 3.1. Experimental set-up

### 3.1.1. Froude scaling

In 2023, Van Balen (2023) spent five months in the HR Wallingford research center in UK for his thesis project. His aim was to physically replicate scaled tsunami waves impacting a beach and analyze the mitigating effects produced by both hard structures and nature-based solutions.
In particular, many experiments were set up to simulate the impact of tsunami waves on an offshore breakwater within a controlled flume environment. These experiments were part of a bigger multi-disciplinary research project called MAKEWAVES (2024).

In his research, Froude scaling was used to replicate the physics of tsunami-structure interaction in a feasible laboratory scale. Froude scaling is in fact often recommended when modelling free-surface phenomena like waves, as gravity is the main driving force both in the model and prototype (the real scale phenomenon) (Hughes 1993). This scaling technique is based on the requirement that the Froude number is exactly the same in both the model and prototype .
The Froude number is defined as follows:

$$Fr = \frac{u}{\sqrt{gh}} \tag{3.1}$$

where $u$ is a characteristic velocity, typically wave celerity, $h$ is the water depth and $g$ the gravitational acceleration.
Particular attention should be posed to the Reynolds and Weber number when using Froude scaling. The two numbers can be defined as:

$$Re = \frac{ul}{\nu} \tag{3.2}$$

$$We = \frac{\rho \nu^2 l}{\sigma_s} \tag{3.3}$$

In which $\rho$ is the density of water, $l$ a characteristic length, and $\sigma_s$ the surface tension. While $Re$ describes the relative importance of viscous effects, $We$ characterizes the importance of surface tension effects. Using the celerity $c$ as characteristic velocity and the water depth $h$ as characteristic length, Van Balen (2023) calculated the Reynolds number to vary within a range of $3.3 - 3.9 \cdot 10^6$ and the Weber number between $1.4 - 1.7 \cdot 10^5$ in the experiments. With these values, according to McGovern

et al. (2018), Froude scaling techniques can be used neglecting the scale effects from $Re$ and $We$. The conservation of Froude number in the model ($m$) and prototype ($p$) can be formulated as follows:

$$\frac{u_m}{\sqrt{g_m L_m}} = \frac{u_p}{\sqrt{g_p L_p}} \tag{3.4}$$

A scale factor was introduced to indicate how much smaller the model is compared to the prototype:

$$n_L = \frac{L_p}{L_m} \tag{3.5}$$

where $L_p$ is the length scale of the prototype and $L_m$ the length scale of the physical model. To ensure an undistorted model, all length scales were scaled accordingly in the experiments. Table 3.1 summarizes the typical scales determined by Hughes (1993) used in Froude scaling.

**Table 3.1:** Froude scaling factors according to Hughes (1993)

| Variable | Unit | Froude Scale |
|---|---|---|
| Length | $L$ | $n_L$ |
| Volume | $L^3$ | $n_L^3$ |
| Time | $T$ | $\sqrt{n_L}$ |
| Frequency | $T^{-1}$ | $\sqrt{n_L}$ |
| Velocity | $LT^{-1}$ | $\sqrt{n_L}$ |
| Acceleration | $LT^{-2}$ | 1 |
| Discharge | $L^3T^{-1}$ | $n_L^{2.5}$ |
| Pressure | $M^{-1}LT^{-2}$ | $n_L$ |
| Force | $MLT^{-2}$ | $n_L^3$ |
| Angle | ° | 1 |

For long wave modelling, Heller (2011), recommended a maximum scale of 1:50 to ensure accurate representation of the physical processes.
The Tsunami Simulator housed at HR Wallingford, introduced in Section 2.4, was used for the generation of tsunami waves, after being proved to effectively replicate tsunami waves at a 1:50 scale (McGovern et al. (2018)). The scale factor used in the experiments was therefore equal to 50, meaning that distances were scaled by a factor of 50, while timescales by a factor $\sqrt{50}$, according to table 3.1.

### 3.1.2. Generated waves

The waves generated had periods T ranging from 20 to 240 seconds, equivalent to prototype periods of 140 to 1700 seconds, falling within the range of typical real tsunami wave periods of 90 to 7000 seconds (McGovern et al. 2018). All the experiments performed involved very long waves in a shallow canal ($\frac{h}{L} < \frac{1}{20}$), allowing the use of shallow water approximation theory. The wave celerity can be defined using the shallow water equations:

$$c = \sqrt{g(h + a^+)} \tag{3.6}$$

where $h$ is the constant still water flume depth and $a^+$ is the positive amplitude of the wave as shown in Figure 2.3. The waves simulated to represent tsunamis were E and N type waves, as defined by Madsen et al. (2008) and detailed in Section 2.4.
The study utilized the second generation of the Tsunami Simulator (TS) located at HR Wallingford. The capability of the TS to simulate N and E waves as defined in 2.1 was already demonstrated by McGovern et al. (2018) and its mechanism of wave generation is better detailed in Van Balen (2023). Illustrations of the shapes of these typical waves are provided in Figure 2.3 . In this research, the

focus was on the study of the E20 wave, corresponding to an elevated wave with a modelled period of 20 seconds. The equation of E waves can be obtained by imposing $A_2 = 0$ in Equation 2.2. In the experiment, the elevated wave was followed by a depression deriving from the generation of the wave by the paddle. However, the E-waves as defined by Madsen et al. (2008) follow the shape illustrated in Figure 2.3b, meaning that the tsunami is characterized by a single positive elevation only. Therefore, this study focused on the analysis and numerical reproduction of the positive elevation only.

### 3.1.3. Experimental set-up and instrumentation

The experiments took place in a physical flume which was 100 m long and 1.8 m wide. The water depth was set to 1.02 m in still water conditions and the tsunami simulator was positioned at the far right end of the flume, with its tip taken as an origin. The breakwater structure was placed at a distance 52.12 m from the tsunami simulator's tip. The flume was characterized by a constant flat bathymetry from its origin at $x$ = 0 m to the landward toe of the breakwater rubble mound, at $x$ = 55.2 m. After this part, the bed of the flume was inclined with an angle 1:30 until the end located at $x$ = 100 m. The location of the still water level was $x$ = 85.30 m. Right after this location, the bottom extended for 15 further meters out of the water to simulate a beach with a 1:30 slope. On the beach, a rough board was placed to simulate the presence of a mangrove forest and was not removed for the tests involving the breakwater. Figure 3.1 shows a picture of the flume used in the experiments

Various equipment, including wave gauges, vectrinos, and pressure transducers, were placed along the flume and on the caisson faces to collect data such as surface elevations, velocities, and pressures. For elevation data collection, 15 resistance-type wave gauges were used, comprising 8 Long Wave Gauges positioned off- and nearshore and 7 Short Wave Gauges onshore. The gauges monitored water levels in real-time with an accuracy of 0.0005 m. The wave gauges were calibrated daily to ensure consistency between daily measurements.

To analyse pressures and forces on the breakwater, 4 pressure transmitters and 8 pressure transducers were installed on the caisson's front, rear, top, and bottom face. Their positions are illustrated in Figure 3.2b. These sensors register pressure exerted by the water on the breakwater. The sensors are characterized by a flush diaphragm with a 17 mm diameter. It was assumed that the measured values corresponded with the pressure at the location of the sensors' axes. The combined linearity and hysteresis errors are less than 0.25% of the full scale range. Prior to their use, the pressure sensors were lowered into a water column with know height and calibrated determining the zero pressure value. Therefore, the pressure values measured by the transducers did not account for the still water hydrostatic pressure acting on the sensors, that was added to the measurements for data analysis in this thesis.
For every Pressure Transducer and Transmittors (PTs), the hydrostatic pressure is given by the following formula:

$$p_{hydrostatic} = \rho g h \tag{3.7}$$

With $\rho$ = 1000 kg/m$^3$ for water, $g$ = 9.81 m/s$^2$ and $h$ the distance between the free surface and the axis of every PT.

All measurement equipment was connected to a 64-channel board, linked to an HR Wallingford-supplied desktop running HR DAQ software for calibrations and data collection.

### 3.1.4. The physical breakwater model

The breakwater used in the physical experiments was inspired by the Kamaishi breakwater (Arikawa et al. 2012) shown in Figure 2.2.

The breakwater constructed in the physical flume, and subsequently reproduced in the numerical flume, was formed by an impermeable wooden caisson placed on top of a permeable rubble mound. The caisson had dimensions of 560 mm height and 460 mm width. It was mounted on battons bolted into the walls of the flume. To enhance caisson rigidity, numerous ribs were mounted inside. The rubble mound

was composed of three permeable layers formed by aggregate with different dimensions, consisting of a core, an underlayer and a toplayer.
The grading consisted of aggregate with the following sediment sizes:

- Toplayer: 10-17 mm
- Underlayer: 10-20 mm (30%), 5-10 mm (65%), 1-5 mm (5%)
- Core: 10-20 mm (30%), 5-10 mm (60%), 1-5 mm (10%)

In Figures 3.2a and 3.2b, a zoom on the breakwater model and its pressure sensors is depicted.

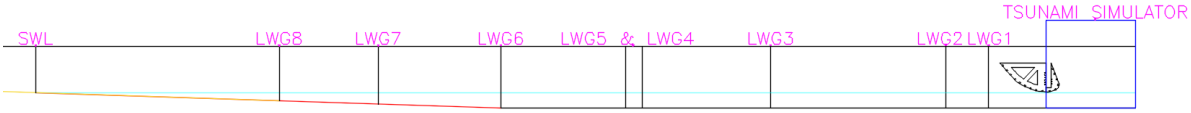


**Figure 3.1:** Flume used in the physical experiments (Van Balen 2023)

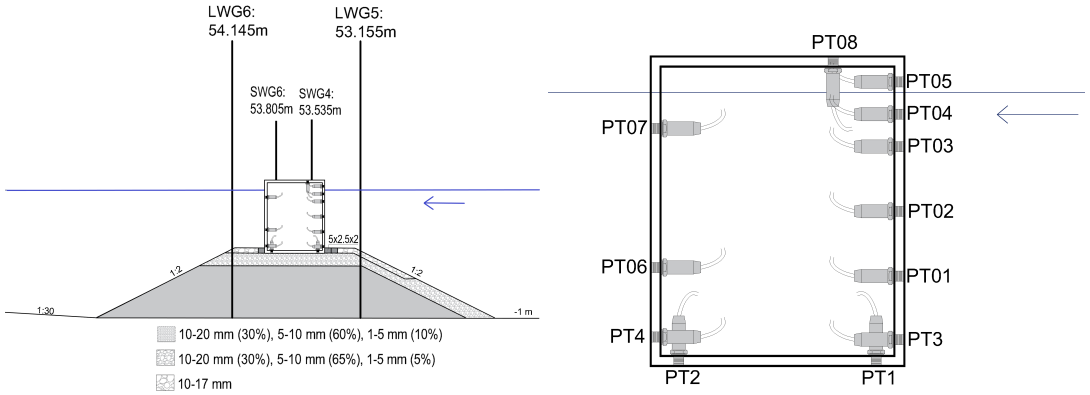


**(a)** Physical breakwater model

**(b)** Zoom on the physical caisson model

**Figure 3.2:** Experimental flume and breakwater model

### 3.1.5. Preliminary signal processing of experimental data

All the pressure sensors time series collected in the experiments were contaminated with high frequency noise which made the recorded signals difficult to analyse. To limit the effect of noise, all the pressure time series were filtered with a low pass filter, capable of eliminating the noise frequencies. A Fast Fourier Transform (FFT) was applied to every pressure record to identify the frequencies of the signal and of the noise. All signals spectra showed higher peaks of signal amplitude at low frequencies, corresponding to the signal, and smaller peaks at higher frequencies, identified as noise. The cut-off frequency for the filters was set to 0.3 Hz, meaning that all the frequencies above 0.3 Hz were removed from the signal. 0.3 Hz was recognised as the maximum frequency below which the signal was not noise, after performing a sensitivity analysis on the cut-off frequency.

It must be acknowledged that elevations data obtained from wave gauges located on the rear side of the structure and close to it, like at LWG6, are less reliable than those from gauges located in the front. This discrepancy is due to the limitations of wave gauges when they encounter biphasic water-air turbulent flow. In fact, the employed wave gauges measure the water level variation based on the conductivity change as a function of wetness. The presence of air bubbles mixed with water in the region behind the breakwater, caused by the overflow jet falling behind the structure, hindered measurements due to the different conductivity of air and water. Because of these reasons, LWG6 in particular recorded an elevation signal highly contaminated by small amplitude oscillations, attributed to the alternation of air and water particles. The pressure sensors on the lee side of the caisson were also

affected by the presence of air bubbles in the water. Pressure transducers and transmitters utilize strain gauges to measure the pressures acting on them, which operate by detecting changes in electrical resistance. The alternation of water particles and and air bubbles hitting the transducers induces high-frequency oscillations in the pressure records. This is the reason why pressure sensors on the lee side of the structure, apart from the instrumental noise, were also contaminated by further oscillations that hindered their interpretation. For the sensors experiencing multipase flow, a LPF with the same cutoff frequency as the other sensors of 0.3 Hz was applied, for consistency of data . This cut-off was capable of removing most of the noise affecting the signal and partially limit the fluctuations caused by the biphasic fluid behind the caisson.

As a reference, Figure 3.3 shows the result of the filtering procedure of a pressure sensor.

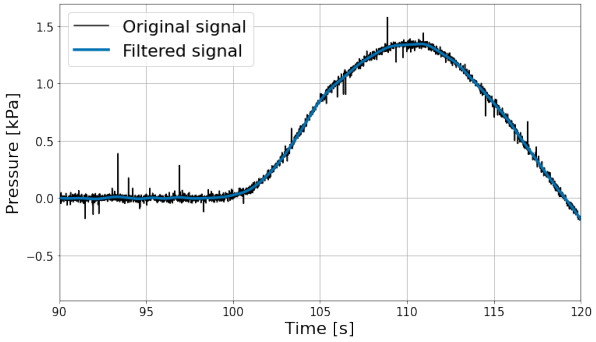


**Figure 3.3:** Original and filtered pressure signal at PT3

## 3.2. Numerical model

### 3.2.1. OpenFOAM and waves2Foam

OpenFOAM (Open-source Field Operation And Manipulations) is a C++ based open source software mainly used for Computational Fluid Dynamics (CFD). It was originally released in 2004 by OpenCFD Ltd. For this research, OpenFOAM 2206, released in June 2022 was used. This version was preferred to the newest 2312 as it was the latest available version compatible with the waves2foam library when the research started.
Waves2foam is a toolbox implemented by Jacobsen et al. (2012) used to generate and absorb free surface water waves, using interFoam as a base solver. This tool is capable of solving the Reynolds-Averaged Navier-Stokes (RANS) equations for multi-phase incompressible flows, with a tracking of the free surface through the Volume of Fluid (VOF) approach, explained in Section 3.2.5 .

The basic form of the Navier-Stokes continuity and momentum equations used in waves2foam are defined by Larsen et al. (2019b) as follows:

$$\frac{\partial u_i}{\partial x_i} = 0 \tag{3.8}$$

$$\frac{\partial \rho u_i}{\partial t} + u_j \frac{\partial \rho u_i}{\partial x_j} = -\frac{\partial \rho^*}{\partial x_i} - g_j x_j \frac{\partial \rho}{\partial x_i} + \frac{\partial}{\partial x_j}(2\mu S_{ij}) + \sigma_T \kappa \frac{\partial \alpha}{\partial x_i} \tag{3.9}$$

Where$u_i$ are the mean components of the velocities, $x_i$ the Cartesian coordinates, $\rho$ the fluid density, taking a constant $\rho_{water}$ value in the water and a constant $\rho_{air}$ value in the air. $\rho^*$ is the pressure minus the hydrostatic potential $\rho g_j x_j$, $g_j$ is the gravitational acceleration, $\mu = \rho\nu$ is the dynamic molecular viscosity, and $S_{ij}$ is the mean strain rate tensor, defined as:

$$S_{ij} = \frac{1}{2}\left(\frac{\partial u_i}{\partial x_j} + \frac{\partial u_j}{\partial x_i}\right) \tag{3.10}$$

Finally, in the last term of equation 3.9, $\sigma_t$ is the surface tension between water and air, $\kappa$ is the local surface curvature and $\alpha$ an indicator field which takes a value of 0 in the air and 1 in the water.

The evolution of $\alpha$ is determined by the continuity equation, which can be expressed in terms of $\alpha$ as:

$$\frac{\partial \alpha}{\partial t} + \frac{\partial \alpha u_j}{\partial x_j} = 0 \tag{3.11}$$

In the waves2Foam framework, maintaining the sharpness of the interface of flows poses a numerical challenge. To tackle this issue, a numerical interface compression method was employed, called "Multidimensional universal limiter with explicit solution" (MULES). This approach is implemented to ensure the accuracy and stability of the simulation by effectively managing the interface sharpness and regulating phase fluxes within the computational domain.

### 3.2.2. The relaxation zone technique

Waves2Foam allows the use of the relaxation zone boundary condition to avoid reflection of waves from outlet boundaries and interference of internal reflected waves with the wave maker boundaries (Jacobsen et al. 2012). Relaxation zones work by weighting the computed solution (velocity and indicator function) and the target solution (based on the imposed wave theory, i.e. the solution modelled by OceanWave3D). The computed solution is solved each time step with the equations:

$$\phi = \alpha_R \cdot \phi_{\text{computed}} + (1 - \alpha_R) \cdot \phi_{\text{target}} \tag{3.12}$$

$$\alpha_R(\chi_R) = 1 - \frac{\exp\left(\chi_R^{3.5}\right) - 1}{\exp(1) - 1} \quad , \chi_R \in [0; 1] \tag{3.13}$$

$\phi$ can be imposed as either the velocity **u** or the indicator parameter $\alpha$. $\alpha_R$ is the relaxation function. $\chi_R$ is defined such that $\alpha_R$ is equal to 1 ($\chi_R$ equal to 0) at the interface between the non-relaxed part of the computational domain and the relaxation zone, ensuring that only the computed values remain. Conversely, at the opposite side, $\chi_R$ is equal to 1 ($\alpha_R$ equal to 0), ensuring that only the target solution remain (Moretto 2020).

### 3.2.3. OceanWave3D

For the generation of the wave modelled in the physical lab, the nonlinear potential flow solver OceanWave3D (OCW3D) was employed. OceanWave3D is a finite difference model based on nonlinear and dispersive potential flow assumption. A detailed description of how potential flow solvers like OCW3D work is given by Engsig-Karup et al. (2009). The model can be used to simulate waves propagating on a canal in shallow water conditions. Its performance is in general very good in case of weakly non-linear and fairly long waves, like tsunamis (Moretto 2020).
In OCW3D, the potential flow is fully characterized by means of a velocity potential function $\phi$, representing the particles velocities in the water, and the position of the free surface $\eta$ relative to the SWL. The particles motion is assumed irrotational, meaning that $\nabla u = 0$. This assumption is valid if the viscous terms are not dominant in the fluid. Engsig-Karup et al. (2009) noted that viscous effects are usually not important away from solid boundaries, therefore the potential fluid approximation can be applied in the first and last part of the numerical domain, far from the breakwater. On the other hand, in the part of the flume where the tsunami wave interacts with the breakwater, achieving an accurate resolution of phenomena like wave overtopping and its associated physics is essential. Consequently, OpenFOAM serves as the chosen computational fluid dynamics solver for this specific task in the inner part of the numerical domain.
The complete flume used in the numerical model can be seen in Figure 3.4.

A time varying, inhomogenoeus Neumann boundary condition is expressed by means of a Laplacian equation:

$$\frac{\partial \phi}{\partial x} = u_p \tag{3.14}$$

Imposing $u_p$ as the horizontal velocity of the wave paddle, the experimental conditions can be recreated with OCW3D (Paulsen (2013)).

### 3.2.4. Coupling OpenFOAM with OceanWave3D

The coupling between OpenFoam and OceanWave3D was firstly achieved by Paulsen (2013). The two solvers can be coupled using a relaxation zone capable of transferring the hydraulic conditions from the OCW3D domain to the OpenFOAM solver. OCW3D calculates a target solution at its interface with the OpenFOAM domain, that is transferred to the latter. The relaxation zone is prescribed in the inlet of the OpenFOAM domain. Numerous validation studies using the coupling between OceanWave3D and OpenFOAM were performed before and during the period of the JIP CoastalFOAM (2015-2019).

### 3.2.5. The Volume of Fluid method

The assumption of the potential flow theory used in OceanWave3D is not valid at the interface between waves and coastal structures. In those regions, the flow is expected to be highly non-linear (Moretto 2020). To model flow in this circumstances, a two-phase incompressible Navier-Stokes solver was introduced to the RANS model, considering the flow of air and water together. In particular, the free surface waves are tracked with the so called Volume of Fluid (VOF) equation. This equation is implemented in the MULES technique used by OpenFoam in order to obtain a non-diffusive solution when solving transport types equations. The MULES technique is represented by the following equation:

$$\frac{\partial \alpha}{\partial t} + \frac{1}{n}[\nabla \cdot \mathbf{u}\alpha + \nabla \cdot \mathbf{u}_r(1-\alpha)\alpha] = 0 \tag{3.15}$$

Where the term $\frac{1}{n}$ guarantees that only the pores of porous material can be filled with water ($n$ is the porosity of the permeable structure), $\mathbf{u}$ is the velocity expressed in Cartesian coordinates and $\mathbf{u}_r$ is the relative velocity between fluids. Utilizing a two-phase approach leads to smearing at the interface between the two fluids, which is mitigated by the last term on the left side of the equation. This last term is activated when the indicator function $\alpha$ lies between 0 and 1. The indicator function is found by solving Equation 3.15 in every grid cell. When doing so, the volume fraction of the fluid in each cell is obtained and tracked. Dry cells are represented by an $\alpha$ value of 0, while completely wet cells have an $\alpha$ value of 1. The value of the indicator factor $\alpha$ is then used to compute properties such as the density and viscosity of every grid cell, subsequently used in the RANS equations, which provide the time-averaged velocities in each grid cell. The velocities are subsequently re-applied to equation 3.15 to re-evaluate the indicator function in each grid cell. The process is repeated for every dynamic time step. Further explanation on the VOF method can be found in Berberović et al. (2009). For the correct implementation of the method, a mesh refinement is performed around the water level, as suggested by Moretto (2020).

### 3.2.6. Turbulence modelling

Turbulence is a complex three-dimensional, time-dependent and nonlinear fluid motion. When a flow is turbulent, various length scales interact, energy transfers occur, and mixing unfolds both horizontally and vertically. As the motion progresses, energy shifts from larger eddies to smaller ones until it dissipates into heat.

The Reynolds-averaged Navier–Stokes (RANS) equations are transport equations primarily used to describe turbulent flow. In the RANS equations, flow quantities are decomposed into their time-averaged and fluctuating components (Reynolds decomposition). Employing these equations introduces an additional term in the Navier-Stokes equations presented in Section 3.2.1, known as Reynolds stress, which allows for turbulence modelling. The resolution of this term is achieved with the use of a turbulence (or closure) model. Different turbulence models have been developed to accurately model coastal turbulent processes such as wave breaking.

The formally stable $k-\omega$ closure model developed by Larsen and Fuhrman (2018) was used in this research, where $k$ represents the turbulent kinetic energy and $\omega$ is the specific turbulent kinetic energy dissipation rate. This model is particularly convenient because, by design, it defaults to a desired unmodified $k-\omega$ model in uniform boundary layer flows and other sheared regions, it is fully consistent with the Boussinesq approximation, and does not require modification of any standard closure coefficients. The model was developed as an alternative to the most commonly used two-equation closure models, that were demonstrated to be unconditionally unstable leading to asymptotic exponential growth rates

for the turbulent kinetic energy and eddy viscosity (Larsen and Fuhrman 2018).
On the other hand, the stabilized model derived by Larsen aimed at avoiding unbounded growth of turbulent kinetic energy. The model was tested and validated for problems involving both non-breaking and breaking surface waves. (Larsen and Fuhrman 2018).
To avoid the overproduction of turbulent kinetic energy, the stabilized model uses two stress limiting coefficients $\lambda_1$ and $\lambda_2$. Here, their values are set to $\lambda_1 = 0.875$ and $\lambda_2 = 0.05$, to bar the overestimation/underestimation of $k$ and $\omega$, following tests performed by Larsen and Fuhrman (2018) for breaking gravity waves.

The initial $\omega$ value is set to $\omega = \omega_\infty = 2.71\sqrt{p_0}$ = 0.043 , and the initial $k_0$ value to $k_0 = 0.1\omega_\infty\nu$ = 4.3 $\cdot 10^{-8}$. $p_0$ is calculated from Equation:

$$\langle\langle p_0\rangle\rangle = \frac{k_w^2 H^2 \sigma_w^2}{2\tanh(k_w h)} \tag{3.16}$$

Finally, the specification of the initial value of the normalized turbulent viscosity $\nu_t$ follows from the relation:

$$\nu_t = \frac{k}{\tilde{\omega}} \tag{3.17}$$

where $\tilde{\omega}$ is defined as:

$$\tilde{\omega} = \max\left[\omega, \lambda_1\sqrt{\frac{p_0 - p_b}{\beta^*}}, \lambda_2\frac{\beta}{\beta^*}\frac{p_0}{p_\Omega}\omega\right] \tag{3.18}$$

For further explanations on the parameters introduced in the Equations above, the reader is referred to Larsen and Fuhrman (2018).

Particular caution is needed when modeling turbulence together with a porous solver in OpenFOAM. In this research, the porosity model developed by Jensen et al. (2014) was employed to simulate water flow through the breakwater's porous rubble mound. Jensen et al. (2014) highlighted that the resistance coefficients used by the porous solver already account for the turbulence effects inside the porous media and no further turbulence model should be included. Furthermore, Mata and Van Gent (2023) found out that including a turbulence model in a numerical simulation that uses the porous solver results a severe effect on the flow through the porous media.
In the present case, however, it is crucial to represent the turbulent dynamics that follow from the overtopping jet falling on the lee side as accurately as possible. Therefore, a turbulence model is employed and the overestimation of turbulence in the porous media is limited by setting the $KC$ number to 10'000, as explained in Section 3.2.7.

### 3.2.7. Porosity modelling

To model flow through the breakwater's porous rubble mound, the porousWaveFoam solver, developed by Jensen et al. (2014) was used. Inside the porous media, the velocity is defined as the filter velocity $u$, related to the pore velocity $u_p$ through the following equation, where $n$ is the porosity of the medium (Barendse 2021):

$$u = nu_p \tag{3.19}$$

The continuity and momentum equation solved by porousWaveFoam are modified to take into account the porosity effects. This leads to the following modified RANS equations:

$$\nabla \cdot \langle\overline{\mathbf{u}}\rangle = 0 \tag{3.20}$$

$$(1 + C_m)\frac{\partial}{\partial t}\frac{\rho\mathbf{u}}{n} + \frac{1}{n}\nabla\cdot\frac{\rho}{n}\mathbf{u}\mathbf{u}^T = -\nabla p^* + \mathbf{g}\cdot(\mathbf{x} - \mathbf{x}_r)\nabla\rho + \frac{1}{n}\nabla\cdot\mu_{tot}\nabla\mathbf{u} - \mathbf{F}_p \tag{3.21}$$

where $\rho$ is the density of the fluid, $u$ the velocity vector in Cartesian coordinates, $t$ the time, $\mathbf{x} = (xyz)$ the Cartesian coordinate vector, $\mathbf{x}_r$ the reference location, $p^* = p - \rho g \cdot \mathbf{x}$ the excess pressure and $\mu_{tot}$ the total dynamic viscosity (Jensen et al. 2014). $C_m$ defines the added mass coefficient, where $\gamma_p$ is a closure coefficient, set to 0.34:

$$C_m = \gamma_p \frac{1-n}{n} \tag{3.22}$$

The flow resistance imposed by the porous media, $\mathbf{F}_p$, is described by the Darcy-Forchheimer resistance equation:

$$\boldsymbol{F}_p = a\boldsymbol{u} + b\rho\|\boldsymbol{u}\|_2\boldsymbol{u} \tag{3.23}$$

This equation includes linear, non-linear and inertia forces to account for accelerations. When the first term dominates, the flow behaves as laminar, while if the second term dominates, the flow behaves as turbulent.

$a$ and $b$ are resistance terms defined by Van Gent (1995) as :

$$a = \alpha \frac{(1-n)^2}{n^3} \frac{\nu}{{d_{n50}}^2} \tag{3.24}$$

$$b = \beta \left(1 + \frac{7.5}{KC}\right) \frac{1-n}{n^3} \frac{1}{d_{n50}} \tag{3.25}$$

In equations 3.24 and 3.25, $\nu$ is the kinematic viscosity, while $d_{n50}$ is the nominal diameter of the porous material. $\alpha$ and $\beta$ are called resistance coefficients. These coefficients were originally introduced by Van Gent (1995), who performed experiments for stationary and oscillating flow, concluding that their value should be set to $\alpha$ = 1000 and $\beta$ = 1.1. However, the determination of the resistance coefficients is highly empirical, and many other values have been proposed in literature. Losada et al. (2008) elaborated on the complexity of resistance coefficients, noting that those determined by Van Gent (1995) might not be valid under oscillatory flow conditions and waves propagating and breaking over slopes. He emphasized the numerous parameters influencing these coefficients, including the Reynolds number, the shape of the stones, the grade of the porous material, the permeability, and flow characteristics. However, the precise description of these parameters is still not completely understood for waves propagating over slopes such as rubble mounds. Based on a comparison of experimental data and numerical results, Losada proposed average values of $\alpha$ = 200 and $\beta$ = 0.8. Further studies from Jensen et al. (2014), suggested values of $\alpha$ = 500 and $\beta$ = 2.0 to consider all possible flow regimes in porous media. Mata and Van Gent (2023) suggest to avoid using too low values of the coefficients because they can result in the generation of numerical dissipation in OpenFoam. In their test, the original values recommended by Van Gent (1995) were used. In this study, the values suggested by van Gent, Losada and Jensen are all tested to determine which sets performs better for the current experiment.

In equation 3.25, $KC$ is the Keulegan-Carpenter number, which describes the relative importance of the drag forces over inertia forces in oscillatory fluid flow. Small $KC$ numbers are observed when inertia dominates, while large $KC$ numbers are typical of dominating drag forces.
Studies by Jacobsen et al. (2018) disregarded the contribution of the $KC$ number by assigning it a very high value. This is equal to limiting the influence of oscillatory movement in the estimation of the nonlinear drag coefficient in the porous media. Moreover, Jacobsen et al. (2015) highlighted how the estimation of the $KC$ number is difficult and not fully understood yet. Additionally, due to the rapid damping of wave energy through the permeable structure, the $KC$ number should ideally be used with a temporal and spatial distribution.
To limit the overestimation of turbulence in the porous media, as explained in Section 3.2.6, this study also limited the influence of the oscillating flow, setting the $KC$ number to a default value of 10'000.

Porous zones were implemented in OpenFOAM using the porosityZones dictionary in waves2Foam. Apart from specific parameters of the Darcy-Forchheimer equation, such as $\alpha$, $\beta$ and the $KC$ number,

parameters typical of the breakwater model used in the experiments were also specified in OpenFOAM. These include the median diameter $d_{50}$ and the porosity of the layers $n$.
The median diameters were directly estimated from the grain size distribution of the three layers. Specifically, they were imposed to 0.0135 m 0.0085 m, 0.0083 m respectively for for the external, intermediate and core layer.

To calculate the porosity, many empirical formulas exist. In this thesis, the approach presented in the Rock Manual (CIRIA 2007) and highlighted by Moretto (2020) was used. The porosity is estimated based on the grain size distribution parameters of the Rosin-Rammler (Ros-Ram) curves, such as the uniformity index $n_{RRD}$.
The bulk porosity is obtained following the equation:

$$n_v = \frac{1}{90} \cdot (e_0) \cdot \arctan\left(0.645 \cdot n_{RRD}\right) \cdot \frac{180}{\pi} \tag{3.26}$$

In Equation 3.26, $e_0$ is the void ratio associated to the single-size particles of different shapes and it typically ranges between 0.92 and 0.96. Here the average value 0.94 is taken. The uniformity index $n_{RRD}$, describes the shape of the Ros-Ram curve and is used to measure the uniformity of a particle size distribution. To obtain the uniformity index, the nominal lower limit mass (NLL) and the nominal upper limit mass (NUL) of the gradings are needed. These parameter were obtained from the sieve curves of the rubble mound layers, applying the relations $M = {d_n}^3 \rho$ and $d_n = 0.84d$. For coarse grading aggregates, with diameters lower than 200 mm, the NLL and NUL masses are determined based on the allowable passing fractions of 10% and 95%, respectively. The resulting bulk porosity values were imposed to 46.93%, 36.16% and 35.28% respectively for the external, intermediate and core layers.

## 3.3. Numerical set-up

### 3.3.1. Computational domain

Two computational domains were defined and merged together in order to simulate the whole physical flume used by Van Balen (2023). In OceanWave3D, a two-dimensional numerical domain was defined as a 100 m long flume. The origin of the flume, $x$ = 0 m is the location where the paddle velocity signal was imposed and corresponds with the physical position of LWG2. The OCW3D flume had an horizontal bottom for its entire length. The interface between OceanWave 3D and OpenFOAM is located at $x$ = 20 m. Here, the wave was transferred to OpenFOAM. The OpenFOAM domain starts at $x$ = 20 m and and extends to $x$ = 81 m. It is composed of a flat bed that extend to $x$ = 38.1 m, followed by a bed inclined with an angle 1:30 in accordance with the experimental flume.
In the OpenFOAM domain, the breakwater was inserted , with the toe of the rubble mound 34.95 m far from the origin.
The OpenFOAM domain also included a part of free beach after Still Water Level. This was done to completely reproduce the experimental flume without removing the effect of wave reflection that influenced results on the rear side of the structure. However, the physical flume also included a rough board placed after Still Water Level that simulated a mangrove forest. The roughness board was capable to limit the run up of water on the beach causing more reflection of water from the beach to the breakwater. In OpenFOAM, this configuration was not implemented, and less reflection was observed on the lee side causing lower elevation values after the transit of the wave and the end of overtopping.
The employed OpenFOAM domain was also two - dimensional, and extended for 2 m in the $y$ direction.

Two relaxation zones were inserted in the numerical flume. The first one, at the beginning of the OpenFOAM domain, was used for wave transferring from the OceanWave3D domain. Moreover, one relaxation zones was imposed at the end of the domain to absorb the incoming wave and avoid wave reflection in the OceanWave3D flume.
In figure 3.4, a sketch of the numerical flume with the imposed relaxation zones is given.

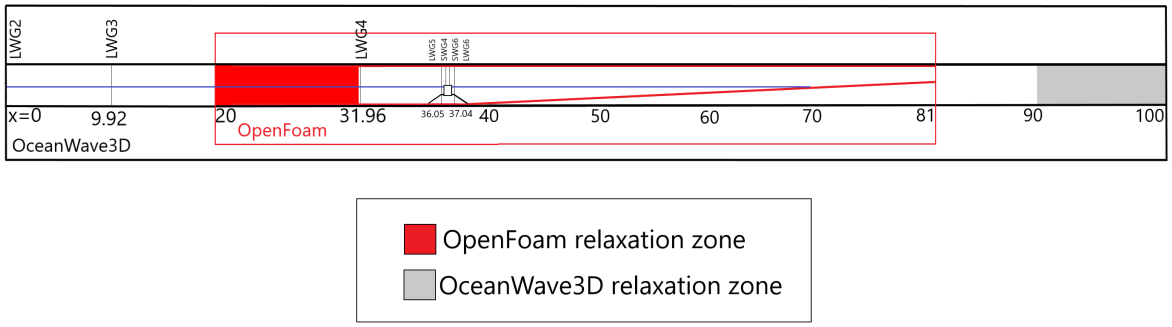


**Figure 3.4:** The numerical flume implemented in this research.

In the numerical flume employed in OpenFOAM, wave gauges were located at the same locations as LWG4, LWG5, SWG4, SWG6 and LWG6 close to the breakwater and on top of it, to validate the model against physical elevation data. Additionally, two wave gauges were placed at the seaward and landward edges of the caisson to have further information on the evolution of the numerical elevations on top of it.

### 3.3.2. Mesh Resolution

After the set up of the flume geometry, the two dimensional mesh was generated, following recommendations given by Jacobsen et al. (2012). A structured mesh, formed by cells of hexahedral shape, was used since it is generally more accurate and less computationally expensive than unstructured ones. Moreover, the aspect ratio $\frac{\Delta x}{\Delta y}$ was kept to 1 throughout the computational domain to improve the accuracy and numerical stability of the model, as suggested by Jacobsen et al. (2012).

#### OceanWave3D

The mesh resolution In OCW3D was tested upon conducting a sensitivity analysis to reach grid convergence. The detailed results of the analysis are shown in the Appendix B. The aim of the sensitivity, or grid convergence analysis, was to make the computational solver independent of the mesh. By doing so, the final mesh that was used better represented the matching between experimental and numerical data. The resolution was tested according to the recommendations given by literature on numerical modelling of tsunami waves.

The JIP CoastalFOAM program recommended the use of more than 10 cells per leading wave length. Moretto (2020) suggested to use 165 cells per wave length. For the vertical refinement, the resolution is determined prescribing a certain number of layers in OceanWave3D. Jacobsen et al. (2018) used 12 layers for vertical resolution of OceanWave3D with good outcomes, Mata (2021) used 11 to 16 layers. Following these recommendations, three horizontal and three vertical resolutions were tested in OceanWave3D. The final resolution in the OceanWave3D domain was 12 layers in the vertical direction and a $\Delta x$ of 12 cm, corresponding to 833 grid points in the x direction. The resolution was obtained following the sensitivity analysis described in Appendix B and comparing the Root Mean Square Errors (RMSE) between the experimental elevation timeseries and the numerical ones. The RMSE quantifies the average difference between two datasets, experimental and numerical elevations in this case. A lower RMSE value indicates a smaller discrepancy between the experimental and numerical signals.

The E20 wave length L can be estimated as $L = c \cdot T$ where T is the wave period and c is the celerity. Assuming a celerity of 3.36 m/s as measured by Van Balen (2023) at LWG5 and a period of 20s for the E20 wave, the resulting wave length is 67.2 m. Using 833 cells ensures that the recommendation suggested by Moretto (2020) was followed.

OpenFOAM

Also for the OpenFOAM domain, a grid convergence study was performed following the recommendations given in previous studies. The detailed results of the grid convergence analysis are presented in Appendix C. Madsen et al. (2008) recommended to use at least 100-150 cells per wave length and not less than 5-10 cells over the wave height for the vertical resolution.
Mata (2021) used 9 to 21 cells per wave height as a resolution close to the free surface. The number of grid cells per wave height is usually normative to define the resolution in OpenFOAM. The resolution is usually studied determining the number of cells based on the wave height and keeping the aspect ratio to 1. Therefore, the resolution in OpenFOAM was tested considering the height of the E wave in this research. The same resolution was then always applied in the horizontal direction, so that the aspect ratio was maintained at 1.

Based on the elevation timeseries observed in the physical experiments, different areas of refinement were defined in the OpenFOAM domain. A base, coarse mesh was defined in the whole domain, and progressive refinement zones were prescribed in areas of interest. A first refinement zone was applied around the SWL, 0.2 m above and below it, offshore and onshore of the breakwater, to correctly capture the surface elevation evolution. Another refinement zone was applied in the region of the porous layers, as well as around the caisson. This was done to ensure that the caisson and porous layers matched as much as possible the original geometries, since the "SnappyHexMesh" feature of OpenFOAM follow the mesh edges to define the breakwater shape. To measure wave elevations and pressure distributions behind the caisson, and correctly capture the amount of water overtopping the caisson, two final refinement zones were defined on top of the caisson, and behind it extending to the location of LWG6. Each refinement zone was assigned a number of refinement levels ($nrf$). If the resolution of the base mesh is $\Delta x_{base}$, the resolution of every refinement zone is equal to:

$$\Delta x_{refined} = \frac{\Delta x_{base}}{2^{nrf}} \tag{3.27}$$

The number of refinement levels for every refinement zone varied between different simulations to study the effect of the grid dimension on the results.
When performing the sensitivity analysis of the OpenFOAM mesh, three resolutions were tested in front of the caisson and around the SWL: $\Delta x$ = 1.5 cm, $\Delta x$ = 0.75 cm and $\Delta x$ = 0.625 cm. . In fact, it was crucial to obtain reliable elevation values in front of the caisson for correct representation of wave-induced hydrostatic pressures. In the remaining region below SWL, the resolution can be coarser to save computational time. With an offshore wave height $H = 7.2$ cm, and considering that the aspect ratio of the mesh $\frac{\Delta x}{\Delta y}$ is always kept to 1, the three resolutions tested correspond respectively to 5, 10 and 12 cells per offshore wave height. Both resolutions of $\Delta x$ = $\Delta y$ = 0.625 cm and $\Delta x$ = $\Delta y$ = 0.75 cm around the water surface and in front of the caisson showed good reproduction of the elevation time series offshore and pressure records, with a mean RMSE of 0.01 cm at LWG5. Given the very small difference in results between the two meshes, a final resolution of $\Delta x$ = $\Delta y$ = 0.75 cm was chosen, to save computational time while still having a good representation of the experiment in the first part of the flume. The base mesh in the OpenFOAM domain had a resolution of 6 x 6 cm. Hence, three levels of refinement were applied offshore of the caisson. Subsequently, three resolutions were tested on top of the caisson, namely $\Delta x$ = 0.75 cm, $\Delta x$ = 0.375 cm and $\Delta x$ = 0.188 cm, further refining the region. With a maximum elevation of 3.2 cm above the caisson's top, these resolutions correspond to setting 4, 8 and 17 cells per wave height. A resolution of $\Delta x$ = 0.375 cm was finally employed on the top region of the caisson, corresponding to four further levels of refinement. Starting from this resolution, different refinements were tested behind the caisson, namely $\Delta x$ = 0.75 cm, $\Delta x$ = 0.375 cm and $\Delta x$ = 0.188 cm. With a mean elevation of 1.35 cm recorded at LWG6 as a consequence of overflow, the three resolutions correspond to imposing respectively 2, 4 and 7 cells per wave height. Surprisingly, on the lee side of the caisson, the resolution that produced best results was $\Delta x$ = 0.75 cm, as shown in Chapter 4.
The mesh was generated in OpenFOAM through the "BlockMesh" utility, and then refined with the "SnappyHexMesh" dictionary.

The detailed informations and results of the OpenFOAM sensitivity analysis are shown in Appendix C. The final configuration of the OpenFOAM domain with its refinement zones is shown in Figure 3.5.

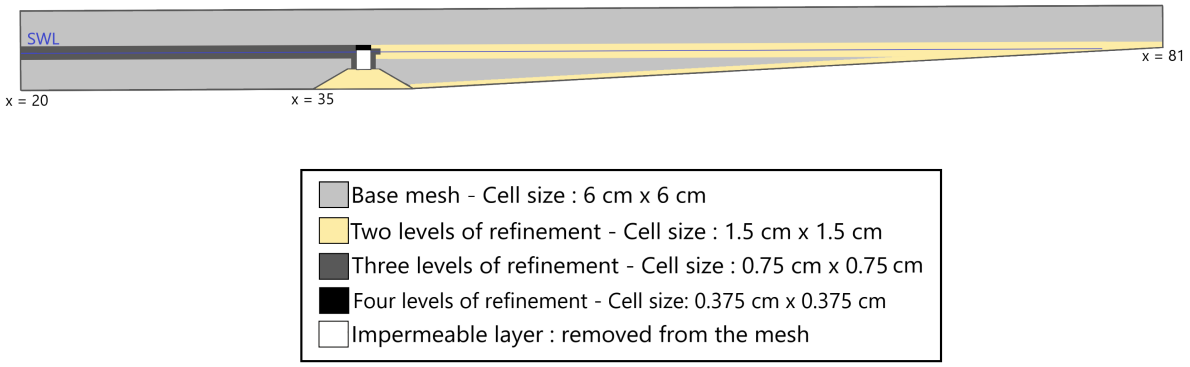


**Figure 3.5:** The refinement zones defined in the final OpenFOAM domain

### 3.3.3. Temporal resolution

The temporal resolution of a numerical scheme must be chosen such that the Courant-Friedrichs-Lewy (CFL) condition is satisfied for the convergence of the solution. The CFL condition is satisfied if the full numerical domain of dependence contains the analytical domain of dependence. This ensures that the information does not travel faster than the distance between mesh elements. The CFL condition, necessary for the stability of numerical models, is defined by the Courant Number $C_O$ which must be smaller than a maximum allowable value :

$$C_O = \frac{u\Delta t}{\Delta x} \tag{3.28}$$

where $u$ is the velocity , $\Delta t$ the time step and $\Delta x$ the space resolution.
For the free surface time integration, the explicit four-stage, fourth-order Runge Kutta scheme is applied in OCW3D. The maximum Courant number prescribed in OCW3D is 0.8. On the other hand, OpenFOAM has larger Courant restriction and allows lower maximum Courant Number than OceanWave3D. In OpenFoam, the $\Delta t$ is adapted at every iteration and is constrained by the imposed $C_{O,max}$.
Larsen et al. (2019b) studied the performance of the interFoam solver when simulating progressive waves. They concluded that using a low value of the $C_O$ number, namely 0.05, would limit problems that the interFoam solver could present when simulating gravity waves, such as increasing wave heights, a wiggled interface between water and air, spurious air velocities, and severely overestimated velocities near the crest. Following their recommendations, a maximum Courant number of 0.05 was used in this research.

When the two softwares are coupled, OpenFOAM adjusts the time step of OCW3D so that the numerical stability is not compromised in the coupling.

### 3.3.4. Wave generation

The wave generation was done with OceanWave3D, imposing Equation 3.14, where $u_p$ is the paddle horizontal velocity, as an inlet boundary condition. The paddle velocity timeseries was obtained imposing the continuity equation (3.8) as a mass balance between the vertical displacement of the paddle and the volume of water transported by the crest of the wave and using the shallow water approximations. This equation was integrated with the values recorded at LWG2. The paddle velocity signal was extrapolated with a timestep $\Delta t$ = 0.01 s The signal was imposed at the location of LWG2 in the numerical flume, which acts as inlet boundary and origin of the domain in OceanWave3D. As a consequence, the other LWGs and the breakwater are at a relative distance from the location of LWG2.

### 3.3.5. The numerical breakwater

In the numerical flume, a breakwater was inserted in the OpenFOAM domain representing the same model used in the physical experiments and described in Section 3.1.4. The impermeable caisson was recreated in the numerical flume extruding it from the domain with the ”SnappyHexMesh” utility. Also the concrete protection blocks placed at its bottom edges were impermeable and therefore removed from the domain.

To accurately reproduce the rubble mound, the geometries of the three layers were recreated and different porosity parameters were assigned to each layer. Using the ”TopoSet” dictionary, the layers geometry were recognised as regions in the mesh. Subsequently, the regions were set to porosity zones using the ”porousWaveFoam” solver, which reads a ”porosityZones” dictionary, containing porosity parameters for each layer. The implemented numerical breakwater was symmetric to the physical one shown in Figure 3.2a, as the inlet was imposed on the left boundary in OceanWave3D.

The three porous layers were formed by aggregate with different dimensions, as explained in Section 3.1.4 . Section 3.2.7 gives an outlook on the porosity parameters that were used to define the different porous layers. The measurement of pressures on the caisson’s faces was done with OpenFOAM placing pressure probes at the same location as in the physical structure and additionally measuring the pressures values at every cell at the interface with the caisson. Moreover, the total horizontal and vertical forces timeseries acting on the caisson were extrapolated using the ”forces” function.

# 4

# Results

In this section, the results of both the physical experiment and numerical simulations are presented. First, a detailed analysis of the outcomes from the experiments is provided. Next, the results of the numerical modeling experiments are shown, validating the numerical model against the physical experiment. The performance of the numerical model is further evaluated by comparing experimental and numerical pressure distributions at critical instants and by assessing the stability of the caisson using the numerical model.
Results are presented for the E20 wave experiment. The wave correspond to an elevated wave with a period of 20 s, corresponding to a prototype period of 140 s. The shape of the wave can be visualized in Figure 2.3. The period is here defined as the distance in time when $\eta(x,t)$ first up-crosses and then first down-crosses the value corresponding to 1% of the positive amplitude $a+$. Because of the particular shape of elevated waves, the amplitude corresponds to the wave height and to the water surface elevation above still water level. The E20 wave is the shortest and most impulsive wave simulated in the experiments. This makes its analysis of particular interest, because it is the one that is expected to exert the highest forces on the breakwater, as highlighted by Van Balen (2023).

## 4.1. Physical experiment results

### 4.1.1. Wave generation and propagation

The wave was generated by the tsunami simulator (TS) located at $x$ = 0 m in the flume and propagated over a distance of 52.07 m before hitting the breakwater's rubble mound toe. A sketch of the flume used in the experiments is presented in Figure 3.1. Appendix A presents the graphs illustrating the evolution of surface elevation at wave gauge locations following wave propagation along the flume. At the location of LWG2, 17.11 m away from the TS tip, the maximum recorded value, corresponding to the wave crest elevation was 7.16 cm. The elevation was almost unchanged at LWG3, located 10 m away from the previous wave gauge. However, at LWG4, the peak elevation significantly increased up to 12.48 cm. This is due to the close proximity of LWG4 to the slope of the breakwater. Shoaling above the rubble mound and partial reflection of the wave at the caisson's front caused increase in the water level. The increase was even stronger at LWG5, located at the top of the rubble mound, 53.16 m away from the TS. Here, partial shoaling above the porous rubble mound played a significant role and the maximum recorded value was 13.27 cm. At $t$ = 99 s from the beginning of the experiment, the long wave began impacting the caisson, resulting in increased pressure values recorded by the sensors on the front face. The peak of the wave reached the caisson approximately 10 seconds later, at around $t$ = 110.5 s, when LWG5 recorded the maximum surface elevation, and the sensors on the caisson's front face registered the highest pressure values.

On top of the caisson, two short wave gauges recorded the overtopping water surface elevation. The overtopping process started about 5 seconds after the time of first impact of the wave on the caisson's

front face, and lasted for approximately 12 seconds. The maximum elevation values recorded on the top of the caisson were lower than the ones recorded in front of the structure. The overtopping water profile, sketched in Figures 4.4b and 4.4c resembled the shape of the overflow over a broad-crested weir. Broad crested weirs are observed when 0.08<$H_1/L$<0.33, where $H_1$ is the total energy head upstream of the caisson and L is the length of the caisson (Goodarzi et al. 2012).

On the backside of the breakwater, a long wave gauge (LWG6) was positioned immediately after the caisson. The elevation recorded from this gauge showed an initial increase, corresponding to the time when the overtopping jet reached the caisson's lee side and caused a rise in water level. This initial elevation increase was not stable: it exhibited many small amplitude fluctuations, consistent with the instrument's response when a biphasic fluid flows through it, as explained in Section 3.1.5.
After this elevation increase, which lasted about as long as the overtopping event, a second, higher peak followed half a minute later. The latter was caused by partial reflection of the wave on the lee side of the breakwater and oscillations in the flume generating from the passage of the E wave. The analysis on the lee side only focused on the first elevation and pressure peak, as it is the one directly caused by the E wave.

### 4.1.2. Pressure distribution on the caisson

The caisson was equipped with 12 pressure sensors, each calibrated to measure zero pressure under stillwater conditions. Because of this, the hydrostatic pressure was not included in the measurements. To estimate the total pressure, the hydrostatic pressure must be added to the recorded one:

$$p_{tot} = p_{record} + p_{hydrostatic} \tag{4.1}$$

where $p_{record}$ is the pressure recorded by the sensor, resulting from the wave action, and filtered with a LPF as explained in Section 3.1.5, while $p_{hydrostatic}$ is the stillwater hydrostatic contribution obtained from Equation 3.7.

Like the elevations, the time series of the total pressures exerted on the sensors located on the seaward face of the caisson displayed an initial peak followed by multiple other ones. The initial peaks coincided with the increase caused by the wave overtopping the caisson and being transmitted through the rubble mound. In contrast, the following pressure peaks resulted from partial wave reflection on the lee side and oscillation of the water surface following the wave transit. Only the first pressure increase was analyzed since it is the one directly caused by the E20 wave.

#### Pressure evolution on the front face of the caisson

Figure 4.1 shows the evolution of total, hydrostatic and hydrodynamic pressure timeseries obtained from the pressure sensors located on the seaward side of the caisson. Only the time series relative to the deepest sensor PT3 and the shallowest PT05, located out of water in still water conditions, are shown. In Appendix A, the plots are shown for every pressure sensor. The total pressure is comprehensive of both a hydrostatic and a hydrodynamic wave-induced pressure component and follows from Equation 4.1. The hydrostatic pressure components, in orange, were obtained summing the still water hydrostatic pressure value acting on a sensor to the time-variant increment caused by the variation in the surface elevation measured at LWG5, located just 25 cm away from the caisson. Equation 3.7 was used, where $h$ is imposed as the depth of the pressure sensor below the wave free surface. The dynamic component of the total pressure was calculated by subtracting the hydrostatic pressure from the total one. To remove small oscillations and negative hydrodynamic pressure values, resulting from the subtraction procedure, a Low Pass Filter with a cut-off frequency of 0.3 Hz was applied and negative values were set to zero.

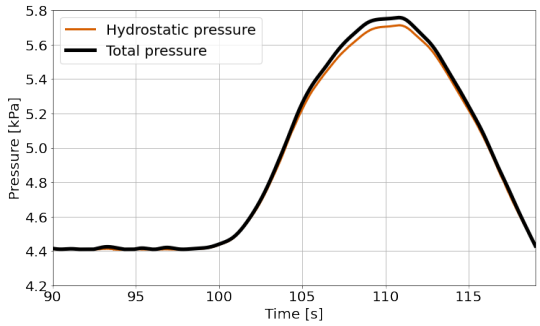


**(a)** Pressures at pressure sensor PT3

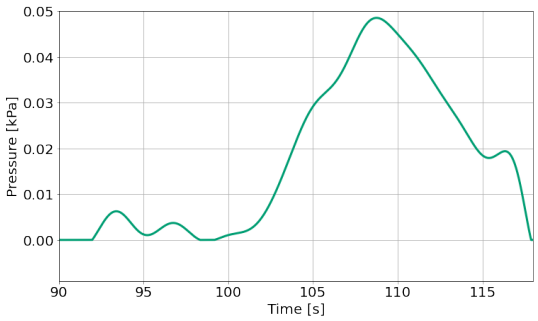


**(b)** Hydrodynamic pressures at pressure sensor PT3

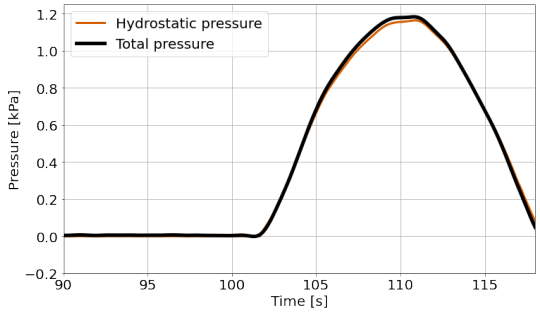


**(c)** Pressures at pressure sensor PT05

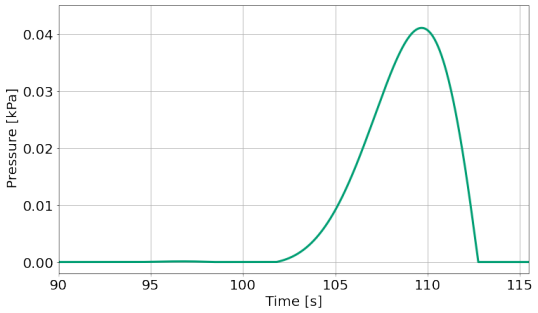


**(d)** Hydrodynamic pressures at pressure sensor PT05

**Figure 4.1:** Total, hydrostatic and hydrodynamic pressure in front of the caisson

In the front face, it is evident that the hydrostatic pressure component predominantly contributed to the total pressure acting on the caisson, as already observed by Van Balen (2023). The hydrostatic distribution of pressures in long waves, such as tsunamis, was also noted by Schiereck and Verhagen (2012). For all the sensors, the hydrodynamic contribution showed no significant change in magnitude, accounting for up to 0.06 kPa. Although the magnitude remained relatively constant, the relative contribution of the hydrodynamic pressure component increased closer to the still water level. The maximum contribution was in fact recorded by PT05, located just outside the still water level, where the hydrodynamic pressure accounted for 3.71 % of the total. For this sensor, the hydrostatic pressure was determined subtracting a value $z_{PT05}$ from the elevation at LWG5, corresponding to the distance between the sensor and the still water level. Conversely, the total pressure is simply the pressure recorded by the sensor. The lowest contribution of the hydrodynamic component was experienced by the deepest sensor, PT3, where the hydrodynamic pressure was only 0.78 % of the total measured one. Overall, the hydrodynamic component of the pressures on the front face remains negligible, with the hydrostatic component being dominant. Neglecting the hydrodynamic component would introduce an error of less than 4 % in pressure calculations.

### Pressure evolution on top of the caisson

A more significant contribution of the hydrodynamic pressure was observed on the top face of the caisson. Although this face was not submerged in still water conditions, it experienced overtopping from $t$ = 105 s to $t$ = 116 s approximately, as suggested by the analysis of the elevation records. The only pressure sensor on the top of the caisson, PT08, recorded a maximum hydrodynamic pressure that constituted about 35 % of the total peak pressure of 0.47 kPa. This contribution was however not constant and was lower during the initial and final phases of overtopping. In this case, the surface elevation used to calculate the hydrostatic pressure contribution was measured by SWG4, located on top of PT08.

### Pressure evolution on the rear of the caisson

Figure 4.2 presents a close-up view of the filtered pressure records at the deepest (PT4) and shallowest (PT07) sensors positioned on the lee side of the caisson. These time series indicate a pressure peak resulting from both caisson overtopping and transmission of the wave through the rubble mound.

Unlike the relatively stable pressure records in front of the caisson, the pressure and elevation time series behind it exhibited numerous small amplitude oscillations. These oscillations were partially mitigated applying a low-pass filter with a cut-off frequency of 0.3 Hz. The pressure fluctuations were attributed to the presence of air bubbles mixed with water in the turbulent structures that develop when the overtopping jet fell on the lee side of the caisson. This phenomenon caused some air entrainment, complicating the measurements taken by the sensors on the lee side, as detailed in the Methodology (Section 3.1.5).

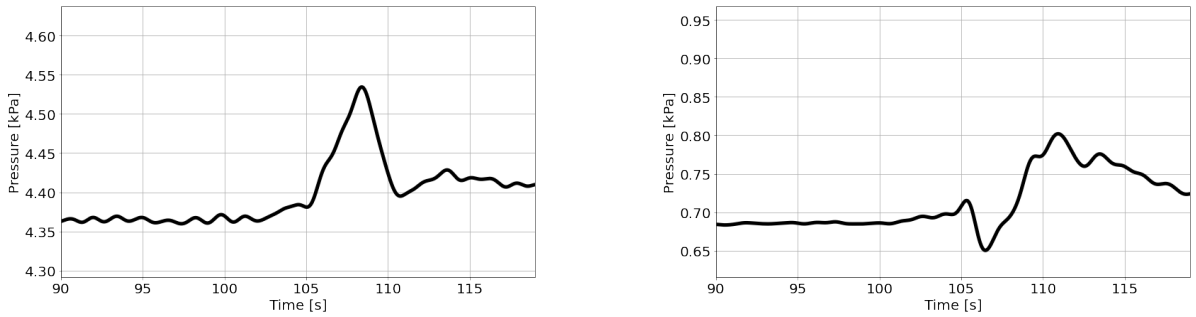


**(a)** Pressure at pressure sensor PT4

**(b)** Pressure at pressure sensor PT07

**Figure 4.2:** Pressure time series behind the caisson

Because of the biphasic nature of the fluid on the lee side, it was difficult to distinguish between the hydrostatic and hydrodynamic contribution of the pressure.
Hsu et al. (2022) noted that dynamic pressure exerted on the rear face of caissons overtopped by waves may not be negligible. However, this analysis indicates that the total pressures on the rear side did not significantly deviate from the still water hydrostatic pressures. In fact, at $t$ = 110 s, corresponding to the time of averagely maximum pressures on the caisson, the total pressure recorded by the sensors was, on average, only 5% higher than the still water hydrostatic one. This suggests that the pressure distribution on the lee side of the caisson can be assumed to be primarily hydrostatic, despite the pressures associated with the plunging jet falling behind the caisson.

### Pressure evolution on the bottom face of the caisson

On the underside of the caisson, the two sensors PT1 and PT2 recorded slight differences in pressure magnitude when hit by the wave, with PT2 displaying marginally lower pressure values compared to PT1. This suggests a trapezoidal distribution of pressure on this face.
The hydrostatic pressure contribution on the bottom face of the caisson is influenced by the water surface elevation upstream and downstream of the caisson. However, due to the absence of wave gauges close enough to the caisson edges, it was difficult to calculate precise values for the hydrostatic and hydrodynamic pressure contributions on the bottom face. The wave gauges on the top of the caisson are located in an area where the overtopping process resembles the flow over a broad crested weir. Goodarzi et al. (2012) observed that water passes from a sub-critical to a super-critical state when flowing over such structures. As a consequence, the elevations measured on top of the caisson cannot be used to accurately estimate the hydrostatic and hydrodynamic contribution of pressure on the bottom, since they are located between two critical depths, while the gradient in elevations upstream and downstream of the caisson should be used. Using the average of the elevations measured upstream at LWG5 and downstream at LWG6, the hydrodynamic contribution to the total pressure was found to be negligible on the bottom side of the caisson.

Figure 4.3 as a reference, shows the evolution of the total pressure records at PT1 and PT2, located on the bottom of the caisson, as illustrated in in Figure 3.2b.

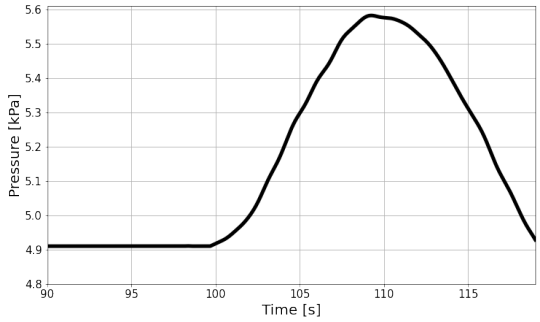


**(a)** Pressure at pressure sensor PT1

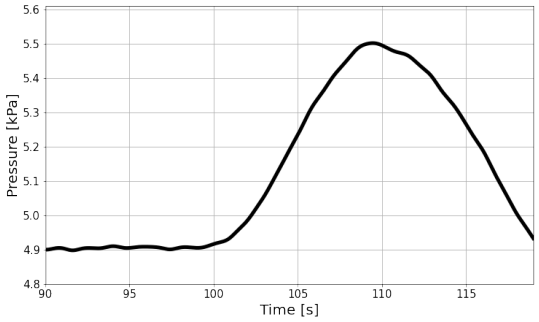


**(b)** Pressure at pressure sensor PT2

**Figure 4.3:** Pressure evolutions on the bottom of the caisson

### Pressure distributions on the caisson

Figure 4.4 show the distribution of pressures on the caisson in 4 different moments during the recreated tsunami event. The pressure values are known only at the locations of the probes (black dots in the Figures), while the distribution between these values was assumed. The pressures at the corners of the caisson in the front and back face were extrapolated from the measured values, assuming hydrostatic distribution and using the elevations at SWG6 for the values on top of the lee side. Due to the isotropic nature of pressure, the values at the same corner in the top and bottom faces were imposed identical to the extrapolated ones in the adjacent faces. This resulted in sharp and unrealistic gradients in the bottom face of the caisson. To clarify the actual pressure distribution on the caisson, the numerical model developed in this thesis was used to plot the distributions at corresponding times in Section 4.2.4.

Figure 4.4a displays the stillwater hydrostatic pressure. Experimental pressure distributions are then illustrated at key time points: at $t$ = 106 s, marking the onset of overtopping reaching the back of the caisson, at $t$ = 110.5 s, corresponding to peak pressures on the frontface, and at $t$ = 117 s, when the overtopping flow ceased.

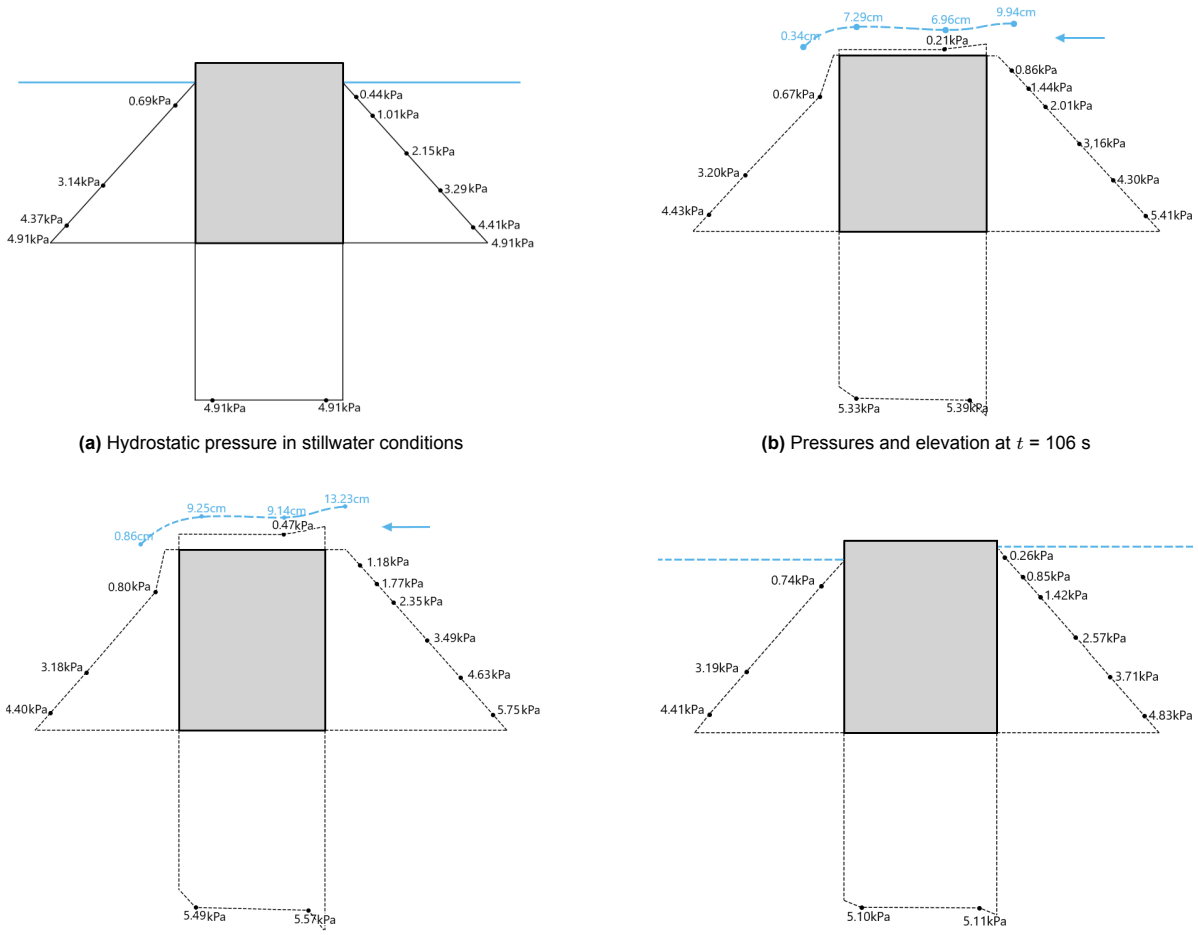


**(a)** Hydrostatic pressure in stillwater conditions

**(b)** Pressures and elevation at $t$ = 106 s

**(c)** Pressures and elevation at $t$ = 110.5 s

**(d)** Pressures at $t$ = 117 s

**Figure 4.4:** Pressure evolution over time

### 4.1.3. Forces on the caisson

In this section, the forces exerted on the caisson's faces are integrated to assess the stability of the caisson in a real scale tsunami event represented by the E20 wave.

#### Horizontal force

The force acting on a caisson's front and back face can be obtained by integration of the pressures over areas delimited by two subsequent sensors, as shown in Figure 4.6. The pressure distribution was assumed linear between the two sensors, and the lines delimiting the trapezoids are the time variant total pressure timeseries.

Following this approach, the total forces acting on the front and rear face were obtained by summing the forces identified as areas of the trapezoids:

$$F_{front} = F' + F3 + F01 + F02 + F03 + F04 + F05 \tag{4.2}$$

$$F_{rear} = F'' + F4 + F06 + F07 \tag{4.3}$$

where every force $F$ corresponds with the pressure values multiplied by the corresponding surface area. The total horizontal force acting on the caisson was determined subtracting the force exerted on the lee side of the caisson from the force acting on the front side. It should be acknowledged that the force distribution on the lee side is particularly uncertain and the zero pressure value was imposed at the free surface measured at SWG6.

Figure 4.5 shows the total horizontal force timeseries. Positive values of the force correspond to a vector aligned with the streamwise direction. The maximum horizontal force exerted by the E20 wave on the caisson amounts to 0.71 kN.

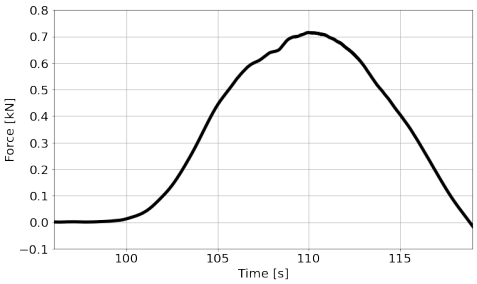


**Figure 4.5:** Total horizontal force on the caisson

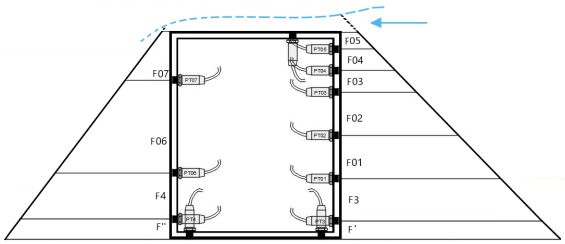


**Figure 4.6:** Force calculation method

### Uplift force

To compute the uplift force acting on the bottom of the caisson, a similar approach was adopted, dividing the bottom in two areas and assuming a linear distribution of the pressure on the bottom, extrapolating the pressure values at the edges. The force exerted on top of the caisson caused by wave overtopping, obtained assuming an uniform distribution of the pressures, was subtracted. The resultant uplift force is depicted in Figure 4.7, with positive values indicating a force acting from the bottom of the flume towards the caisson. The uplift force exhibited a double-peak distribution. Hsu et al. (2022) attributed this shape to caisson overtopping. In fact, the wave's transmission through the rubble mound resulted in a single-peaked uplift force time series. However, the peak splitted into two smaller ones during overtopping, due to the force exerted by the overtopping volume of water that acted in negative direction and was subtracted from the positive one.

The maximum resultant uplift force, given by the contribution of the pressures on the bottom face, the buoyancy of the structure, and the overtopping, was 2.42 kN.

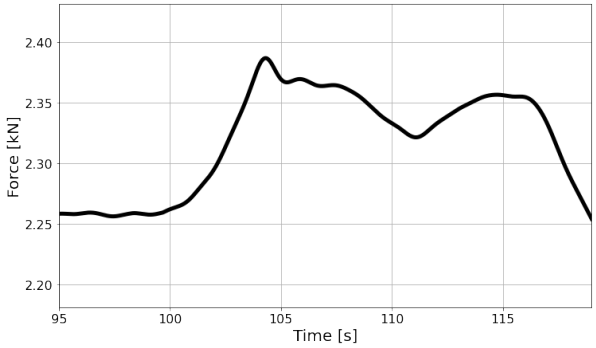


**Figure 4.7:** Total uplift force on the caisson

## 4.1.4. Caisson Stability

Numerous studies were conducted to analyse the mechanisms that caused the failure of the Kamaishi breakwater after the 2011 Great East Japan Tsunami. Among these, Arikawa et al. (2012) stated that the fall of back surface pressure caused by the water level differences during overflow, and the scouring process of the rubble mound, made the breakwater extremely vulnerable and led to caissons deformation and sinking inside the breakwater riprap, as well as sliding towards the landward direction.

Although the determination of the failure causes in complex cases is not trivial, composite breakwater stability can be assessed analysing the three most common ways of failure: sliding and overturning of

the caisson and collapse of the foundation. This section assesses the sliding and overturning stability of the prototype caisson that served as inspiration for the laboratory experiment. The experiment was scaled down to 1:50 following Froude scaling rules. To evaluate the stability of the prototype, all quantities were scaled as per Table 3.1, with a scale factor $n_L = 50$.

The stability against sliding and overturning can be calculated by means of Safety Factors (SF), defined as follows by Veraghen and Van Den Bos (2017):

$$SF_{sliding} = \frac{\mu(W - U)}{P} \tag{4.4}$$

$$SF_{overturning} = \frac{(W_t - M_U)}{M_P} \tag{4.5}$$

Where $\mu$ is the friction coefficient between the caisson and the stones of the rubble mound, usually taken as 0.6 between concrete and rubble stones. $W$ is the weight of the caisson per unit length in still water, $U$ is the total uplift pressure per unit length of the caisson and $P$ the total horizontal force per unit length of the caisson. $t$ is the horizontal distance between the center of gravity and the heel of the caisson, $M_U$ the moment of total uplift pressure around the heel of the caisson and $M_P$ the moment of total wave pressure around its heel.
Both safety factors are required to be greater or equal than 1.2 in vertical breakwater design.

The caisson used in the experiment was a wooden structure measuring 0.46 m in length and 0.56 m in height. These dimensions correspond to a prototype caisson that is 23 m long and 28 m tall.

### Caisson's weight

The first step in determining the safety factor involves calculating the weight of the prototype caisson. The method outlined in Veraghen and Van Den Bos (2017) was employed here. The specific weight of typical caissons is $\gamma_c$ = 22.55 kN/m$^3$ for the part above SWL, and $\gamma_c'$ = 20.59 kN/m$^3$ for the part below SWL. The variation in specific weights reflects the common practice of sand filling in the cells of concrete caissons.
In the model, 0.499 m of the caisson were submerged while 0.06 m were above SWL. This corresponds to a prototype caisson that is submerged for 25 m and emerges for 3 m. The dry weight of the caisson per unit length was calculated as follows:

$$W_{dry} = 20.59(25 \cdot 23) + 22.55(3 \cdot 23) = 13398 kN/m \tag{4.6}$$

Subsequently, the weight of the caisson in situ was obtained :

$$W = 13398 - 10.1(25 \cdot 23) = 7590 kN/m \tag{4.7}$$

Where 10.1 kN/m$^3$ is the specific weight of sea water.

The calculation of stability factors depends on parameters that are site-specific. The analysis presented here relies on average values of parameters such as the friction coefficient $\mu$ and includes uncertainties related to the determination of the caisson's weight, which can vary based on the materials used. Therefore, the stability factors obtained from this analysis represent an average value, with the actual values potentially varying within a range. To account for the uncertainties inherent in the approach to calculating stability factors, a margin of variation of 20 % is considered around the average weight and average friction coefficient values. This range provides the limits within which the stability factors are expected to vary. The limits of variation of stability factors are depicted in grey in Figure 4.8

### Stability Factors

The stability of the caisson against sliding can be determined with Equation 4.4. $W$ is $7590$kN/m, as previously calculated. $U$ and $P$ represent the total uplift and total horizontal force, respectively, scaled up by a factor of $50^2$ according to Froude scaling rules, to obtain prototype forces per unit width in kN/m.

The stability of the caisson against overturning can be studied with Equation 4.5. $t$ is equal to 11.5 m in the prototype. $M_U$ and $M_P$ were obtained multiplying the total uplift and total horizontal force by the moment arms, which are the distance between the point of application of the force and the heel of the caisson. The points of application of the forces depend on the pressure distributions on the face of the caisson, which are time-variant. In this analysis, the points relative to the maximum pressure distributions at t = 110.5 s were used. These points correspond with the center of gravity of the pressure diagrams. The distribution of maximum total horizontal pressures on the front face was trapezoidal, as seen in Figure 4.4c. The center of gravity was determined to be 0.24 m from the heel in the model, equivalent to an arm length of 12.1 m in the prototype. The total uplift pressure exhibited a trapezoidal distribution. By disregarding pressure gradients observed at the caisson's extremities as depicted in Figure 4.4c, and assuming a linear pressure distribution between the extremes at the two bottom corners, the center of gravity was located 0.22 m from the heel in the model and 11.2 m in the prototype.

Figure 4.8 illustrates the sliding and overturning stability factor over time. It can be seen that a tsunami with the characteristics of the E20 wave, would induce both sliding and overturning instabilities in a real-scale tsunami-breakwater interaction. The duration during which the stability factor against overturning falls below the limit is shorter compared to the period during which the structure would be unstable against sliding.

The caisson, in particular, would become unstable during the period when it is overtopped by the wave. This confirms that the differences in water level on the two sides of the caisson, due to overtopping, led to the failure of the Kamaishi breakwater, as hypothesized by Arikawa et al. (2012). Patil et al. (2018) also emphasized that the development of a non-aerated overflow nappe on a caisson can generate additional destabilizing horizontal forces, further compromising the caisson's stability during overtopping events.

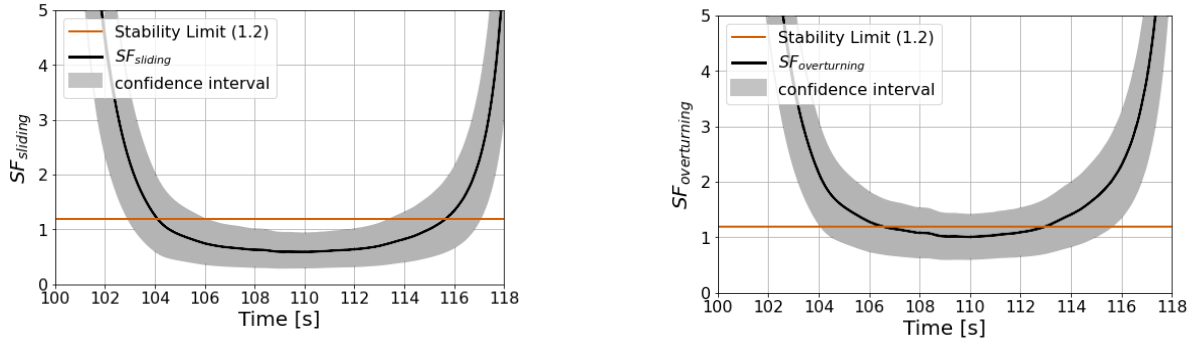


**(a)** Stability against sliding

**(b)** Stability against overturning

**Figure 4.8:** Prototype caisson stability factors against sliding and overturning

To ensure the prototype caisson stability in these conditions, using a conservative approach, the minimum values of the lower limits of the stability factors should both exceed 1.2. To achieve this, the caisson's weight should be significantly increased by 40 %, resulting in an in-situ weight of 10,900 kN per unit length. Caissons are typically constructed with a concrete structure divided into internal chambers that are filled with sand (Takahashi 1996). Reducing the volume of these chambers while increasing the amount of concrete would increase the weight of the caisson given the higher specific density of concrete. Another effective measure to increase the caisson stability would be to increase

its width, which results in increased weight and friction coefficient, raising the stability factors. These adjustments could potentially enhance the overall stability of the breakwater.

## 4.2. Numerical Results

This section presents an analysis of the most significant results obtained from the numerical model. First, the model was validated against experimental data. This validation involves comparing elevation records and pressure records on the caisson.
Subsequently, the model's accuracy and reliability was tested with further data analysis to evaluate its applicability and limitations.

### 4.2.1. Model Validation

In this section, the numerical model described in the Methodology is validated comparing surface elevations and pressures against physical results. This comparison highlights the performance of the numerical flume. Before validating the model, a comprehensive grid sensitivity analysis was conducted for both OceanWave3D and OpenFOAM to ensure grid independence and numerical solution accuracy. The performance of the numerical flume is in fact directly influenced by the grid resolution. The results of the sensitivity analysis are presented in Appendixes B and C. As illustrated in the former Appendix, the coupling between OpenFOAM and OceanWave3D was tested prior to every run with different resolutions.
The results shown in the following paraghraphs refer to the final configuration of the numerical flume, illustrated in Figures 3.4, 3.5 and explained in the Methodology. In the final configuration shown in the Figure, a base resolution of 6 cm was adopted in the OpenFOAM domain. Moreover, specific refinement zones were defined: a resolution of $\Delta x$ = 0.75 cm corresponding to 3 levels of refinement, was applied in front of the caisson, around the offshore water level, and behind it. On top of the caisson, a resolution of $\Delta x$ = 0.375 cm corresponding to 4 levels of refinement, was used. In the region of the rubble mound, a resolution of $\Delta x$ = 1.5 cm was used.

### 4.2.2. Model validation: surface elevation analysis

The model's validation was first conducted by comparing the numerical and physical surface elevation signals at Long Wave Gauges 2,4,5,6 and Short Wave Gauges 4 and 6. The validation results for the elevation time series are presented in Figure 4.9.
To assess the model's performance, Root Mean Square Errors (RMSE) were calculated to quantify the overall differences between the numerical and experimental elevations. Another useful parameter, the Normalized Root Mean Square Error (NRMSE) was also calculated as the RMSE normalized by the range of the experimental values. This quantity provides an indication of performance that is independent of the unit of the data. The NRMSE typically ranges between 0 and 1. Values around 0.1 and closer to 0 indicate that the model makes accurate predictions of the physical data. On the other hand, values closer to 1 indicate poor predictive capacity of the model.

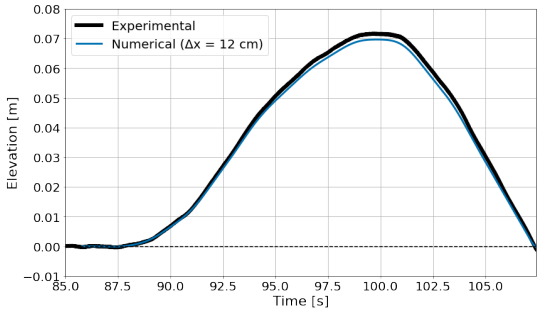


**(a)** Model validation - Elevation at LWG2 (OCW3D)

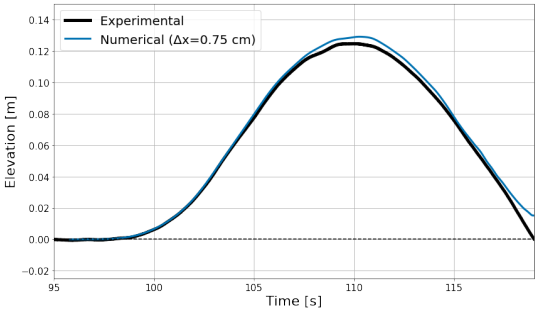


**(b)** Model validation - Elevation at LWG4

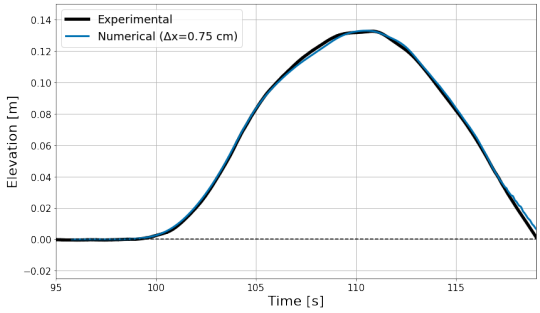


**(c)** Model validation - Elevation at LWG5

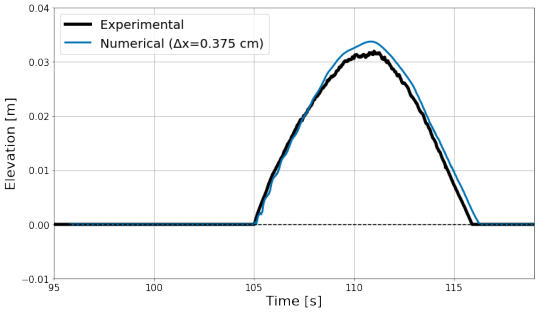


**(d)** Model validation - Elevation at SWG4

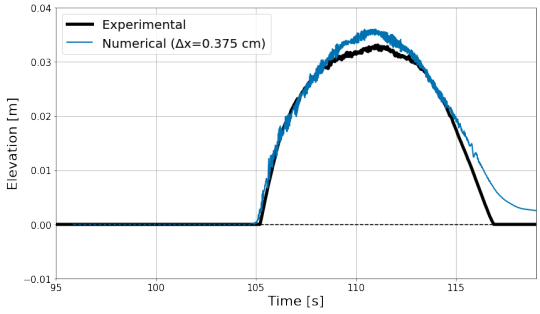


**(e)** Model validation - Elevation at SWG6

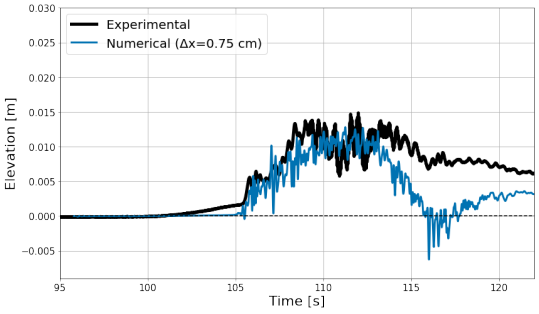


**(f)** Model validation - Elevation at LWG6

**Figure 4.9:** Model validation: comparison of experimental and numerical elevations

The model produced a good representation of the experimental elevation time series offshore of the caisson and on top of it. The Root Mean Square Error between the experimental and the numerical elevation time series was 0.010 m at LWG5, in front of the caisson, and 0.002 m on top of the caisson. The corresponding adimensional NRMSE were 0.08 and 0.07, denoting good level of predictive accuracy.

On the lee side of the caisson, at the location of LWG6, the falling of the overflow jet induced high turbulence and recirculation of water, resulting in a biphasic flow characterized by the presence of air particles within the water flow. Patil et al. (2018) observed that the complex hydrodynamic behaviour of the overflow jet falling on the lee side of a caisson cannot be modelled as a two-dimensional process. They also found out that the interFoam solver lacks the correct representation of the aeration mechanism that takes place in these cases, and fail to capture small bubbles that are entrained and supplied back into the air cavity below the overflow jet.
This research also identified a significant constraint affecting numerical data analysis on the lee side. Specifically, it highlighted that the numerical model fails to reproduce experimental findings in this region with high accuracy. Even with increased resolution on the lee side, the representation of elevation data at LWG6 did not improve, as evidenced in Appendix C. Refining the mesh introduced additional oscillations in both the elevation and pressure time series.

Observations indicate that oscillations, stemming from the biphasic nature of the fluid, were visibly present in the physical elevation records at LWG6 as well, as depicted in the Figure. Additionally, albeit to a lesser extent, oscillations in surface elevations were also observed on top of the caisson near the lee side, which are similarly captured by the numerical model at SWG6. The NRMSE at LWG6 is 0.3, suggesting non negligible differences between experimental and numerical elevations.

### 4.2.3. Model validation: Pressure analysis

Following the comparison of the physical and numerical surface elevation time series, the model validation proceeded by comparing the numerical and experimental pressure time series.
Figure 4.10 shows the results of the validation for the pressure sensors located in front of the caisson, on top of it and on its lee side. While the experimental pressure sensors initially exhibited high-frequency noise generating from the instrument, addressed with filtering as explained in Section 3.1.5, the numerical pressure signals did not exhibit such oscillations in front of the caisson. Therefore, they could be directly compared with the experimental filtered data.
A resolution of $\Delta x$ = 0.75 cm was capable of capturing the pressure time series in front of the caisson with an average RMSE of 0.033 kPa and an average NRMSE of 0.025, indicating a very good correspondence between the experimental and numerical pressure records. In the numerical model, the peak pressures were slightly underestimated, by on average 1.17 %. On top of the caisson, the model could reproduce the physical pressure records with a finer resolution with a NRMSE of 0.03 and an overestimation of 0.46 % of the peak pressure.

The Figure also illustrates the comparison between experimental and numerical pressure records on the lee side of the caisson with the employed resolution of $\Delta x$ = 0.75 cm. As discussed earlier, the biphasic nature of the fluid in this region resulted in numerous oscillations in the records. These oscillations were particularly pronounced in the sensor closer to the water surface, PT07, located near the point where the overflow nappe cascaded onto the rear of the caisson, generating eddies. Patil (2019) also noted discrepancies in OpenFOAM simulations of free nappe falling behind a caisson, where cycles of air entrainment into and out of the cavity do not accurately reflect the real physical behavior of the nappe. This inconsistency resulted in less reliable estimates, particularly close to the water surface, which were further compromised when using a two-dimensional model.
For ease of interpretation, the numerical pressure records in this region were filtered using a low-pass filter to remove high-frequency oscillations caused by the presence of air bubbles. The cutoff frequency of the filter was set to 0.3 Hz, equal to that used for filtering the experimental pressure records to maintain data integrity. The unfiltered numerical signals can be viewed in Appendix C for reference. The average NRMSE of the pressures on the lee side of the caisson was 0.34.

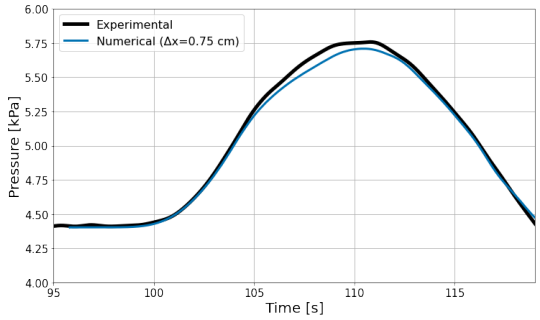


**(a)** Model validation - Pressure at PT3

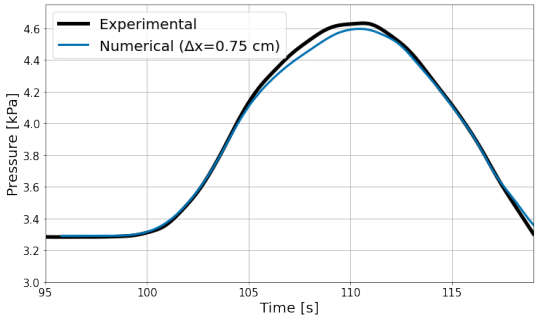


**(b)** Model validation - Pressure at PT01

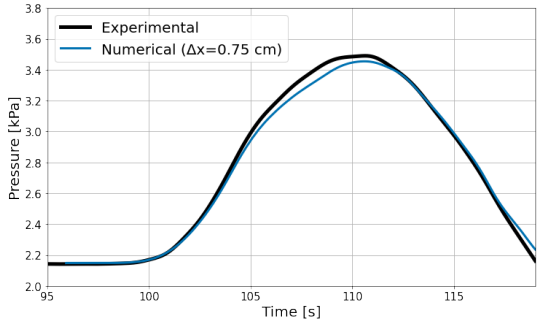


**(c)** Model validation - Pressure at PT02

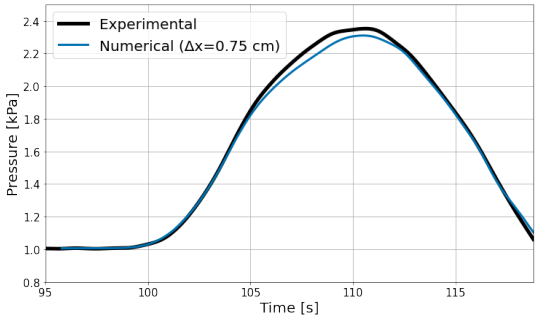


**(d)** Model validation - Pressure at PT03

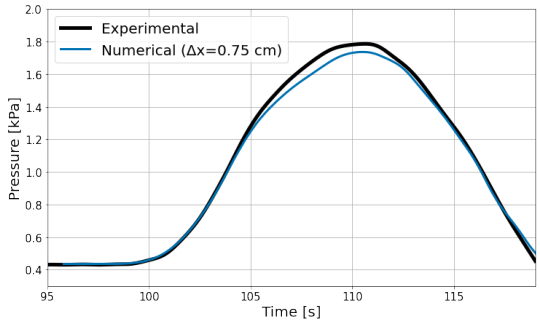


**(e)** Model validation - Pressure at PT04

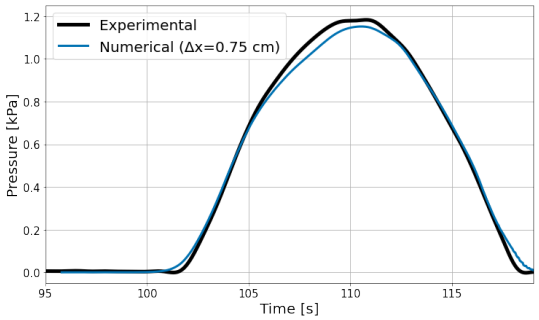


**(f)** Model validation - Pressure at PT05

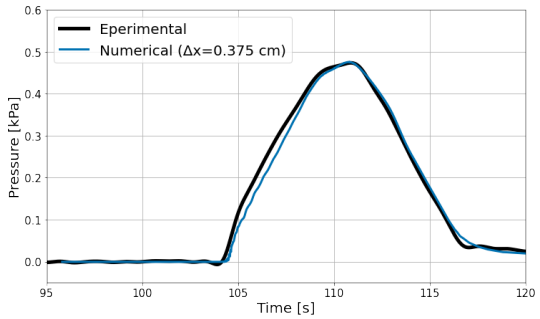


**(g)** Model validation - Pressure at PT08

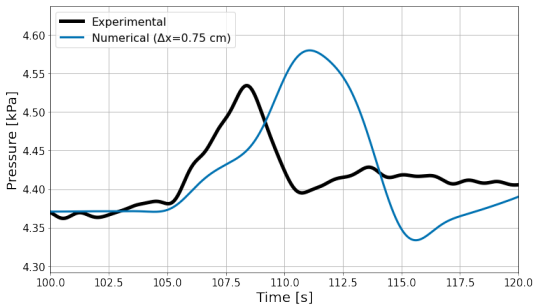


**(h)** Model validation - Pressure at PT4

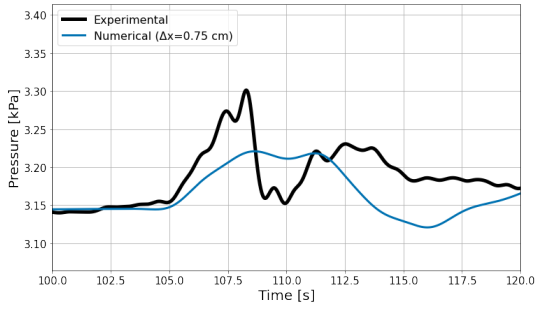


**(i)** Model validation - Pressure at PT06

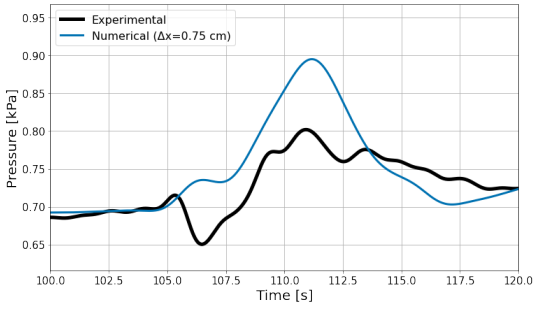


**(j)** Model validation - Pressure at PT07

**Figure 4.10:** Model validation: comparison of experimental and numerical pressure records

### Porosity parameters and bottom face of the caisson

Figure 4.11 shows the validation of the pressure records located on the bottom face of the caisson at the interface with the rubble mound. A resolution of $\Delta x$ = 1.5 cm was used in the region of the rubble mound since finer resolutions did not produce improved results but only increased the computational time. Three values of the resistance parameters $\alpha$ and $\beta$ were tested with porosity parameters of the rubble mound layers imposed as explained in Section 3.2.7. Appendix C shows the comparison of the pressure time series changing the resistance coefficients.
The values recommended by Losada et al. (2008), $\alpha = 200$ and $\beta = 0.8$, applied to every layer of the foundation, produced numerical results closest to the experimental ones, with an average RMSE and NRMSE of 0.12 kPa and 0.20.

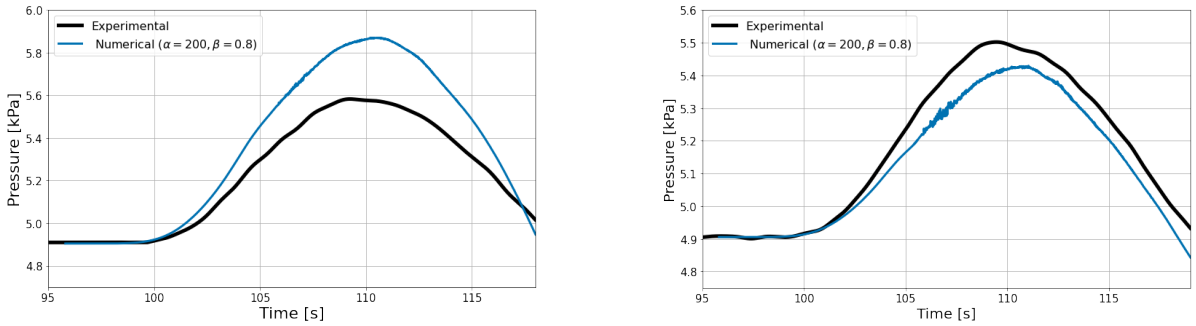


**(a)** Model validation - Pressure at PT1

**(b)** Model validation - Pressure at PT2

**Figure 4.11:** Validation of pressure records on the bottom.

It can be observed that the model overestimated the peak pressure at PT1 by 0.29 kPa and underestimated it at PT2 by 0.07 kPa, corresponding to 4.94 % and 1.32 % of the peak pressures, respectively.

Mata and Van Gent (2023) conducted research on modeling wave overtopping discharges on rubble mound breakwaters using the same approach of coupling OpenFOAM and OceanWave3D as used in this thesis. They concluded that OpenFOAM struggles with accurately solving the combination of porous media and detailed turbulence closure models, such as the stabilized $k-\omega$ model used in this research. This inadequacy significantly affects wave overtopping and the flow through the permeable structure. In this research, the same approach was employed with the porous solver and the stabilized $k-\omega$ closure model. This produced generally good results regarding wave overtopping on the caisson, with only minor overestimation of the peak overtopping elevation and the peak overtopping pressure. However, the wave propagation through the porous layers and the pressure records in this region differed from the physical observations. It must also be acknowledged that in this study, the oscillatory part of the Darcy-Forchheimer equation ( Equation 3.23) inside the porous media was limited by setting a very high value of the $KC$ number. However, the impact of this parameter on the modeling of flow through porous media is not yet fully understood, and its estimation is not trivial, as explained in Section 3.2.7. This could influence wave propagation in the rubble mound, as observed in the figure. Further aspects that could influence the model accuracy in this region are detailed in the Discussion.

## 4.2.4. Numerical pressure distribution

The numerical pressure distributions on the caisson were compared with experimental ones at specific times to evaluate the model's predictive accuracy. The numerical pressure distributions, shown in blue, were plotted based on the pressure values predicted by the model at each cell located at the interface with the caisson's faces in the numerical flume.

The pressure distribution at $t$ = 110.5 s was first examined. At this moment, the experimental data analysis showed pressure peaks on the front face of the caisson. This instance coincides with the peak horizontal total force and the lowest stability factor values against sliding and overturning. Therefore,

it is crucial for the numerical model to replicate the actual pressure distribution to enable a reliable stability analysis. The pressure distributions were also compared at $t$ = 106 s, after overtopping started, and at $t$ = 117 s, when overtopping was completely over. At $t$ = 106 s and $t$ = 110.5 s, a sketch of the numerical elevations on top of the caisson is provided, obtained by wave gauges located as in the physical flume, and additional gauges placed at the edges of the caisson.

One notable observation is the absence of abrupt pressure gradients at the bottom of the caisson. This directly follows from the pressure distribution in the front and back of the caisson. In the deepest part of the caisson, small pressure gradients can be observed on both the seaward and landward faces. These result from the caisson being partially embedded in the rubble mound. The porous rubble mound exerts a drag force on the flow, as described by Equation 3.23, which caused the formation of these pressure gradients. Conversely, the pressure distribution on the bottom side of the caisson was trapezoidal, with no significant pressure gradients. The pressure values at the corners of the caisson in the model were identical across the two adjacent faces of each corner.

During overtopping, the model recorded negative pressure values in the upper part of the landward face and on the top face close to the lee side. This suggests that the model struggles to record accurate pressure values when the fluid is highly biphasic and contaminated with air bubbles and in the vicinity of this region. The formation of an air cavity below the nappe and the presence of air bubbles in the overflow region complicate the accurate modeling of pressures in this area. The negative pressures were set to 0 in Figures 4.12 to 4.14.
Additionally, close to the seaward edge of the caisson, at the top face, some oscillations in the numerical pressures were observed. The sketched elevations during overtopping, in contrast with the experimental ones shown in Figures 4.4b and 4.4c , display a different evolution of the broad-crested weir. While experimental gauges indicate that the water level slightly increased towards the lee edge of the caisson during overtopping, this was not observed in the numerical model. Instead, a contraction of the overtopping flow on top of the caisson is noted.

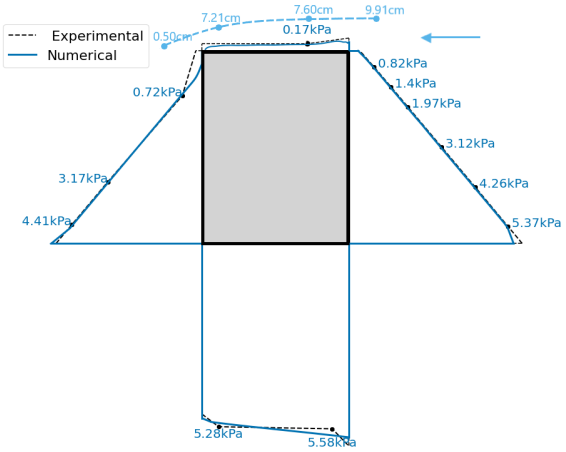


**Figure 4.12:** Experimental and numerical pressure distributions at $t$ = 106 s

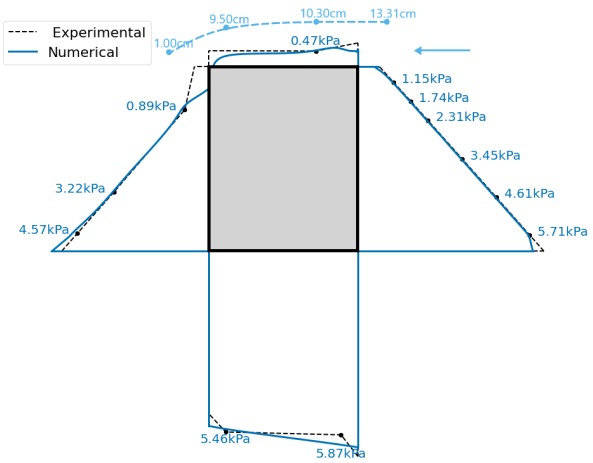


**Figure 4.13:** Experimental and numerical pressure distributions at $t$ = 110.5 s

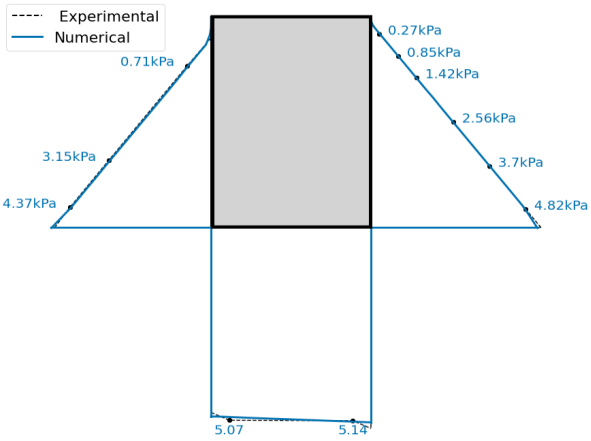


**Figure 4.14:** Experimental and numerical pressure distributions at $t$ = 117 s

**Figure 4.15:** Comparison of experimental vs numerical results at different times.

Comparing the numerical values in Figure 4.15 with those in Figures 4.4b to 4.4d indicates that the pressure values at the locations of the physical probes were overall well predicted by the numerical model at the three analyzed times. At the instant of maximum pressure on the front face ($t$ = 110.5 s), the model's predicted pressures on the front face of the caisson were underestimated by a maximum of 2%, while the pressure values on the back face were overestimated by up to 10% near the still water level. The overestimation on the back face is also due to the slight delay in the increase of numerical pressure records on the lee side. For instance, looking at the pressure record at PT4 in Figure 4.10, it is evident that the peak in numerical pressures is slightly shifted in time compared to the peak in experimental pressures. At the bottom of the caisson, numerical pressures were overestimated by 5% near the seaward edge and underestimated by 1% closer to the landward edge of the caisson. The pressure value recorded on top of the caisson at the location of the physical probe is almost identical to the physical measurement, despite the slight difference in overtopping surface elevation.

The largest discrepancy between experimental and numerical values occurred in the critical region of biphasic fluid on the lee side of the caisson. However, the numerical model's predicted linear pressure distribution on this face supports the assumption of hydrostatic pressure distribution made in the experimental data analysis section. This also confirms the negligible contribution of hydrodynamic and impulsive pressures caused by the overtopping jet.

### 4.2.5. Numerical forces and Stability analysis

The model was tested to calculate the forces exerted by the wave on the caisson and subsequently perform a numerical stability analysis. Ensuring the caisson's stability against sliding and overturning is crucial when designing composite breakwaters for coastal protection. Therefore, it is essential that a numerical model developed to simulate the physical response of a breakwater impacted by a tsunami can be used to accurately study the structure's stability.
In OpenFOAM, the forces were calculated using the "forces" function, which integrates pressure over the areas of each grid cell to produce a time series of the total horizontal and vertical forces acting on the caisson. This method can yield more accurate results compared to physical experiments, which rely on a limited number of known pressure values and assumed distributions between probes. The numerical forces obtained from OpenFOAM were compared with those derived from the experimental time series, as explained in Section 4.1.3. Figures 4.16 and 4.19 show the superimposition of experimental and numerical horizontal and uplift forces. While the horizontal force closely matches the experimental results, the numerical uplift force exhibits different behavior and is generally higher than the experimental force during instances of overtopping. This discrepancy is likely due to the assumption of a constant pressure distribution on top of the caisson, inferred from a single pressure sensor, for the calculation of the experimental overtopping force. In contrast, the numerical results indicate that the pressure acting on the top face decreased from PT08 towards the lee side of the caisson, consistent with the reducing modelled water level .

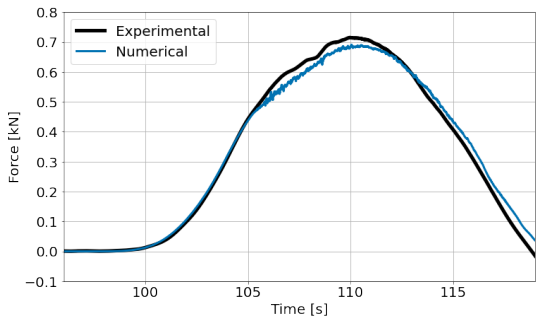


**Figure 4.16:** Experimental and numerical horizotnal force

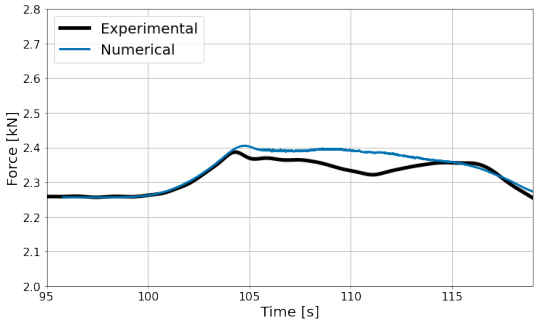


**Figure 4.17:** Experimental and numerical uplift force

Using Equations 4.4 and 4.5, the stability factors against sliding and overturning of the caisson were calculated from the numerically obtained forces and compared with those calculated from the physical experiment, as illustrated in Figures 4.18 and 4.19. In the plots, the average physical stability factors described in Section 4.1.4 are plotted in black, while the grey area identifies the physical confidence region, as preciously described. The figure demonstrates that the model can reliably perform a stability analysis, with only minor differences when compared to the experimental sliding and overturning stability factors.

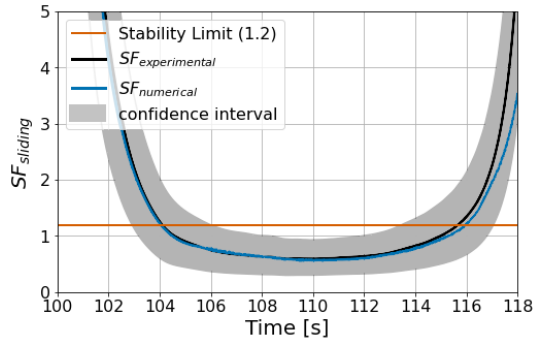


**Figure 4.18:** Experimental and numerical sliding stability factors

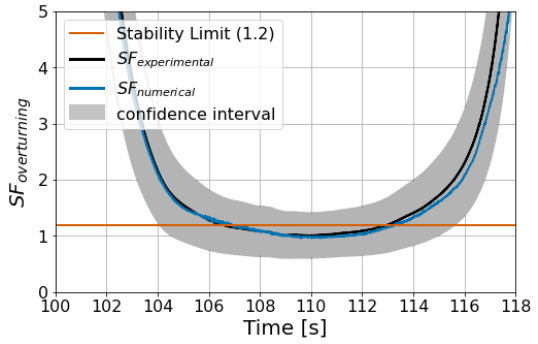


**Figure 4.19:** Experimental and numerical overturning stability factors

# 5

# Discussion

## 5.1. Tsunami impact on a composite breakwater

Through the analysis of experimental data and numerical simulations, the hydrodynamic interaction between tsunami waves and composite breakwaters was studied to improve the understanding of these structures' capability to withstand tsunami impacts, thereby aiding in the protection of critical coastal areas. The research focused on the E20 wave, an elevated wave with a model period of 20 seconds, corresponding to a prototype period of 140 seconds.

This study highlighted that tsunamis primarily exert hydrostatic pressures on the caisson's front face of a composite breakwater. When impacted by a tsunami, the front face experienced extremely low dynamic pressures, up to only 3.72 % of the total pressure. In particular, the pressure increase observed on the front face mirrors the elevation of the wave impacting the vertical wall. This contrasts with findings from Mizutani (2015), who observed three peaks in pressures when a tsunami hit a sloped wall, modelling the tsunami wave as a bore-type transient wave. Correctly modelling tsunami waves as trough led N-waves or elevated E-waves, as suggested by Madsen et al. (2008) avoids conflicting findings.
On the lee side of the breakwater, despite measurement challenges due to the biphasic nature of the fluid from the overtopping jet, the pressure distribution remained primarily hydrostatic. In fact, the pressure values at the probe locations did not significantly differ from stillwater hydrostatic pressures, suggesting only a minor contribution from dynamic components. This study showed that hydrodynamic pressures exerted by tsunami waves are non negligible only on the top face of the caisson when overtopping occurs.

These findings confirm some conclusions from previous studies. In fact, Foster et al. (2017) stated that for longer period waves, like tsunamis, there is negligible impulsive component in the forces experienced by a rectangular structure, and the pressure distributions on the structure are hydrostatic.
On the lee side of the caisson, where the overtopping jet generates high recirculation of water and turbulent motions, the duration of the pressure peaks captured by both experimental and numerical probes ( PT4, PT06, and PT07 in Figure 4.10) suggest that the increases in pressure are due to lee side elevation changes produced by overtopping, and wave propagation through the rubble mound, rather than from impulsive impact of the overtopping jet.
Findings from Foster et al. (2017), McGover et al. (2018, 2019, 2023) indicate that long tsunami-like waves shoaling over a breakwater's rubble mound do not lead to wave breaking. Consequently, impulsive forces are negligible and do not contribute to structural damage. This study also confirmed the absence of noticeable impulsive force peaks when a tsunami hits and overtops a composite breakwater, but rather a quasi-steady flow caused by the long period of the waves, as observed by Wüthrich et al. (2018) for tsunami-like waves hitting a structure. However, this observation might not hold true in the case of more impulsive unsteady flows.

Aniel-Quiroga et al. (2019) identified three distinct pressure peaks on the lee side of a breakwater's crown wall when hit by a tsunami wave, attributed primarily to the wave impact, down-rushing water, and transmitted waves from the overtopping jet. However, this study did not observe such distinct peaks in case of composite breakwaters overtopped by a tsunami. Instead, pressure records on the lee side of the caisson exhibited an unstable increase with numerous oscillations. These fluctuations were attributed to the presence of air bubbles generated by the overtopping jet, which compromised the accuracy of pressure measurements.

## 5.2. Performance and applicability of the model

To further study the impact of tsunami waves on composite breakwater, a two-dimensional numerical model was developed in this research. The model was validated against experimental results using E20 wave data. The validation of the model demonstrated its accuracy in representing physical time series for both the elevations offshore of the caisson and the pressure records on the seaward face of the caisson. Additionally, the model showed high accuracy in representing the physical results on the top face of the caisson, with both physical elevations and pressures accurately captured.

However, on the lee side of the caisson, the numerical model exhibited limitations in producing accurate elevation and pressure time series, as previously detailed.
The model also showed deviations of up to 4.94 % when compared to experimental pressure measurements on the bottom face of the caisson. This discrepancy is attributed to the challenges in accurately determining the parameters that govern flow through porous media, as discussed in Section 3.2.7. Moreover, OpenFOAM is highly sensitive to parameters such as stone dimensions and the resulting porosity of the porous layers. The absence of detailed information on the grain size distribution of the different rubble mound layers in this research, therefore, plays a significant role. Consequently, parameters such as the median diameter and the porosity of the layers implemented in the model may differ from the actual physical ones in the experiment. Furthermore, inaccuracies highlighted by Mata and Van Gent (2023) in OpenFOAM regarding the simultaneous presence of porous media and complex closure models, such as the one developed by Larsen and Fuhrman (2018) and employed in this study, contribute to these discrepancies, resulting in overestimation of turbulence in the porous media. In particular, Jensen et al. (2014) highlighted that the resistance coefficients used by the porous solver already account for the turbulence effects within the porous media. Consequently, introducing a closure model results in turbulence being solved twice by OpenFOAM, compromising the accuracy of flow modelling in porous media. The overestimation was however limited by setting a high value of the $KC$ number.

Despite these limitations, the model proved to be accurate for studying the pressure distribution on the caisson at different instances of tsunami impact. The pressure values at the locations of the physical probes showed a high degree of similarity with the recorded values, with non-negligible discrepancies only on the bottom and lee side, where pressures can be overestimated or underestimated by up to 10 % of their actual value, on the lee side close to the still water level. The model also addresses the physical limitation of using only a limited number of pressure sensors in physical breakwater models, providing a more detailed distribution of pressures that would otherwise only be assumed.
Moreover, the model could also be used for capturing the forces exerted by the wave on the caisson, potentially yielding more reliable time series for both horizontal and vertical forces, given the direct integration of pressures at each grid cell. In contrast, experimentally calculated forces rely on assumed pressure distributions across the caisson face and are limited to a few known pressure values only.
The stability analysis performed using the numerical model produced similar results to those obtained from the physical stability analysis.

## 5.3. Computational efficiency of the model

The model developed in this study is based on the coupling of the two CFD softwares OpenFOAM and OceanWave3D. While OceanWave3D is a very fast potential flow solver, OpenFOAM is definitely more computationally expensive. The OpenFOAM domain of the final model configuration consists of a 2D

flume composed of 169,149 cells. The duration of the simulation in OpenFOAM was selected as 30 seconds. The computational time is approximately 96 hours when the simulation is run in parallel with 8 threads (Intel Core i7-7700HQ 2.80 GHz) and 16 GB of RAM.
Although being computationally expensive, the model's performance is overall accurate and therefore the computational time is considered acceptable. The use of a supercomputer with higher number of nodes is suggested to fasten the simulation speed.

# 6

# Conclusions and Outlook

## 6.1. Conclusions

The catastrophic impacts of past tsunamis and the failures of coastal protection structures, such as the world-record Kamaishi breakwater, underscore the crucial need to advance our understanding on the interaction between tsunamis and coastal structures. Furthermore, many coastal protection structures worldwide are not specifically designed to endure tsunami forces, significantly increasing the risk of failure in the event of a tsunami.
This study aimed to analyze the results of experiments where scaled tsunami waves were generated in a 2D flume and impacted a composite breakwater model inspired by the Kamaishi breakwater. A numerical model was also developed as part of this research to explore the feasibility of replicating these experiments and to further extend the findings beyond the constraints of physical modelling.

In this section, an answer to the research question and sub-questions defined in the Introduction is given. Furthermore, the major limitations of this study and recommendations for future research are highlighted.

1. **What are the key hydrodynamic interactions, pressure distributions and forces exerted when a tsunami wave interacts with a composite breakwater structure?**

This study reveals that elevated tsunami waves impact on composite breakwaters primarily causes an increase in hydrostatic pressure on the caisson's faces. Neglecting the hydrodynamic contribution of pressures would result in a maximum estimated error of 4 % on the front and back face. On the other hand, the hydrodynamic contribution should not be neglected on the top face of the caisson, if overtopping occurs. The pressure increase on the front face of the caisson is associated with the rise in surface elevations and quasi-steady flow in this region. As the wave propagates through the porous rubble mound, the pressure exerted on the bottom face of the caisson increases. Given the very long wavelength and extended duration of typical tsunamis, they can easily overtop the caissons of composite breakwaters. The overtopping process is associated to higher and non negligible hydrodynamic contributions on the top face of the caisson, up to 35 % of the total pressure in this study. The fall of the overtopping jet on the lee side of the caisson produces flow recirculation and turbulence. This causes the flow to become biphasic with air bubbles entrained in it. As a consequence, the pressure evolution in this area showed many small amplitude fluctuations. The pressure distributions on the back face of the caisson were nonetheless observed to be primarily hydrostatic.
In the case of tsunami waves, and very long waves in general, shoaling over rubble mounds does not typically result in wave breaking, thereby avoiding the production of impulsive forces (Foster et al. 2017, Mc Govern et al. 2018, 2019) which were in fact not observed in this study. The analysis of the horizontal force on the caisson reveals a shape that closely matches the elevation and pressure time series evolution in front of it, slightly reduced by the force acting in opposite direction on the lee side. The peak of the horizontal force, 0.71 kN in this study, occurs at the moment of the greatest pressure and

elevation difference between the front and back sides of the caisson, which is the most critical moment for caisson stability. The uplift force on the caisson's bottom face also initially mirrors the wave shape but is attenuated by the force exerted by the overtopping flow in the opposite direction.

2. **How effectively does a numerical model simulate the generation, propagation, and impact of a tsunami wave interacting with a composite breakwater? What additional insights does it provide compared to experimental results, and what are its associated limitations?**

The model developed in this research can reproduce the generation, propagation and impact of the simulated E-wave with a composite breakwater with an overall good accuracy. A thorough sensitivity analysis was carried out to identify the grid resolution capable of reproducing the most accurate elevation and pressure time series in the numerical model, subsequently utilized for the validation of the model against the experimental data. The validation of the model demonstrates a strong capability to reproduce the experimental pressures and elevation time series on the front face and top face of the caisson, with low Normalized Root Mean square Error values between the experimental and numerical data (NRMSE < 0.1). On the other hand, the model exhibited a more limited accuracy in reproducing pressure time series on the back and bottom faces of the caisson, with higher NRMSE values. These limitations stemmed from the inherent complexity of the simulated processes. Firstly, the complex physics of the overtopping process, along with the turbulence generated by the jet falling on the lee side, was not solved by the model with sufficient accuracy. The primary cause of this discrepancy is the presence of air bubbles and biphasic flow on the lee side, which resulted in pressure readings exhibiting numerous oscillations, complicating data analysis. Even the increase in grid resolution in this region did not result in improved pressure estimates, as evidenced in Appendix C. Furthermore, the two-dimensional nature of the model cannot accurately solve the high three-dimensionality of the overtopping phenomenon (Patil et al. 2018). Deviations between the numerical and experimental pressure time series are particularly evident closer to the water surface in proximity of the overtopping jet.
Additionally, on the bottom side of the caisson, at the locations of the physical probes, the model was capable of reproducing the shape of the pressure records, but the numerical peak values slightly deviated from those recorded by the physical probes. This limitation arose from several factors that affect the model's ability to accurately reproduce the pressure records in this region. Among these causes are the observed difficulties in accurately estimating turbulence when incorporating porous media combined with complex closure models in OpenFOAM. This approach results in turbulence being solved twice in the porous regions, leading to its overestimation. Furthermore, the complexity and not fully understood estimation of parameters in the Darcy-Forchheimer equation, along with the high sensitivity of OpenFOAM to parameters such as the dimensions of the stones in the porous layers, also play a significant role.

Despite the observed limitations, the model developed in this research was capable of reproducing the pressure distributions on the caisson at specific time instants with only minor differences from the experimental pressure values. Furthermore, the model addressed the constraints imposed by the physical limitations of using only a few pressure probes on the caisson. While the physical experiment relied on an assumed pressure distribution among these probes, the numerical model provided a pressure distribution with pressure records at every grid cell. As OpenFOAM directly integrates the pressure values at every cell, it overcomes the issues arising from few known pressure values in the physical model when calculating horizontal and uplift forces. The forces obtained from the numerical model were also used to perform a stability analysis of the caisson, yielding results similar to those of the physical one. With the research focusing on the entire breakwater response to a tsunami, using a 2D model is preferable for saving computational time, while still obtaining precise results with only minor over- or underestimation of pressures and forces.
Given the high accuracy in predicting overall pressure distributions, the model represents a suitable starting point for future studies on tsunami-structure interaction. This approach offers the invaluable advantage of avoiding the material costs associated with conducting physical experiments, albeit having a non negligible computational cost.

3. **What are the critical aspects of caisson stability during a tsunami? How well does the numerical model perform in studying the stability of the caisson?**

In this study, an analysis was conducted to evaluate caisson stability against sliding and overturning under conditions simulating a real-scale tsunami resembling the E-20 wave. The analysis revealed that in the prototype composite breakwater, the caisson would be unstable against both sliding and overturning when subjected to a tsunami characterized by the real-scale E20 wave with a prototype period of 140 seconds. In particular, the stability factor against sliding of the caisson would be even lower than that against overturning and fall below the allowable limit throughout the entire overtopping process duration. At 110.5 seconds, corresponding to the instant of maximum pressures on the front face, the caisson experienced its highest horizontal force and a reduced stability factor against both sliding and overturning. This time also marked the peak difference in surface elevation between the front and back sides of the caisson. Furthermore, the non-aerated overtopping nappe introduced additional destabilizing horizontal forces on the caisson, further compromising its stability against sliding.
The most critical moments for caisson stability were observed during overtopping, particularly at the instant of maximum pressure differences between the front and back faces, which corresponded with the maximum horizontal force. Increasing the caisson's width can be an effective measure to enhance its weight and friction coefficient, thereby improving its stability against tsunamis.
The model developed in this thesis proved to be accurate for assessing the caisson stability, yielding stability factor time series closely aligned with experimental results. The numerical stability analysis could be even more accurate than the experimental one due to the direct integration of pressures on surfaces for forces calculation, which avoids assumptions inherent in experimental analyses. Therefore, the model is suitable and adaptable for future studies analyzing the stability of composite breakwaters against tsunami waves.

## 6.2. Limitations

One of the most noteworthy limitations arises on the back side of the caisson. There, the highly biphasic nature of the fluid is not correctly captured by OpenFOAM, which measures oscillating and inaccurate pressures as a consequence. This limitation is also linked to the two-dimensionality of the model. While a 2D model offers significant computational advantages, it introduces some inaccuracies when simulating three-dimensional phenomena such as the overtopping of a caisson. This limitation was also previously highlighted by Patil et al. (2018).
Another limitation arises from uncertainties in the physical experimental setup. For instance, detailed information regarding the rock size distribution of the porous rubble mound used in the experiment is lacking, which restricts accurate estimation of parameters such as median diameters and porosity for implementation in the model. These uncertainties consequently impact the model's results in the porous region. Additionally, the complexity linked to estimating parameters such as the KC number in the Darcy-Forchheimer equation affects the modeled flow propagation through the porous media and consequently influences results in the bottom area of the caisson.
Other limitations related to physical modeling, such as the constrained number of pressure probes and wave gauges available to measure parameters like pressures and surface elevations in the flume, can be overcome through numerical modeling. In fact, the numerical model in this study enables measurements at numerous locations across the domain with no significant increase in computational time.

## 6.3. Recommendations and outlook for future studies

For future studies in tsunami engineering and the modelling of tsunami interactions with coastal structures, the results and model developed in this research serve as a valuable starting point adaptable to specific scenarios. The analysis in this thesis suggests that studying the pressures exerted by the tsunami and the resulting forces on the structure can be done by considering only the hydrostatic contribution, while neglecting the hydrodynamic component, resulting in a minor underestimation of up to 4 % of pressures. However, this simplified approach does not apply to the top face of composite breakwaters' caissons in case of overtopping events, where a significantly higher and non-negligible hydrodynamic pressure contribution is observed.

The model developed in this research can be used and adapted for future studies involving other tsunami scenarios, to investigate their interaction with composite breakwaters. The model demonstrates strong capabilities in reproducing horizontal and uplift forces on the caisson when compared to experimental results, and can therefore be used to assess caisson stability. The two-dimensional nature of the model offers a clear advantage in terms of computational efficiency, particularly beneficial when overtopping phenomena are not present. An important recommendation is to further validate the proposed model using other tsunami waves experiments, including simulations of N waves. This expanded validation process would enhance confidence in the model's applicability across diverse scenarios, potentially including other coastal protection structures. Moreover, when modelling the interaction of a tsunami with a rubble mound, it is important to thoroughly investigate the composition and grain size distribution of the porous layers. This ensures accurate implementation of porous parameters in the numerical model, minimizing discrepancies in modelled flow through the porous media. Finally, when studying the stability of a breakwater impacted by a tsunami, the analysis should not be limited to the predominant failure mechanisms associated with caissons in composite breakwaters, such as sliding and overturning. Additional failure mechanisms should be investigated to enable a more comprehensive assessment.

### 6.3.1. Recommended approach for implementation of a numerical model to study tsunami-structure interaction

As a general approach, the following procedure is recommended for numerical modeling of tsunami impact with coastal structures:

1. Set up the OceanWave3D model standalone:
    - Implement the paddle signal velocity at the inlet boundary.
    - Perform a temporal and spatial grid sensitivity analyses to ensure correct representation of the surface elevation time series at the inlet.
    - Implement relaxation zones at the outlet of the OceanWave3D domain to avoid wave reflection.
2. Set up the OpenFOAM model standalone:
    - Set up the base mesh and refinement zones in the areas of interest.
    - Configure the structure by removing the impermeable zones and implementing the porous layers.
3. Set up the coupled model:
    - Implement a relaxation zone at the inlet of the OpenFOAM domain, to transfer the hydraulic conditions from the OceanWave3D domain.
    - Perform spatial grid sensitivity analysis to optimize the representation of physical processes while minimizing computational costs.

# References


Alison, R., Joshua, M., P., Antonios, Wilkinson, S., and Rossetto, T. (2015). “Implications of the 2011 Great East Japan Tsunami on sea defence design”. In: *International Journal of Disaster Risk Reduction* 14, pp. 332–346. ISSN: 2212-4209. DOI: 10.1016/j.ijdrr.2015.08.009. URL: https://www.sciencedirect.com/science/article/pii/S2212420915300534.

Aniel-Quiroga, I., Vidal, C., Lara, J., and González, M. (2019). “Pressures on a rubble-mound breakwater crown-wall for tsunami impact”. In: *Coastal Engineering* 152, p. 103522. DOI: 10.1016/j.coastaleng.2019.103522.

Aniel-Quiroga, I., Vidal, C., Lara, J.L., and Gonzalez, M. (2018). “Stability of rubble-mound breakwaters under tsunami first impact and overflow based on laboratory experiments”. In: *Coastal Engineering* 135.

Arikawa, T., Sato, M., Shimosako, K., Hasegawa, I., Yeom, G.S., and Tomita, T. (2012). “Failure mechanism of Kamaishi breakwater due to the Great East Japan Eqarthquake Tsunami”. In: *Coastal Engineering Proceedings* 1. DOI: 10.9753/icce.v33.structures.16.

Barendse, L. (2021). “Hydrodynamic modelling of wave overtopping over a block-covered dike”. MA thesis. University of Twente.

Berberović, E., Van Hinsberg, N., Jakirlić, S., Roisman, I., and Tropea, C. (2009). “Drop impact onto a liquid layer of finite thickness: Dynamics of the cavity evolution”. In: *Physical review. E* 79, p. 036306. DOI: 10.1103/PhysRevE.79.036306.

CIRIA CUR, CETMED (2007). *The Rock Manual - The use of rock in hydraulic engineering*. C683, CIRIA, London.

Engsig-Karup, A., Bingham, H., and Lindberg, O. (2009). “An efficient flexible-order model for 3D nonlinear water waves”. In: *Journal of Computational Physics* 228, pp. 2100–2118. DOI: 10.1016/j.jcp.2008.11.028.

Esteban, M., Onuki, M., Ikeda, I., and Akiyama, T. (2015a). “Reconstruction following the 2011 Tohoku earthquake tsunami: Case study of Otsuchi Town in Iwate prefecture, Japan”. In: *Handbook of Coastal Disaster Mitigation for Engineers and Planners*, pp. 615–630. DOI: 10.1016/B978-0-12-801060-0.00029-0.

Esteban, M., Thao, N., Hiroshi, T., Ravindra, J., Takahito, M., and Tomoya, S. (2015b). “Stability of breakwaters against Tsunami attack”. In: *Handbook of Coastal Disaster Mitigation for Engineers and Planners*, pp. 293–323. DOI: 10.1016/B978-0-12-801060-0.00015-0.

Esteban, M., Thao, N., Takagi, H, and Shibayama, T. (2008). “Analysis of rubble mound foundation failure of a caisson breakwater subjected to tsunami attack”. In: *Proceedings of the International Offshore and Polar Engineering Conference*.

Foster, A.S.J., Rossetto, T., and Allsop, W. (2017). “An experimentally validated approach for evaluating tsunami inundation forces on rectangular buildings”. In: *Coastal Engineering* 128, pp. 44–57. ISSN: 0378-3839. DOI: 10.1016/j.coastaleng.2017.07.006. URL: https://www.sciencedirect.com/science/article/pii/S0378383916303544.

Goodarzi, E, Farhoudi, J., and Shokri, N. (2012). “Flow Characteristics of Rectangular Broad-Creestevand Weirs with Sloped Upstream Face”. In: *Journal of Hydrology and Hydromechanics* 60. DOI: 10.2478/v10098-012-0008-1.

Guler, H., Baykal, C., Arikawa, T., and Yalciner, A. (2018). “Numerical assessment of tsunami attack on a rubble mound breakwater using OpenFOAM ®”. In: *Applied Ocean Research* 72, pp. 76–91. DOI: 10.1016/j.apor.2018.01.005.

Gusiakov, V. (2009). “Tsunami history: recorded.” In: *The Sea* 15.

Hanzawa, M. and Matsumoto, A. (2015). “Stability and Disaster Mitigation Effect of Wave-Dissipating Concrete Blocks of Detached Breakwaters Against Tsunami Waves”. In: *Handbook of Coastal Disaster Mitigation for Engineers and Planners*, pp. 325–347. DOI: 10.1016/B978-0-12-801060-0.00016-2.

Heller, V. (2011). “Scale effects in physical hydraulic engineering models.” In: *Journal of Hydraulic Research* 49(3), pp. 293–306. DOI: 10.1080/00221686.2012.654671.

Hsu, H.C., Chen, Y.Y., Chen, Y.R., and Li, M.S. (2022). “Experimental Study of Forces Influencing Vertical Breakwater under Extreme Waves”. In: *Water* 14, p. 657. DOI: 10.3390/w14040657.

Hughes, S.J. (1993). “Physical Models and Laboratory Techniques in Coastal Engineering. Advanced series on ocean engineering”. In: *Advanced series on ocean engineering*.

Jacobsen, N., Van Gent, M., Capel, A., and Borsboom, M. (2018). “Numerical prediction of wave loads on crest walls on top of rubble mound structures”. In: *Coastal Engineering* 142, pp. 110–124. DOI: 10.1016/j.coastaleng.2018.10.004.

Jacobsen, N., Van Gent, M., and Wolters, G (2015). “Numerical analysis of the interaction of irregular waves with two dimensional permeable coastal structures”. In: *Coastal Engineering* 102, pp. 13–29. DOI: 10.1016/j.coastaleng.2015.05.004.

Jacobsen, N.G., Fuhrman, D.R., and Fredsoe, J. (2012). “A Wave Generation Toolbox for the Open-Source CFD Library: OpenFoam®”. In: *International Journal for Numerical Methods in Fluids* 70.9, pp. 1073–1088. DOI: 10.1002/fld.2726.

Jelinek, R. and Krausmann, E. (2009). “Approaches to Tsunami Risk Assessment”. In: *OPOCE*.

Jensen, B., Jacobsen, N.G., and Christensen, E.D. (2014). “Investigations on the porous media equations and resistance coefficients for coastal structures”. In: *Coastal Engineering* 84, 56–72.

Kato, F., Inagaki, S., and Fukuhama, M. (2007). “Wave Force on Coastal Dike due to Tsunami”. In: *Coastal Engineering 2006*, pp. 5150–5161. DOI: 10.1142/9789812709554_0431.

Krautwald, C., Häfen, H. von, Niebuhr, P-, Vögele, K., Stolle, J., Schimmels, S., Schürenkamp, D., Sieder, M., and Goseberg, N. (2022). “Collapse processes and associated loading of square light-frame timber structures due to bore-type waves”. In: *Coastal Engineering* 177. DOI: 10.1016/j.coastaleng.2022.104178.

Lampela, K. (2020). “Breaking of the tsunami waves before shoreline on the shallow water”. In: *The 17th World Conference on Earthquake Engineering*.

Larsen, B.E. and Fuhrman, D. R. (2018). “On the over-production of turbulence beneath surface waves in Reynolds-averaged Navier–Stokes models”. In: *Journal of Fluid Mechanics* 853, pp. 419–460. DOI: 10.1017/jfm.2018.577.

Larsen, B.E. and Fuhrman, D.R. (2019). “Full-scale CFD simulation of tsunamis. Part 1: Model validation and run-up”. In: *Coastal Engineering Journal* 151, pp. 22–41.

Larsen, B.E., Fuhrman, D.R., and Johan, R. (2019b). “Performance of interFoam on the simulation of progressive waves”. In: *Coastal Engineering Journal* 61, pp. 380–400.

Losada, J.I., Lara, J.L., Raul, G., and Gonzalez-Ondina, Jose M. (2008). “Numerical analysis of wave overtopping of rubble mound breakwaters”. In: *Coastal Engineering* 55.1, pp. 47–62. ISSN: 0378-3839. DOI: 10.1016/j.coastaleng.2007.06.003. URL: https://www.sciencedirect.com/science/article/pii/S0378383907000713.

Madsen, P., Fuhrman, D., and Schäffer, H. (2008). “On the solitary wave paradigm for tsunamis”. In: *Journal of Geophysical Research* 113. DOI: 10.1029/2008JC004932.

Mata, M. I. (2021). “Numerical estimation of wave loads on crest walls on top of rubble mound breakwaters using OpenFOAM”. MA thesis. Delft University of Technology.

Mata, M.I. and Van Gent, M. (2023). “Numerical modelling of wave overtopping discharges at rubble mound breakwaters using OpenFOAM®”. In: *Coastal Engineering* 181. ISSN: 0378-3839. DOI: 10.1016/j.coastaleng.2022.104274.

Mcgovern, D, Todd, D., Rossetto, T., Whitehouse, R.J.S., Monaghan, J., and Gomes, E. (2019). “Experimental observations of tsunami induced scour at onshore structures”. In: *Coastal Engineering* 152, p. 103505. DOI: 10.1016/j.coastaleng.2019.103505.

Mcgovern, D., Allsop, W., Rossetto, T., and Chandler, I. (2023). “Large-scale experiments on tsunami inundation and overtopping forces at vertical sea walls”. In: *Coastal Engineering* 179, p. 104222. DOI: 10.1016/j.coastaleng.2022.104222.

McGovern, D., Robinson, T., Chandler, I., Allsop, W., and Rossetto, T. (2018). “Pneumatic long-wave generation of tsunami-length waveforms and their runup”. In: *Coastal Engineering* 138. DOI: 10.1016/j.coastaleng.2018.04.006.

Mizutani, S. Imamura F. (2015). “Dynamic wave force of tsunami acting on a structure”. In: *ITS 2001 Proceedings, Session 7, Number 7-28*.

Moretto, M. (2020). “An efficient numerical approach to model wave overtopping of rubble mound breakwaters”. MA thesis. Delft University of Technology.

Neumann, B., Vafeidis, A., Zimmermann, J., and Nicholls, R. (2015). “Future Coastal Population Growth and Exposure to Sea-Level Rise and Coastal Flooding - A Global Assessment”. In: *PLoS ONE* 10. DOI: 10.1371/journal.pone.0118571.

NILIM (2013). *A draught manual for developing earthquake-tsunami disaster scenarios including damage to public works, Japan (in Japanese)*.

Oda, K., Hayakawa, T., and Naoi, S. (2005). “A new approach to the mitigation effects of break waters against Tsunami in Ports and Harbors (in Japanese)”. In: *Annual Journal of Coastal Engineering* JSCE 52, pp. 291–295.

Oetjen, J., Vallam, S., Sriram, V., Reicherter, K., Engel, M., Schüttrumpf, H., and Sannasiraj, S.A. (2022). “A comprehensive review on structural tsunami countermeasures”. In: *Natural Hazards Review* 113. DOI: 10.1007/s11069-022-05367-y.

PARI (2011). *Verification of the tsunami damage process at Kamaishi Port*. URL: https://www.pari.go.jp/info/tohoku-eq/20110401.html.

Patil, A. (2019). “Numerical investigation of nearshore wave transformation and surf zone hydrodynamics”. MA thesis. Delft University of Technolgy.

Patil, A., M., Disanayaka, Bricker, J., Uijttewaal, W., and Keetels, G. (2018). “Effect of the overflow nappe non-aeration on tsunami breakwater failure”. In: *Coastal Engineering Proceedings* 1, p. 18. DOI: 10.9753/icce.v36.papers.18.

Paulsen, B.T. (2013). “Efficient computations of wave loads on offshore structures”. PhD thesis. Technical University of Denmark.

Rossetto, T., Allsop, W., Charvet, I., and Robinson, D. (June 2011). “Physical modelling of tsunami using a new pneumatic wave generator”. In: *Coastal Engineering* 58, pp. 517–527. DOI: 10.1016/j.coastaleng.2011.01.012.

Schiereck, G. and Verhagen, H.J. (2012). *Introduction to bed bank and shore protection*.

Shibayama, T., Esteban, M., Nistor, I., Takagi, H., Thao, N., Matsumaru, R., Mikami, T., Aranguiz, R., Jayaratne, R., and Ohira, K. (2013). “Classification of Tsunami and Evacuation Areas”. In: *Natural Hazards* 67. DOI: 10.1007/s11069-013-0567-4.

Takagi, H. and Bricker, J. (2015). “Breakwater damage and the effect of breakwaters on mitigation of inundation extent during tsunamis: Case study of the 2011 great east Japan earthquake and tsunami”. In: *Handbook of Coastal Disaster Mitigation for Engineers and Planners*, pp. 363–383. DOI: 10.1016/B978-0-12-801060-0.00018-6.

Takahashi, S (1996). *Design of vertical Breakwaters*. Port and airport research institute, Japan.

Tanimoto, K., Takayama, T., Murakami, K., Murata, S., Tsuruya, H., Takahashi, S., Morikawa, M., Yoshimoto, Y., and Nakano S. Hiraishi, T (1983). “Field laboratory investigations of the Tsunami caused by 1983 Nihonkai Chubu earthquake. (in Japanese)”. In: *Technical Note of the Port and Harbour Research Institute* 470.

Telford, J., Cosgrave, J., and Houghton, R. (2006). *Joint Evaluation of the international response to the Indian Ocean tsunami: Synthesis Report*.

“The makewaves tsunami collaboration” (2024). English. In: *Coasts, Marine Structures and Breakwaters 2023*. United Kingdom: Emerald Publishing, pp. 823–828. ISBN: 9780727767042. DOI: 10.1680/cmsb.67042.0823.

Tucker, J. (2013). “The Failure of the Kamaishi Tsunami Protection Breakwater”. In: *Coastal and Ocean Engineering ENGI.8751 Undergraduate Student Forum* PT13.

Van Balen, I. (2023). “The Efficacy Of Nature-Based versus Man-Made Tsunami Wave Run-Up Mitigation Strategies”. MA thesis. Delft University of Technology.

Van Gent, M. (1995). “Porous Flow through Rubble-Mound Material”. In: *Journal of Waterway Port Coastal and Ocean Engineering-asce - J WATERW PORT COAST OC-ASCE* 121. DOI: 10.1061/(ASCE)0733-950X(1995)121:3(176).

Veraghen, H.J. and Van Den Bos, J.P. (2017). *Breakwater design*. TU Delft, Department Hydraulic Engineering.

Wüthrich, D., Pfister, M., Nistor, I., and Schleiss, A. (2018). “Experimental study on the hydrodynamic impact of tsunami-like waves against impervious free-standing buildings”. In: *Coastal Engineering Journal* 56, pp. 1–20. DOI: 10.1080/21664250.2018.1466676.

# A

# Experimental elevation and pressure time series

This appendix shows the time series of the experimental elevation and pressure records obtained by the analysis of data collected by Van Balen (2023).

## A.1. Experimental elevation time series

Figures A.1 and A.2 show the original elevation time series obtained at LWG2,LWG3,LWG4,LWG5,LWG6 and SWG4 and SWG6, in the time frame of the passage of the E20 wave.

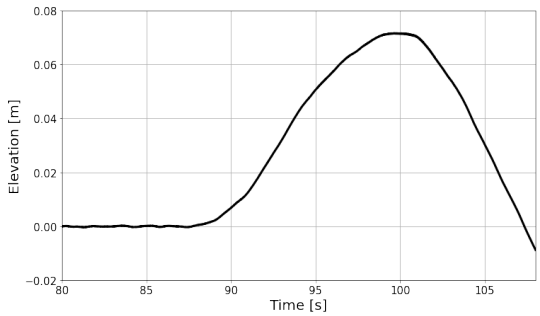


**(a)** Elevation at LWG2

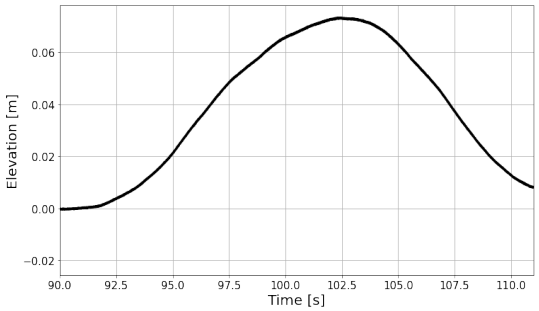


**(b)** Elevation at LWG3

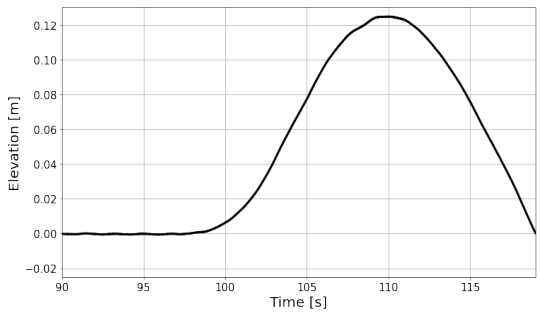


**(c)** Elevation at LWG4

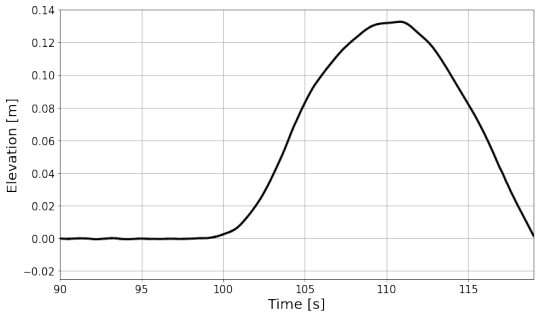


**(d)** Elevation at LWG5

**Figure A.1:** Elevation signals in the experiment offshore of the caisson

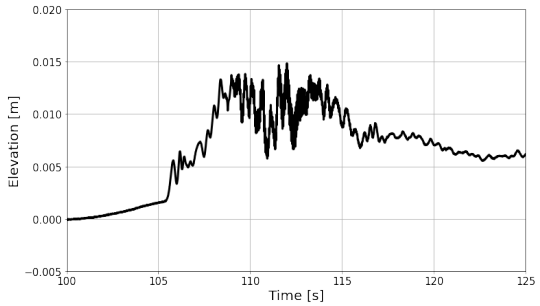


**(a)** Elevation at LWG6

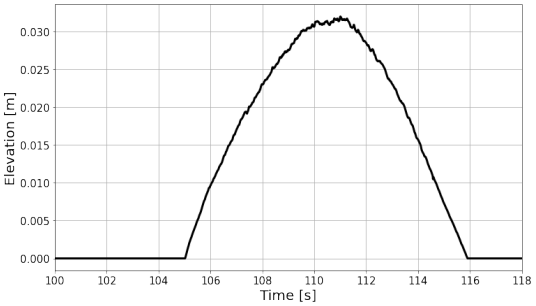


**(b)** Elevation at SWG4

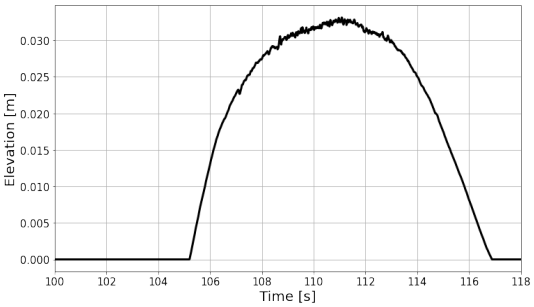


**(c)** Elevation at SWG6

**Figure A.2:** Elevation signals in the experiment on top and onshore of the caisson

## A.2. Experimental pressure time series

Figure A.4 displays the pressure records from the experimental pressure time series on the front face of the caisson. Figure A.5 presents the pressure records for sensors on the top and bottom faces. For the pressure sensors located on the front and top, and bottom of the caisson, the total, hydrostatic, and hydrodynamic pressures were derived from the filtered pressure records as explained in Section 4.1.2. Figure A.6 shows the total pressure for the sensors on the lee side of the caisson, filtered according to Section 3.1.5.

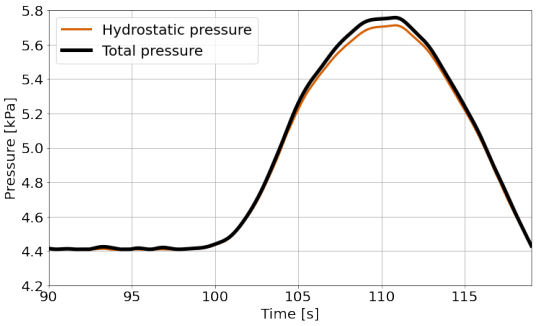


**(a)** Pressure at PT3

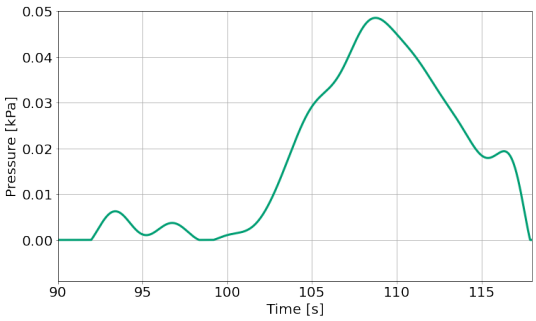


**(b)** Hydrodynamic pressure at PT3

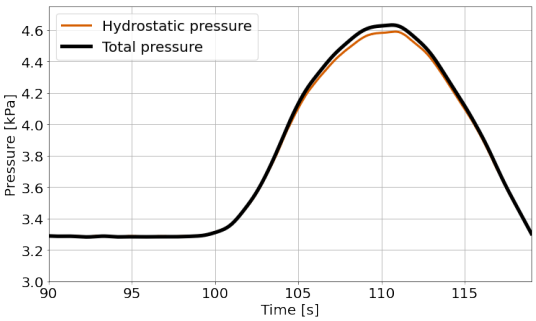


**(c)** Pressure at PT01

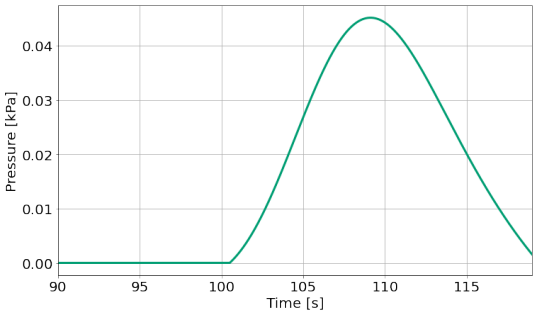


**(d)** Hydrodynamic pressure at PT01

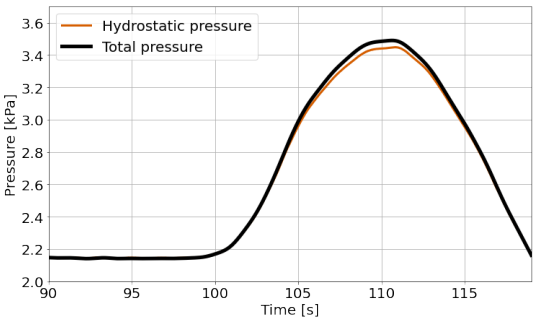


**(e)** Pressure at PT02

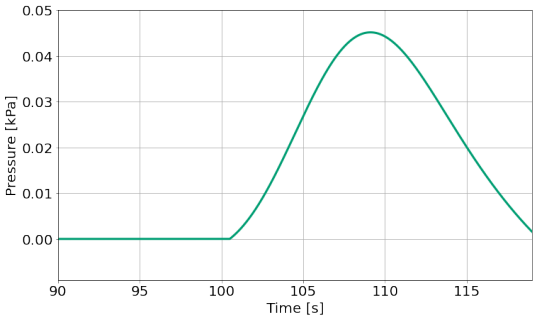


**(f)** Hydrodynamic pressure at PT02

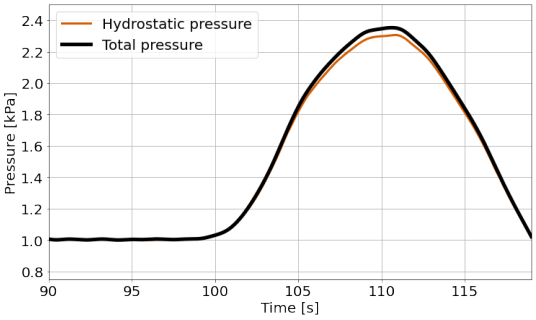


**(g)** Pressure at PT03

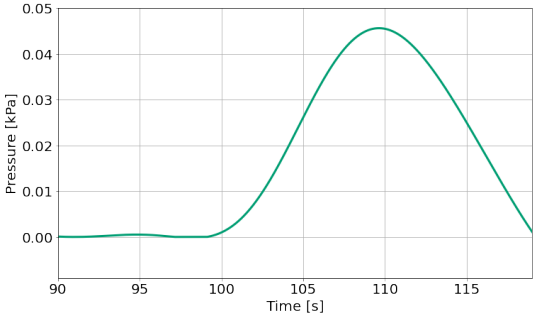


**(h)** Hydrodynamic pressure at PT03

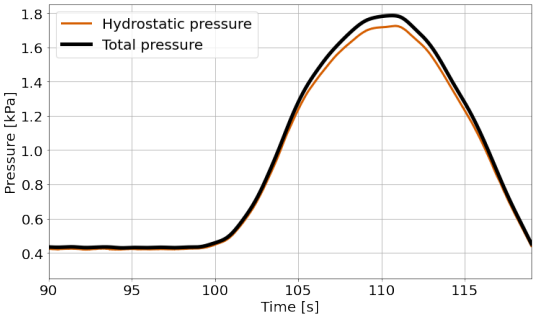


**(i)** Pressure at PT04

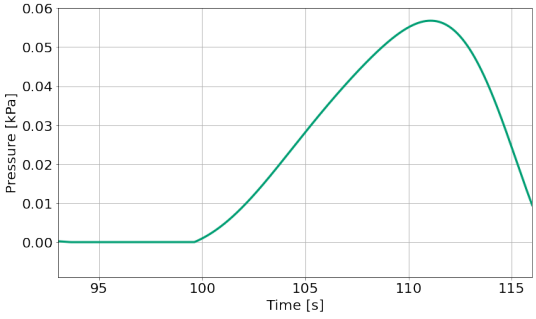


**(j)** Hydrodynamic pressure at PT04

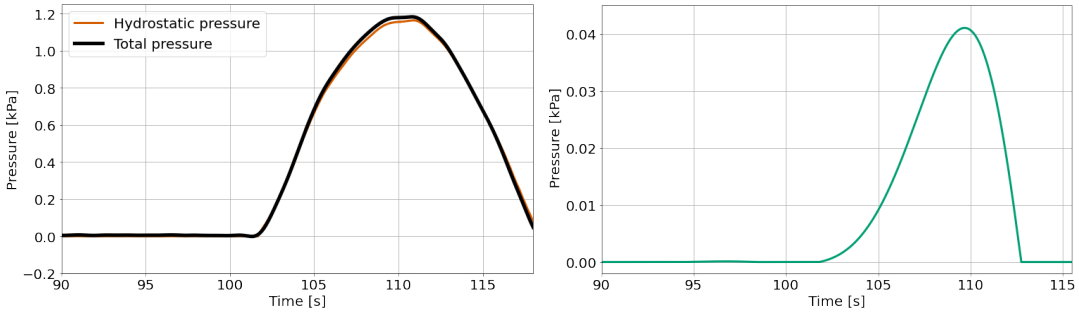


**(a)** Pressure at PT05 **(b)** Hydrodynamic pressure at PT05

**Figure A.4:** Total, hydrostatic and hydrodynamic pressures (front face)

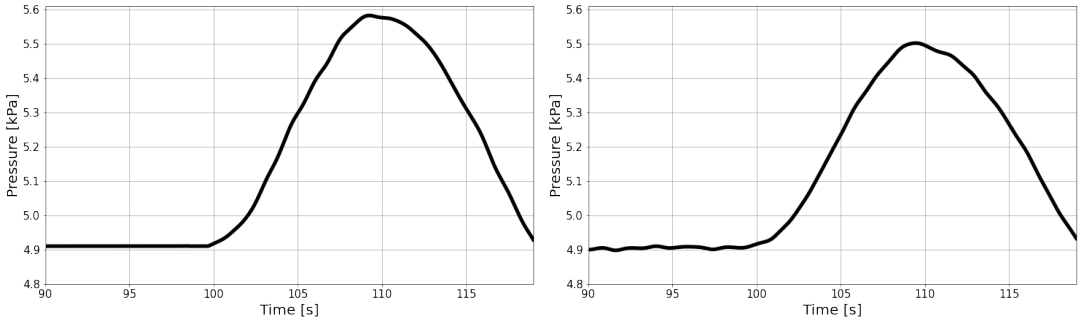


**(a)** Pressure at PT1 **(b)** Pressures at PT2

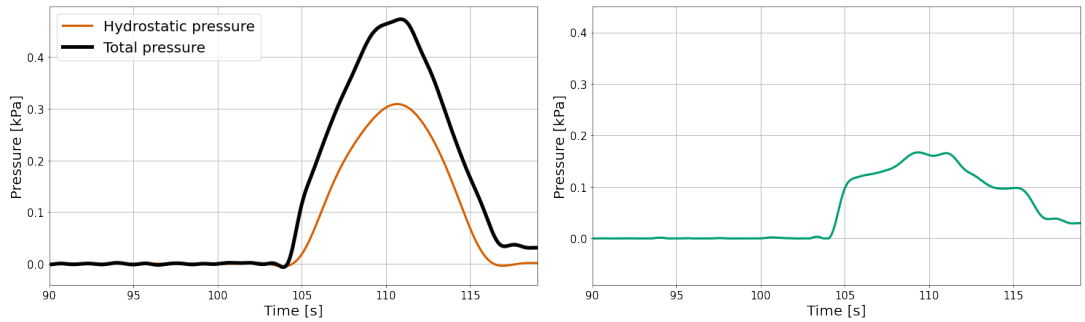


**(c)** Pressure at PT08 **(d)** Hydrodynamic pressure at PT08

**Figure A.5:** Total, hydrostatic and hydrodynamic pressures (bottom and top face)

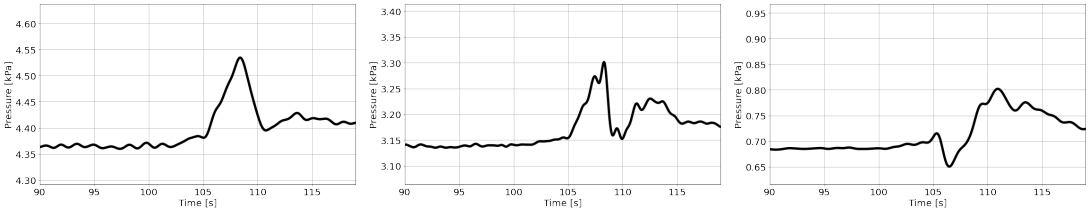


**(a)** Pressure at PT4 **(b)** Pressure at PT06 **(c)** Pressure at PT07

**Figure A.6:** Total, hydrostatic and hydrodynamic pressures (back face)

# B

# OceanWave3D Sensitivity analysis

In this appendix, the results of the grid and temporal sensitivity study conducted for the OceanWave3D domain are shown. The sensitivity analysis followed recommendations mentioned in Section 3.3.2 The final mesh and time step derived from this analysis were implemented in the model and are detailed in the Methodology.
The sensitivity analysis aimed at determining:

- The best resolution of the grid expressed in $\Delta x$ and number of layers in the vertical direction.
- The optimal time step $\Delta t$ impoosed in OCW3D.

## B.1. Spatial Resolution

The calibration of the OCW3D domain was conducted by comparing the elevation time series near the origin of the numerical domain to the elevation time series at LWG2 in the physical flume. This ensured an accurate representation of the elevation time signal imposed at the inlet of the domain, corresponding to the location of LWG2.

The spatial resolution was tested with a time step $\Delta t$ = 0.01 s to speed up the simulation time.
For the number of vertical layers, 12 layers were used as a starting value, as recommended by Jacobsen et al. (2018). Figure B.1 shows the results of the horizontal grid sensitivity analysis for three resolutions, $\Delta x$ = 0.23 m, $\Delta x$ = 0.12 m and $\Delta x$ = 0.06 m. To identify the best resolution in OCW3D, the Root Mean Square Error and Normalized Root Mean Square Error were used. Table B.1 shows the three horizontal resolutions tested in OCW3D and the values of the associated NRMSE.

**Table B.1:** Horizontal Sensitivity Analysis OCW3D

| **Test** | $\Delta x$ **[cm]** | **Nx** | **Ny** | $\Delta t$ [s] | **RMSE** | **NRMSE** |
|---|---|---|---|---|---|---|
| 1 | 23 m | 435 | 12 | 0.01 | 0.0061 | 0.085 |
| 2 | 12 | 833 | 12 | 0.01 | 0.0020 | 0.028 |
| 3 | 6 | 1667 | 12 | 0.01 | 0.0008 | 0.010 |

Since the initial guess of 12 vertical layers effectively represented the elevation signal, only a coarser resolution with 7 vertical layers was tested. The results of these tests are shown in Figure B.1, and the RMSE and NRMSE values are given in Table B.2.

The optimal spatial resolution for OCW3D, which produced the lowest RMSE when replicating the experimental elevation signal, was found to be $\Delta x = 12$ cm, with 12 layers in the vertical direction.

Albeit producing slightly higher RMSE, this resolution was computationally more convenient than the finest one and did not significantly affect accuracy in OpenFOAM.

**Table B.2:** Vertical sensitivity analysis

| **Test** | $\Delta x$ [cm] | **Nx** | **Ny** | $\Delta t$ [s] | **RMSE** | **NRMSE** |
|---|---|---|---|---|---|---|
| 1 | 6 | 1667 | 7 | 0.01 | 0.002 | 0.028 |
| 2 | 6 | 1667 | 12 | 0.01 | 0.001 | 0.011 |

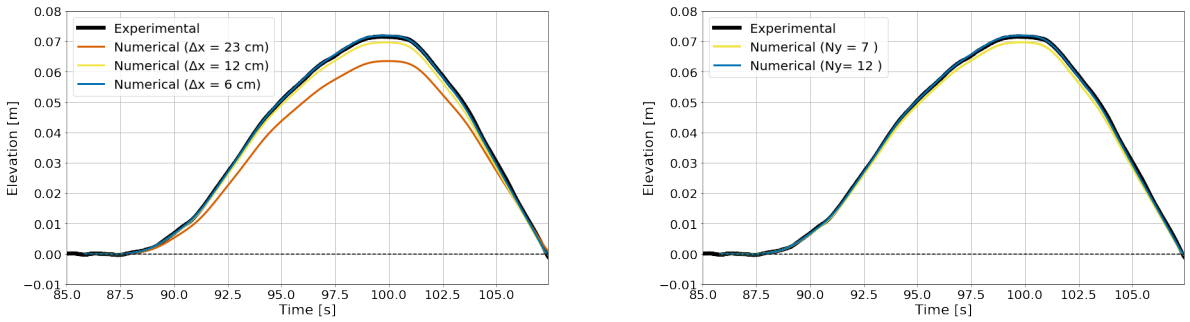


**Figure B.1:** Spatial sensitivity analysis in OceanWave3D

## B.2. Temporal Resolution

The initial time step of 0.01 s produced good elevation results with the spatial resolution indicated above and was therefore adopted as the temporal resolution in OceanWave3D. This value corresponds to both the timestep in the OceanWave3D simulation and the time interval for integrating the wave paddle signal. A further test with a finer timestep of 0.001 s was conducted. However, this resulted in increased computational time with only minor and negligible improvements in the representation of the elevation signal.

## B.3. Coupling with OpenFOAM

Prior to every simulation, a test was performed to verify that OceanWave3D and OpenFOAM were correctly coupled. The aim of the tests was to verify that the wave at the boundary between the OCW3D and OpenFOAM numerical domain was correctly transferred from the former to the latter.
The coupling was tested using a flat empty flume in OpenFoam, with no breakwater inserted so that the flow conditions could be identical in the OpenFoam and OceanWave3D domain.
To test the coupling, numerical wave gauges were placed at the same locations in both the OceanWave3D and the OpenFoam domain. It was ensured that the elevation time series at the wave gauges were identical in both OceanWave3D and OpenFOAM. This indicates that the two solvers are correctly coupled, and the wave does not become distorted when transferred to OpenFOAM.
Figure B.2 shows as an example the comparison between the elevation timeseries at the same location measured in OceanWave3D and OpenFOAM, as a result of the coupling test.

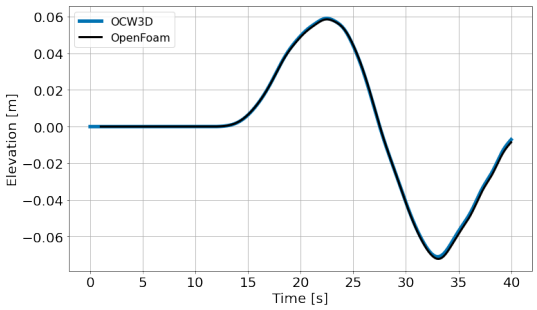


**Figure B.2:** Test on the coupling of OpenFOAM and OceanWave3D at $x$ = 34 m

# C

# OpenFoam sensitivity analysis

In this appendix, the results of the grid sensitivity analysis conducted for the OpenFOAM domain are shown. The sensitivity analysis followed recommendations mentioned in Section 3.3.2 The final mesh configuration implemented in the model is detailed in the Methodology.

## C.1. Spatial Resolution

The mesh resolution in OpenFoam was set as defined in Section 3.3.2, with a base coarser mesh and different refinement levels in the areas of interest. Firstly, a sensitivity analysis was conducted focusing on the elevation signals in front of the caisson and the pressure records on its front face. To do so, a refinement zone was defined along the SWL, 0.2 m above and below it for the whole domain length. Subsequently, the analysis shifted to the top of the caisson, where different resolutions were tested keeping the grid dimension in front of the caisson untouched. fter identifying the resolution on the top that effectively captured the overtopping, the sensitivity analysis progressed to the back of the caisson. Here, a further refinement zone was defined, according to Figure 3.5.

### C.1.1. Surface elevation sensitivity analysis

Figure C.1 show the results of the grid sensitivty analysis conducted on the elevation sensors LWG4, LWG5, LWG6, SWG4 and SWG6.

To determine the best resolution, RMSE between the experimental and the numerical values were calculated. Table C.1 presents the RMSE and NRMSE velues of the elevations time series offshore of the caisson, together with the difference of maximum elevation between the numerical result and the experimental one ($\Delta\eta = \eta_{max}(experimental) - \eta_{max}(numerical)$). This third indicator is particularly important because it relates to the maximum wave crest elevation. The force exerted by the wave peaks at the crest, making it crucial to obtain a precise estimate of this maximum elevation. Accurate measurement of the crest height is necessary to prevent the underestimation of forces.
The two finer resolutions showed better accordance with experimental data at LWG5, location closer to the breakwater. In particular, a mesh resolution of 0.75 cm result in very little NRMSE (below 0.1, indicating good representation of physical elevations) and also very small difference between experimental and numerical maximum elevation.
For the sensitivity analysis conducted at LWG6, only the RMSE and NRMSE have were calculated while no difference in elevation is shown, given the highly oscillatory signal of the surface elevation in that area.

**Table C.1:** Sensitivity analysis - elevations offshore of the breakwater

| **Resolution** | **LWG4** | | | **LWG5** | | |
|---|---|---|---|---|---|---|
| $\Delta x[cm]$ | RMSE | NRMSE | $\Delta\eta[\%]$ | RMSE | NRMSE | $\Delta\eta[\%]$ |
| 1.5 | 0.008 | 0.067 | 1.58 % | 0.011 | 0.080 | 5.97 % |
| 0.75 | 0.009 | 0.074 | -3.50 % | 0.010 | 0.077 | -0.97 % |
| 0.625 | 0.009 | 0.075 | -4.05 % | 0.010 | 0.077 | -1.07 % |

**Table C.2:** Sensitivity analysis - elevations on top and behind the breakwater

| **Resolution** | **SWG4** | | | **SWG6** | | | **LWG6** | |
|---|---|---|---|---|---|---|---|---|
| $\Delta x[cm]$ | RMSE | NRMSE | $\Delta\eta[\%]$ | RMSE | NRMSE | $\Delta\eta[\%]$ | RMSE | NRMSE |
| 0.75 | 0.0017 | 0.055 | 11.11 % | 0.0025 | 0.077 | -7.81 % | 0.004 | 0.28 |
| 0.375 | 0.0013 | 0.041 | -11.07 % | 0.0023 | 0.071 | -10.98 % | 0.0036 | 0.24 |
| 0.188 | 0.0024 | 0.076 | -11.27 % | 0.0023 | 0.069 | 11.58 % | 0.0061 | 0.43 |

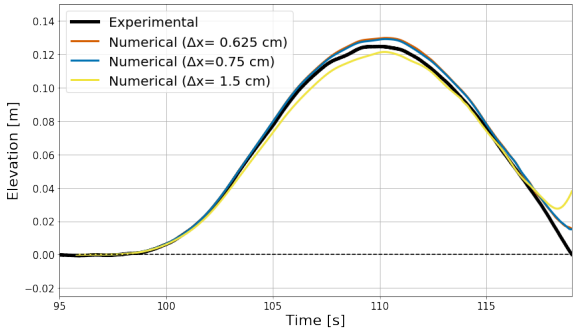


**(a)** Sensitivity Analysis - elevation at LWG4

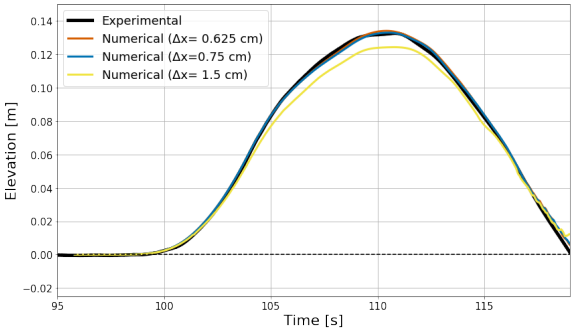


**(b)** Sensitivity Analysis - elevation at LWG5

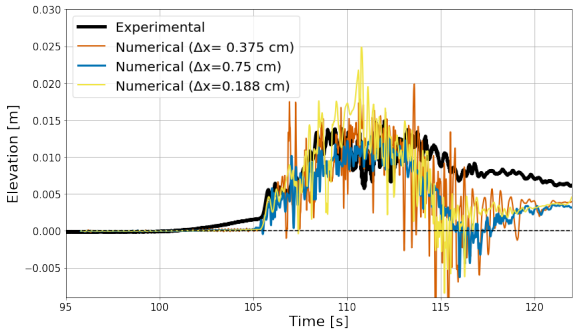


**(c)** Sensitivity Analysis - elevation at LWG6

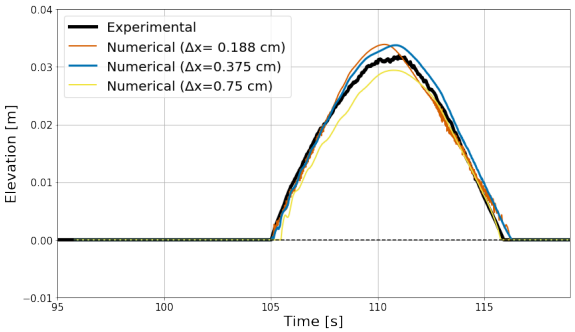


**(d)** Sensitivity Analysis - elevation at SWG4

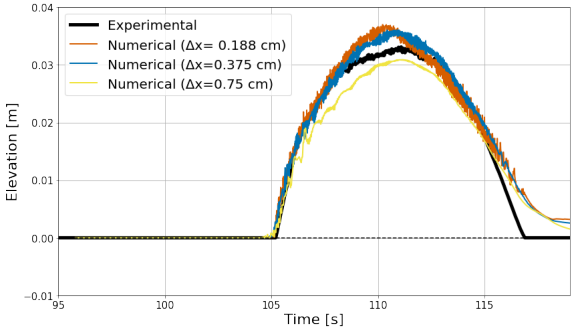


**(e)** Sensitivity Analysis - elevation at SWG6

**Figure C.1:** Sensitivity analysis - Elevations

## Pressure sensors sensitivity analysis

The grid sensitivity was then tested comparing the experimental pressure records to the numerical ones. Figure C.2 shows the results of the grid sensitivity analysis performed in the front face of the caisson for the pressure time series.

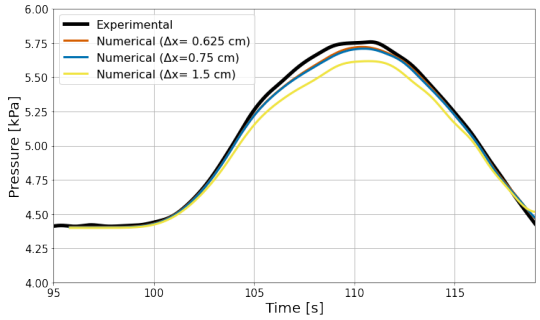


**(a)** Sensitivity Analysis - Pressure at PT3

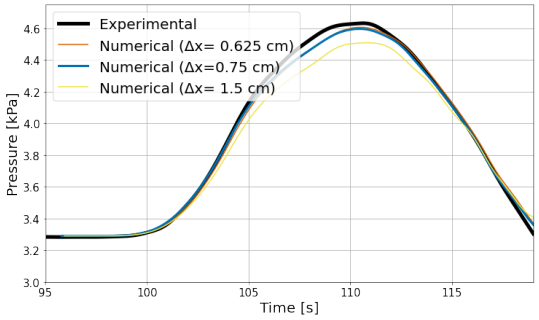


**(b)** Sensitivity Analysis - Pressure at PT01

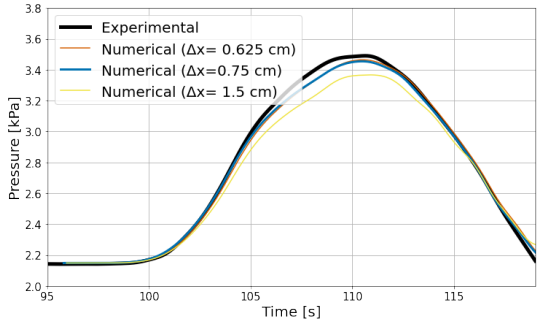


**(c)** Sensitivity Analysis - Pressure at PT02

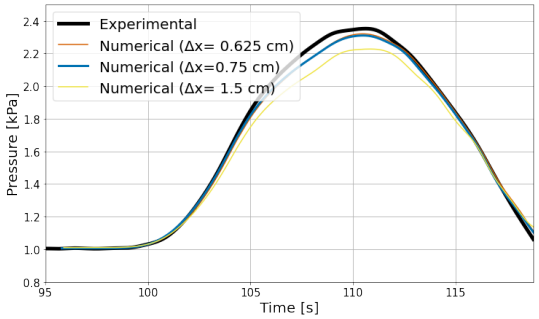


**(d)** Sensitivity Analysis - Pressure at PT03

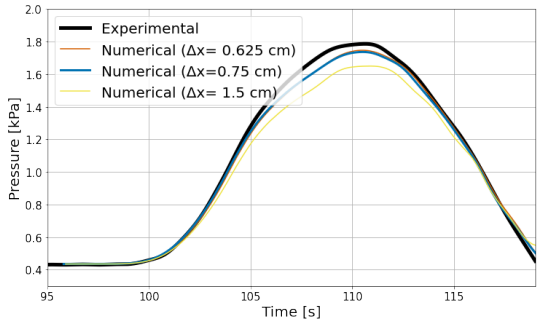


**(e)** Sensitivity Analysis - Pressure at PT04

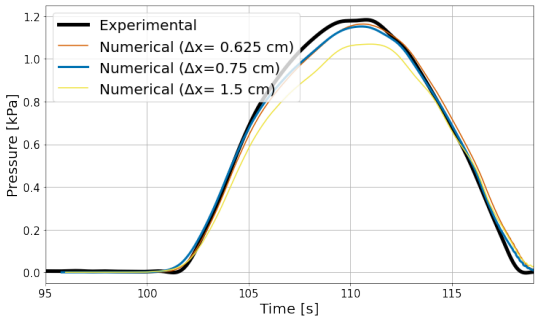


**(f)** Sensitivity Analysis - Pressure at PT05

**Figure C.2:** Sensitivity analysis - Pressures on the front face

When comparing experimental and numerical pressures, the difference between peak values ($\Delta p = p_{max}(experimental) - p_{max}(numerical)$) is an insightful indicator. This value is important because the forces acting on the caisson, and consequently its stability, are directly influenced by the pressure magnitudes.

Table C.3 summarizes the average RMSE, NRMSE and differences in maximum numerical and experimental pressure values on the front face of the caisson.

The resolutions of $\Delta x$ = 0.75 cm and $\Delta x$ = 0.625 cm both resulted in a good reproduction of the numerical pressure time series. Given the negligible differences, a resolution of $\Delta x$ = 0.75 cm was preferred in front of the caisson to save computational time.

**Table C.3:** Sensitivity analysis - pressures on the front face of the caisson

| **Resolution** | **Front face** | | |
|---|---|---|---|
| $\Delta x[cm]$ | RMSE | NRMSE | $\Delta p[\%]$ |
| 1.5 | 0.088 | 0.056 | -5.20 % |
| 0.75 | 0.039 | 0.0268 | -1.64 % |
| 0.625 | 0.036 | 0.0251 | -1.19 % |

In the region above and behind the caisson, lower elevation records require further levels of refinement. Therefore, further refinement zones have been employed on the region on top of the caisson and behind it, as shown in Figure 3.5.
First, a calibration procedure was performed on top of the breakwater. Following this, the resolution of the refinement zone on the back side of the caisson was tested.
When testing resolutions in the top and back region of the caisson, a resolution of $\Delta x$ = 0.75 cm was maintained around SWL in front of the breakwater, as derived from the sensitivity analysis performed in that area. Figure C.3 shows the results of the grid sensitivity analysis on top of the caisson. Table C.4 shows the RMSE, NRMSE as well as peak pressure differences for the top and back face of the caisson. From the table it can be concluded that applying a further level of refinement, with a resolution of $\Delta x$ = 0.375 cm on the top, corresponding to 9 cells per maximum elevation, produces the lowest RMSE and lowest overestimation of the pressures on top. Maintaining this resolution on top of the caisson, different levels of refinement were tested in the zone behind it. Grid size of $\Delta x$ = 0.75 cm, $\Delta x$ = 0.375 cm, and $\Delta x$ = 0.188 cm, corresponding to 2, 4, and 7 cells per maximum surface elevation on the lee side, respectively. The results of the pressure sensitivity analysis in the back face of the caisson for the pressure sensors is shown in Figure C.4 Given the highly oscillatory behaviour of the pressure records in this area due to the biphasic nature of the fluid, the numerical pressure sensors were filtered with the same filter employed for the experimental pressure sensors, for ease of interpretation. The filtered numerical signals are shown in the right plots in the Figure.

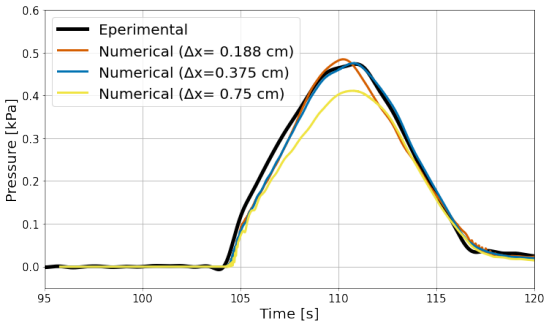


**(a)** Sensitivity Analysis - Pressure at PT08

**Figure C.3:** Sensitivity analysis - Pressures on the top face

**Table C.4:** Sensitivity analysis - pressures on the top and back face of the caisson

| **Resolution** | **Top face** | | | **Back face** | |
|---|---|---|---|---|---|
| $\Delta x[cm]$ | RMSE | NRMSE | $\Delta p[\%]$ | RMSE | NRMSE |
| 0.75 | 0.038 | 0.079 | -13.3 % | 0.056 | 0.350 |
| 0.375 | 0.015 | 0.032 | 0.46 % | 0.060 | 0.380 |
| 0188 | 0.019 | 0.040 | 2.34 % | 0.063 | 0.401 |

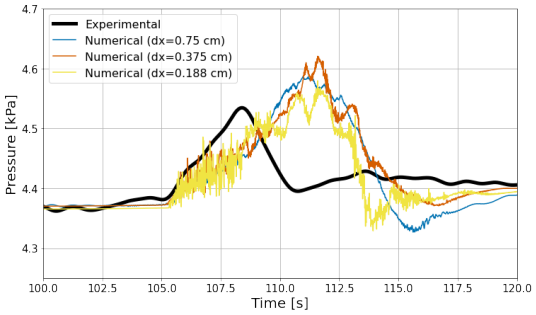


**(a)** Sensitivity Analysis - Pressure at PT4

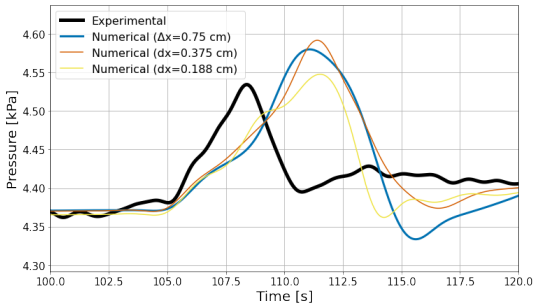


**(b)** Sensitivity Analysis - Filtered Pressure at PT4

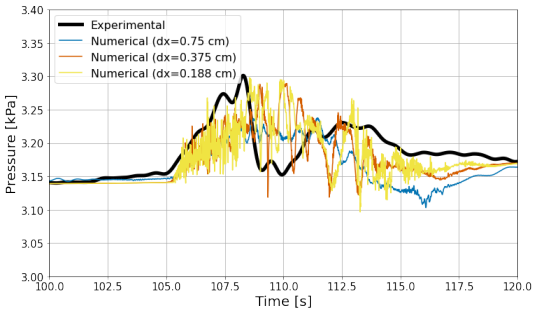


**(c)** Sensitivity Analysis - Pressure at PT06

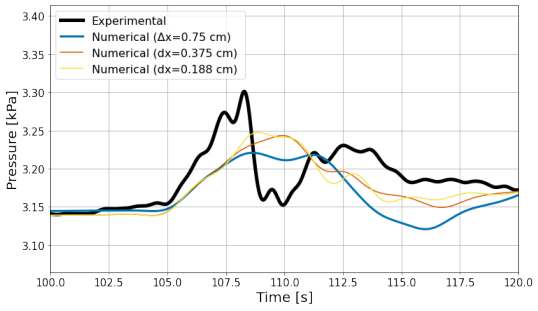


**(d)** Sensitivity Analysis - Filtered Pressure at PT06

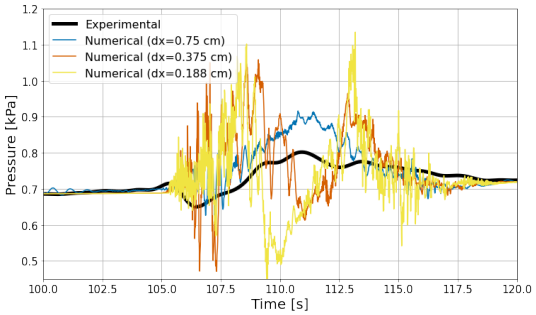


**(e)** Sensitivity Analysis - Pressure at PT07

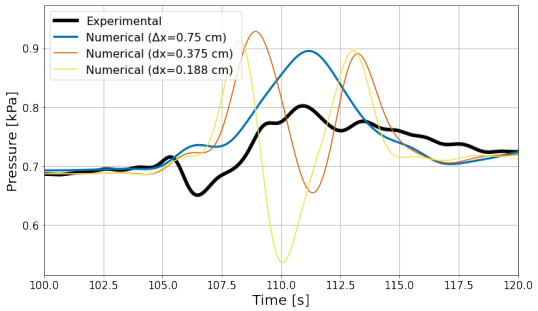


**(f)** Sensitivity Analysis - Filtered Pressure at PT07

**Figure C.4:** Sensitivity analysis - Pressures on the back face

## C.1.2. Porous layers sensitivity analysis

In the porous layer zone, a resolution of $\Delta x = \Delta y$ = 1.5 cm was used, corresponding to 2 levels of refinement from the base mesh dimension 6 x 6 cm. Additional levels of refinement proved to not produce more accurate results but only increased the computational time. Three different resistance parameters were tested for the porous layers, as detailed in Section 3.2.7. Figure C.5 details the different pressure records at PT1 and PT2 in the bottom face of the caisson with the three different resistance parameters. In Table C.5, the average values of RMSE, NRMSE and pressure over-underestimation are shown for the three configurations of porosity parameters that were tested.

**Table C.5:** Sensitivity analysis - pressures on the bottom face of the caisson

| **Test** | **Coefficients** | **Bottom face** | | |
|---|---|---|---|---|
| | | RMSE | NRMSE | $\Delta p[\%]$ |
| Jensen | $\alpha = 500, \beta = 2$ | 0.12 | 0.19 | 3% |
| van Gent | $\alpha = 1000, \beta = 1.1$ | 0.13 | 0.20 | 4% |
| Losada | $\alpha = 200, \beta = 0.8$ | 0.12 | 0.18 | 3% |

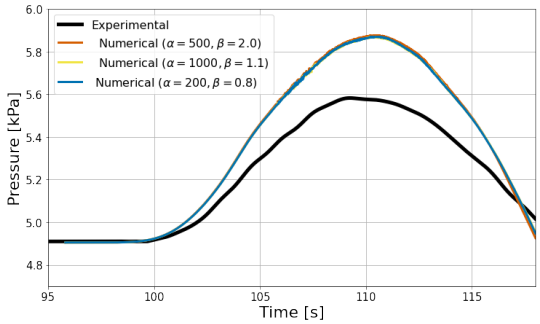


**(a)** Sensitivity Analysis - Pressure at PT1

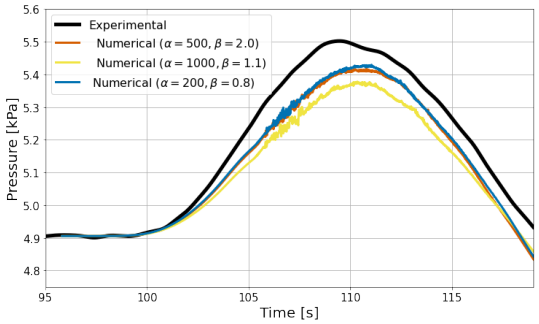


**(b)** Sensitivity Analysis - Pressure at PT2

**Figure C.5:** Sensitivity analysis - Pressures on the bottom face

The table show that the resistance coefficients suggested by Losada et al. (2008) produce the lowest over-underestimation of pressures at PT1 and PT2.

## C.2. Temporal Resolution

In OpenFoam, no temporal sensitivity analysis was performed since the timestep is not a fixed value but adapts to the constraint of maximum Courant number, imposed to 0.05 as detailed in Section 3.3.3.